

# 広島大学学位請求論文

A Family of Multiproperty Coordination Polymers  
[Mn<sup>II</sup>(LH)(H<sub>2</sub>O)][Cr<sup>III</sup>(CN)<sub>6</sub>]·H<sub>2</sub>O, L = *R*-pn, *rac*-pn or en

多様な物性を示す配位重合体

[Mn<sup>II</sup>(LH)(H<sub>2</sub>O)][Cr<sup>III</sup>(CN)<sub>6</sub>]·H<sub>2</sub>O, L = *R*-pn, *rac*-pn or en

2008 年

広島大学大学院理学研究科

化学専攻

吉田 祐輔

# 目次

## 1. 主論文

A Family of Multiproperty Coordination Polymers

$[\text{Mn}^{\text{II}}(\text{LH})(\text{H}_2\text{O})][\text{Cr}^{\text{III}}(\text{CN})_6]\cdot\text{H}_2\text{O}$ , L = *R*-pn, *rac*-pn or en

多様な物性を示す配位重合体

$[\text{Mn}^{\text{II}}(\text{LH})(\text{H}_2\text{O})][\text{Cr}^{\text{III}}(\text{CN})_6]\cdot\text{H}_2\text{O}$ , L = *R*-pn, *rac*-pn or en

吉田 祐輔

## 2. 公表論文

(1) Reversible Single-Crystal-to-Amorphous Phase Transition upon Dehydration-Rehydration and Associated Magnetism in  $[\text{Mn}^{\text{II}}(\text{enH})(\text{H}_2\text{O})][\text{Cr}^{\text{III}}(\text{CN})_6]\cdot\text{H}_2\text{O}$ .

Yoshida, Y; Inoue, K; Kurmoo, M.

*Chem. Lett.* **2008**, 37, 504

(2) Crystal Structures and magnetic Properties of  $[\text{Mn}^{\text{II}}(\text{rac-pnH})(\text{H}_2\text{O})\text{Cr}^{\text{III}}(\text{CN})_6]\cdot\text{H}_2\text{O}$  and its Dehydrated Form.

Yoshida, Y; Inoue, K; Kurmoo, M.

*Chem. Lett. Accepted.*

## 3. 参考論文

(1) Three-Dimensional Chiral Molecule-Based Ferrimagnet with Triple-Helical-Strand Structure

Imai, H.; Inoue, K.; Kikuchi, K.; Yoshida, Y.; Ito, M.; Sunahara, T.; Onaka, S.

*Angew. Chem. Int. Ed.* **2004**, 43, 5618-5621

(2) Magnetic resonance in a [ $\{\text{Cr}(\text{CN})_6\}\{\text{Mn}(\text{S-pnH}-(\text{H}_2\text{O}))\} \cdot \text{H}_2\text{O}$ ] single-crystal molecular ferrimagnet

Blokhin, I. V.; Markosyan, A. S.; Morgunov, R. B.; Inoue, K.; Tanimoto, Y.; Yoshida, Y.

*Physics of the Solid State*. **2005**, *47*, 2106-2113.

(3) Synthesis, Structure and Magnetic Properties of Chiral Molecule-Based Magnets

Kishine, J.; Inoue, K.; Yoshida, Y.

*Prog. Theor. Phys. Suppl.* **2005**, 82-95.

(4) Chiral Magnetic Ordering and Commensurate-to-incommensurate Transition in  $\text{CuB}_2\text{O}_4$

Kousaka, Y.; Yano, S.; Kishine, J.; Yoshida, Y.; Inoue, K.; Akimitsu, J.

*J. Magn. Magn. Mater.* **2007**, *310*, 463-464.

(5) Structural and Magnetic Investigations for the Doping Effect of Nonmagnetic Impurity on the Spin-Peierls-like Transition in a Quasi-One-Dimensional Magnet: 1-(4'-Nitrobenzyl)pyridinium Bis(maleonitriledithiolato)nickelate.

Ren, X. M.; Akutagawa, T.; Noro, S.; Nishihara, S.; Nakamura, T.; Yoshida, Y.; Inoue, K.

*J. Phys. Chem. B* **2006**, *110*(15), 7671-7677.

# 主論文

A Family of Multiproperty Coordination Polymers  
 $[\text{Mn}^{\text{II}}(\text{LH})(\text{H}_2\text{O})][\text{Cr}^{\text{III}}(\text{CN})_6]\cdot\text{H}_2\text{O}$ , L = *R*-pn, *rac*-pn or en

Yusuke Yoshida

Doctor of Philosophy

Department of Chemistry  
Hiroshima University

2008

# Contents

## A Family of Multiproperty Coordination Polymers [Mn<sup>II</sup>(LH)(H<sub>2</sub>O)][Cr<sup>III</sup>(CN)<sub>6</sub>]·H<sub>2</sub>O, L = *R*-pn, *rac*-pn or en

### Summary

<b>Chapter I</b>	1
<b>Introduction</b>	2
<b>Chapter II</b>	6
<b>Experimental Section</b>	7
II-1.    Synthesis of K <sub>3</sub> [Cr(CN) <sub>6</sub> ]	7
II-2.1.  Synthesis of <i>R</i> -pn·2HCl	8
II-2.2.  Synthesis of <i>S</i> -pn·2HCl	9
II-2.3.  Synthesis of <i>rac</i> -pn·2HCl	10
II-2.4.  Synthesis of en·2HCl	11
II-3.1.  Synthesis of [Mn( <i>R</i> -pnH)(H <sub>2</sub> O)][Cr(CN) <sub>6</sub> ]·H <sub>2</sub> O ( <b>RGN-LTP</b> )	11
II-3.2.  Synthesis of [Mn( <i>S</i> -pnH)(H <sub>2</sub> O)][Cr(CN) <sub>6</sub> ]·H <sub>2</sub> O ( <b>SGN-LTP</b> )	12
II-3.3.  Synthesis of [Mn( <i>rac</i> -pnH)(H <sub>2</sub> O)][Cr(CN) <sub>6</sub> ]·H <sub>2</sub> O ( <b>racGN</b> )	12
II-3.4.  Synthesis of [Mn(enH)(H <sub>2</sub> O)][Cr(CN) <sub>6</sub> ]·H <sub>2</sub> O ( <b>enGN</b> )	13
II-4.    Elemental analyses	14
II-5.    Infrared spectroscopy	14
II-6.    Polarimetry	14
II-7.    UV-Vis spectroscopy	15
II-8.    Magnetic measurements	15
II-9.    Thermogravimetric and differential thermal analyses	18
II-10.   Differential scanning calorimetry	18
II-11.   Powder X-ray diffraction	18
II-12.   Single crystal X-ray diffraction	19
<b>Chapter III</b>	21
<b>[Mn(<i>R</i>-pnH)(H<sub>2</sub>O)][Cr(CN)<sub>6</sub>]·H<sub>2</sub>O: A Chiral Soft Ferrimagnet Displaying Two Reversible Single Crystal-to-Single Crystal Transformations, proton transfer and Increment of Curie Temperature</b>	
III-1.    Abstract	22
III-2.    Introduction	23
III-3.    Results and discussion	24
III-3.1.  Synthesis	24

III-3.2.	Thermogravimetric and differential thermal analyses	25
III-3.3.	Differential scanning calorimetry	26
III-3.4.	Crystal structures	27
III-3.4.1.	Structures of virgin <b>RG</b> N-LTP (1), relaxed <b>RG</b> N-LTP (6), relaxed <b>RG</b> N-LTP (10), and rehydrated <b>RG</b> N-HP (14) at 298 K	34
III-3.4.2.	Structures of <b>RG</b> N-HTP at 330 K (3), <b>RG</b> N-HTP at 298 K (4), and quenched <b>RG</b> N-HTP at 200 K (8)	35
III-3.4.3.	Structures of <b>RG</b> N-DP (12) at 298 K	36
III-3.5.	Powder X-ray diffraction	38
III-3.6.	Mechanism for structural transformation and dehydration	40
III-3.7.	Infrared spectroscopy	43
III-3.8.	UV-Vis spectroscopy	46
III-3.9.	Magnetic properties	47
III-3.10.	Ac-susceptibilities	50
III-3.11.	Hysteresis loops	52
III-3.12.	Isothermal magnetization on single crystals	55
III-3.13.	Magnetic structures	57
III-3.14.	Conformation of structural phase transition and dehydration for <i>S</i> -isomer [Mn( <i>S</i> -pnH)(H <sub>2</sub> O)][Cr(CN) <sub>6</sub> ]·H <sub>2</sub> O	58
III-4.	Conclusion	61

## Chapter IV 63

### [Mn(*rac*-pnH)(H<sub>2</sub>O)][Cr(CN)<sub>6</sub>]·H<sub>2</sub>O: Reversible Dehydration-Rehydration Induces Increment-Decrement of Dimensionality, Curie Temperature and Magnetic Hardness

IV-1.	Abstract	64
IV-2.	Introduction	64
IV-3.	Results and discussion	65
IV-3.1.	Crystal structures	65
IV-3.1.1.	Crystal structure of virgin <i>rac</i> GN	72
IV-3.1.2.	Crystal structure of <i>rac</i> GN-DP	74
IV-3.2.	Thermogravimetric analyses	75
IV-3.3.	Differential scanning calorimetry	76
IV-3.4.	Powder X-ray diffraction	77
IV-3.5.	Infrared spectroscopy	79
IV-3.6.	Magnetic properties	81
IV-4.	Conclusion	86

## Chapter V 87

### [Mn(enH)(H<sub>2</sub>O)][Cr(CN)<sub>6</sub>]·H<sub>2</sub>O : Reversibility of Single Crystal-to-Amorphous Dehydrated Phase and Associated Increment-Decrement of Curie Temperature and Magnetic Hardness

V-1.	Abstract	88
V-2.	Introduction	88
V-3.	Results and discussion	90
V-3.1.	Crystal structures	90
V-3.1.1.	Crystal structure for enGN and its rehydrated form	93

V-3.1.2.	Crystal structure for dehydrated structure of <b>enGN-DP</b>	95
V-3.2.	Thermogravimetric analyses	96
V-3.3.	Powder X-ray diffraction	97
V-3.4.	Infrared spectroscopy	98
V-3.5	Magnetic properties	100
V-4.	Conclusion	104

## **Chapter VI**

<b>Concluding Remarks</b>	106
---------------------------	-----

<b>References</b>	109
-------------------	-----

## **APPENDIX**

**Syntheses, Structures and Magnetic Properties of One-Dimensional Chains of  
Transition Metals with O-P-O Bridges**  
Full paper submitted to Dalton Transactions

## **Acknowledgement**



## Summary

This thesis describes the syntheses, structures and physical properties (thermal, optical and magnetic) of hetero-bimetallic mixed-valence coordination polymers belonging to the family of Prussian blue cyanide compounds.  $[\text{Mn}^{\text{II}}(R\text{-pnH})(\text{H}_2\text{O})][\text{Cr}^{\text{III}}(\text{CN})_6]\cdot\text{H}_2\text{O}$ ,  $[\text{Mn}^{\text{II}}(\textit{rac}\text{-pnH})(\text{H}_2\text{O})][\text{Cr}^{\text{III}}(\text{CN})_6]\cdot\text{H}_2\text{O}$  and  $[\text{Mn}^{\text{II}}(\textit{enH})(\text{H}_2\text{O})][\text{Cr}^{\text{III}}(\text{CN})_6]\cdot\text{H}_2\text{O}$ , where pn = 1,2-diaminopropane and en = ethylenediamine, have consequently been studied (Chapters III-V) using a variety of techniques (chapter II) in the aim finding relations between chirality and magnetism. Chapter I introduces the subject and details of the project.

$[\text{Mn}(R\text{-pnH})(\text{H}_2\text{O})][\text{Cr}(\text{CN})_6]\cdot\text{H}_2\text{O}$  consists of a chiral layered magnetic network based on a square-grid with Mn-NC-Cr connections as its *R*-enantiopure congener,  $[\text{Mn}(S\text{-pnH})(\text{H}_2\text{O})][\text{Cr}(\text{CN})_6]\cdot\text{H}_2\text{O}$ , and is also a ferrimagnet ( $T_C = 38$  K) in its low temperature phase (**RGN-LTP**). It is found to survive two consecutive reversible single crystal-to-single crystal structural phase transitions at 310 (**RGN-LTP** to high temperature phase, **RGN-HTP**) and 360 K (**RGN-HTP** to dehydrated phase, **RGN-DP**) while preserving the same space-group  $P 2_12_12_1$ . The structures of all its phases and some of the magnetic properties were performed on one single crystal. The first transition is of first-order and involves exchange of coordinating and non-coordinating water molecules and Mn bond with the secondary amine nitrogen to the primary one which is promoted by proton-transfer. The second is the complete dehydration producing a 3D-network by additional cyanide bridges. The first transition results in an increase of  $T_C$  to 39 K and the second to 73 K. These are associated with rotation of the easy/intermediate/hard axes going from a/b/c crystallographic axes for **RGN-LTP** to a/c/b for **RGN-HTP** to b/a/c for **RGN-DP**.

$[\text{Mn}(\textit{rac}\text{-pnH})(\text{H}_2\text{O})][\text{Cr}(\text{CN})_6]\cdot\text{H}_2\text{O}$  (**racGN**) crystallizes in the monoclinic achiral *P*

$2_1/m$  space-group having the same square-network of Mn-CN-Cr, and is a soft ferrimagnet ( $T_C = 36$  K). The *S*- and *R*-enantiomers are randomly disordered. **racGN** shows reversible dehydration-rehydration to **racGN-DP** having a three-dimensional network and adopts the achiral orthorhombic *P* mnb space-group. **racGN-DP** is a ferrimagnetic ( $T_C = 70$  K) with enhanced coercive field at 2 K of 64 Oe compared to the virgin sample.

$[\text{Mn}(\text{enH})(\text{H}_2\text{O})][\text{Cr}(\text{CN})_6]\cdot\text{H}_2\text{O}$  (**enGN**) crystallizes in the achiral orthorhombic *P* cmn space-group with similar structure and is a ferrimagnet ( $T_C = 42$  K). **enGN** shows reversible single crystal to an amorphous dehydrated phase, **enGN-DP** is ferrimagnetic ( $T_C = 75$  K).

TGA, DSC, IR and UV-vis provide evidences of the reversibility and reproducibility of the transitions, the order parameter of the transition and the mixed-valency character.

## **Chapter I**

### **Introduction**

# Chapter I

## Introduction

The field of magnetism based on molecules or molecular components is a fast advancing area of research and is of major academic and industrial importance. As the desired long-range magnetic ordering is becoming quite common and can be designed, in some cases, for systems of interest, research is being directed towards improving the critical transition temperatures, the magnetic hardness and the energy products. Critical temperature strongly depend on the number of atoms between paramagnetic center like above 800 K for the oxides (one-atom bridge) and decreases to nearly 200 K for the Prussian blue family having two-atom cyanide bridges while for those containing three-atom bridges  $T_C$  are less than 30 K.<sup>1</sup> Depending on the desired application, the required magnetic hardness, as measured by the coercivity field, can vary from zero Oersted (very soft) for high efficiency smooth motors, to kilo-Oersted for everyday memory devices such as metro tickets, to average hard magnets of ten kilo-Oersted for permanent memory recordings such as music and computer disks, to very hard ones of several tens of kilo-Oersted for writing/erasing heads.<sup>2</sup> The control of this aspect of magnetism is the most difficult. One choice is the anisotropy of the moment carriers. Very anisotropic carriers, for example cobalt(II), are used for obtaining hard magnets while non-anisotropic carriers such as iron(III) or Mn(II) provide soft magnets. The energy product ( $B \times H$  where  $B$  is the remanant magnetization and  $H$  is the coercive field for a square hysteresis loop) of a magnet is proportional to the area within the hysteresis loops, which is dependent on temperature as well as orientation of the magnet in an external field. The coercive field has been discussed earlier, where as the remanant magnetization depends on the quality, the form, the type of magnetic ordering and the spin quantum numbers of the elements of the sample. The order of decreasing remanant magnetization is as follows, ferromagnet, ferrimagnet and canted-antiferromagnet.<sup>3</sup> In addition to these rules that have

been established principally for metals and alloys and are also applied for metal-organic compounds, the latter provide several other properties belonging to the organic part that has been useful in the development of metal-organic magnets. One disadvantage of the latter is the low density of moments. Using paramagnetic ligands is a way to increase the moment density and also to provide closer distances between the different paramagnetic centers. The organic moiety, diamagnetic or paramagnetic, can be used to organize the metal centers into certain crystal types that satisfy the orbital-rule for obtaining long-range magnetic ordering. For example, the dicyanamide anion ( $\text{NC-N-CN}^-$ ) was elegantly used to generate rutile structures with divalent transition metals that satisfy the orthogonality-rule of Goodenough and Kanamori and resulted in ferromagnetism for  $d^7$  and  $d^8$  metals while canted-antiferromagnetism was obtained for  $d^6$  and  $d^5$  metals.<sup>4</sup>

Among the recent developments, single-molecule magnet (SMM) and single-chain magnet (SCM) have been realized, where the major requirement for stabilizing these very peculiar magnetic properties relies on the magnetic anisotropy of the systems. SMM and SCM form a class of materials that bridges the gap between paramagnetism and long-range ordered magnetism covering a wide variety of spin dynamics.<sup>5,6</sup> These compounds are also of importance in the development of nanosized materials.

As pointed out above, the various magnetic properties are thought to be accessible through design of the coordinating ligands, the choice of paramagnetic centers and the control of the structural and magnetic dimensionalities. Working along these lines, much advances have been made which led to the realization of multi-property within one compound. Therefore in parallel to these works, there is a concerted effort to deliberately introduce other properties such as photo-reactivity,<sup>7</sup> guest sensitivity<sup>8</sup> and electrical conduction.<sup>9</sup> Photo-induced magnet was achieved by selecting metals with the appropriate ratio in Prussian blue analogues, showing the photo-activated magnetization and pole inversion by exciting within the appropriate IT - band region.<sup>7a,b,e,g</sup> Guest sensitive magnets have been demonstrated reversible

ferro-antiferromagnet,<sup>8h</sup> Curie temperature increment<sup>8a,b,i,j</sup> as well as spin-crossover critical temperature change<sup>8d,f,l,m</sup> upon guest molecule absorption/desorption. For the magnets combined with electric properties, antiferromagnetic ordering and superconductivity,<sup>9e</sup> ferromagnetic ordering and metallic conductivity,<sup>9a</sup> ferromagnet and ferroelectricity (multiferroics)<sup>9f,g</sup> have been reported. Most unusually observation has been the field-induced superconductivity.<sup>9d</sup>

Magnets with interesting optical properties have also received much attention. Non-linear-optical properties, such as magnetization-induced second harmonic generation (MSHG), are among the first to be realized.<sup>10</sup> The Magneto-Chiral-Dichroism (MChD) effect in absorption or emission is expected for chiral magnets. The MChD effect was first demonstrated in the dehydrated dimethyl sulphoxide solution of chiral structural molecule, [Eu((+ or -)-tfc)<sub>3</sub>] where (+ or -)-tfc is trifluoro-(+ or -)-camphorato.<sup>11</sup>

Beside them, the chiral magnet is of special interest. For the magnetism, absence of centro-symmetry can also provide pathways for the asymmetric Dzyaloshinsky-Moriya (DM) interaction to operate and can result in inducing "chirality" in the magnetic structure. The DM interaction was first introduced by Dzyaloshinsky and consequently modified by Moriya to explain the weak-ferromagnetism in  $\alpha$ -Fe<sub>2</sub>O<sub>3</sub>.<sup>12</sup> Up to date, several chiral magnets have been synthesized due to the spontaneous resolution phenomenon upon crystallization by the use of auxiliary chiral ligands. In one case, these magnets were made from ligands without an optically active center, such as those with a twisting ligand (P or M) or metal-tris(oxalate) ( $\Lambda$  or  $\Delta$ ) as well as from simple formate anion.<sup>13</sup> Meanwhile, in another case from ligands with an optically active center, such as simple amines,<sup>14,15</sup> organic radicals,<sup>16</sup> or naturally available compounds.<sup>17</sup> Very recently, new chirality induced porous achiral magnet by absorption of the chiral alcohol was reported.<sup>18</sup>

Among these strategies, our group is working on auxiliary ligand method with Prussian blue building blocks and this work led to several chiral magnets belonging to different crystal

classes and systems. Among them is  $[\text{Mn}^{\text{II}}(\text{S-pnH})(\text{H}_2\text{O})][\text{Cr}^{\text{III}}(\text{CN})_6]\cdot(\text{H}_2\text{O})$  (**SGN-LTP**) which we abbreviated to ‘GN for green needle’.<sup>15</sup> This compound has several facets to it, which are incorporated by choice; it is heterometallic class-II mixed-valent, it has paramagnetic centers of different spin, and it chiral by virtue of the presence of only one enantiomer in the structure. It is a soft ferrimagnet ( $T_{\text{C}} = 38 \text{ K}$ ;  $H_{\text{coercive}} < 10 \text{ Oe}$ ). Furthermore, neutron diffraction indicates the chiral magnetic structure ( $P 2_1 2_1' 2_1'$ )<sup>19a</sup> and  $\mu$ -SR results are consistent with chiral magnetic structure,<sup>19b</sup> moreover, giant non-linear third harmonic ac-susceptibilities were found.<sup>19c</sup>

To develop this area, further experiment on GN as well as synthesizing achiral reference samples had been invoked to elucidate the sole effect of chirality. Surprisingly, GN showed other ground states as a function of the temperature with reversible single crystal-to-single crystal transformations,<sup>20</sup> increasing number of the chiral magnet. In this thesis, we discuss on the crystal structure of GN and its structural transformations and the accompanying physical properties (chapter III). Consequently, successfully synthesized GN reference sample *rac*GN (chapter IV) and *en*GN (chapter V) with structural and physical properties changes are described.

## **Chapter II**

### **Experimental Section**



## Chapter II

### Experimental Section

#### II-1. Synthesis of $\text{K}_3[\text{Cr}(\text{CN})_6]$

This compound was synthesized by a slight modification to the reported procedure.<sup>21</sup> (Caution: Potassium cyanide is very toxic and should be used only in a well-ventilated hood and manipulated with latex gloves). 50 mL of an aqueous solution of KCN (13.02 g, 200 mmol) was heated to 80 °C and the added drop by drop to a 50 mL aqueous solution of  $\text{CrCl}_3 \cdot 6\text{H}_2\text{O}$  (15.9 g, 48.9 mmol). The dark-orange solution formed was filtered through a Celite®545 column until the filtrate loses its turbidity.

In a different dry flask Hg/Zn amalgam was prepared by adding 4 mL of 0.5 M HCl to a mixture of  $\text{HgCl}_2$  (0.2 g, 0.74 mmol) and Zn powder (2.0 g, 30.6 mmol) (Warning: This is a fuming reaction). After mixing, the solvent was removed by decantation.

The experiments that followed were performed under dry nitrogen. To the amalgam, 12 mL of an aqueous solution of  $\text{CrCl}_3 \cdot 6\text{H}_2\text{O}$  (0.266 g, 1.0 mmol) was added and stirred until the color of the solution has changed to pale-blue. The reduced chromium solution was added to the orange  $\text{CrCl}_3$ -KCN solution prepared above. The resulting mixture was stirred for 3 hours and the color of the solution changed from dark-orange to an orange-yellow. After the color change, the solution was exposed to air and stirred overnight. The color of the solution reverts back to dark-orange. 550 mL MeOH was then added to the solution to yield a yellow precipitate. This precipitate was filtered and washed with EtOH and then ether. The solid was dissolved in a minimum amount of iced water and filtered through Celite. MeOH was then added to it while stirring to give a yellow precipitate, which was filtered and washed with

EtOH and ether. Yield 1.91 g (5.87 mmol), 11.8% (5.87 / 49.9 mmol based on Cr<sup>III</sup>). The presence of this product was confirmed and its quality was verified from UV-vis spectra using an aqueous solution containing 5.04 mM of the product (0.04102 g, 0.126 mmol in 25 mL of H<sub>2</sub>O). Obs.  $\lambda = 378.5$  nm ( $\epsilon = 89.6$  mol<sup>-1</sup> L cm<sup>-1</sup>),  $\lambda = 306.5$  nm ( $\epsilon = 66.4$  mol<sup>-1</sup> L cm<sup>-1</sup>); Ref.  $\lambda = 377$  nm ( $\epsilon = 85.9$  mol<sup>-1</sup> L cm<sup>-1</sup>),  $\lambda = 307$  nm ( $\epsilon = 59.5$  mol<sup>-1</sup> L cm<sup>-1</sup>).<sup>1</sup>

## II-2.1. Synthesis of *R*-pn·2HCl

This compound was synthesized with slight modification to that referenced in the book.<sup>22</sup> A solution containing *L*-(+)-tartaric acid, (+tartH<sub>2</sub>, 289 g, 1.92 mol) in 380 mL of H<sub>2</sub>O was added to 81.8 mL of *rac*-1,2-diaminopropane, (*rac*-pn,  $d = 0.87$  g/mol, 0.961 mol) to yield a white precipitate. The solution with precipitate was heated to  $\approx 80$  °C until complete dissolution of the solid and then cooled slowly to 0 °C with vigorous stirring to yield a white precipitate. This precipitate was filtered, washed with iced water and then re-dissolved in 800 mL of H<sub>2</sub>O at 0 °C. Recrystallization of the solid was then performed very slowly with the Erlenmeyer flask wrapped by a towel and aluminum foil and left overnight, followed by cooling in ice while it is vigorously stirred. The white precipitate was filtered and washed with iced water. This recrystallization was repeated three more times from 720, 480 and 480 mL of H<sub>2</sub>O, respectively. The final white precipitate *R*-pnH<sub>2</sub>[+tart]<sub>2</sub>·2H<sub>2</sub>O (170 g, 0.414 mol) was partially dissolved in 200 mL of H<sub>2</sub>O and Ca(OH)<sub>2</sub> (67.2 g, 0.907 mol) was added drop-wise to the suspension with vigorous stirring. The mixture was kept stirring overnight at 40 °C. The resulting heavy precipitate was filtered and washed with iced water and all the filtrate was collected. KOH solid was added to the filtrate until the solution separated into two-layers. The upper layer was separated and to it was added 70 mL 37% HCl ( $d = 1.19$

g/mL, 0.845 mol). The mixed solution was evaporated until a white precipitate was observed. EtOH was added to the suspension to give a heavier white precipitation. The precipitate was filtered and washed with EtOH and ether. Yield 28.0 g, 39.6% (0.19 / 0.48 mmol based on *R*-pn).

Optical purity was obtained from measurement on a polarimeter using a 10 mL aqueous solution containing the product (2.00 g,  $\alpha = 4.0 \text{ deg. mL g}^{-1} \text{ dm}^{-1}$ , theoretical value = 0.800 deg for 1 dm light pass) with reference to 100 mL aqueous solution of sucrose (1.48 g,  $\alpha = 66.5 \text{ deg. mL g}^{-1} \text{ dm}^{-1}$ , theoretical value = 0.984 deg for 1 dm light pass). The observed value of *R*-pn·2HCl / Sucrose was 0.78 while theoretical value is 0.82. Assuming that by-product is *S*-pn·2HCl, enantio-excess is calculated at 96%.

## II-2.2. Synthesis of *S*-pn·2HCl

This compound was synthesized from same protocol with *R*-pn·2HCl with using *D*-(-)-tartaric acid instead of *L*-(+)-tartaric acid.

A solution containing *D*-(-)-tartaric acid, (-tartH<sub>2</sub>, 300 g, 2.00 mol) in 400 mL of H<sub>2</sub>O was added to 95 mL of *rac*-1,2-diaminopropane, (*rac*-pn,  $d = 0.87 \text{ g/mol}$ , 1.11 mol) to yield a white precipitate. The solution with precipitate was heated to  $\approx 80 \text{ }^\circ\text{C}$  until complete dissolution of the solid and then cooled slowly to  $0 \text{ }^\circ\text{C}$  with vigorous stirring to yield a white precipitate. This precipitate was filtered, washed with iced water and then re-dissolved in 700 mL of H<sub>2</sub>O at  $0 \text{ }^\circ\text{C}$ . Recrystallization of the solid was then performed very slowly with the Erlenmeyer flask wrapped by a towel and aluminum foil and left overnight, followed by cooling in ice while it is vigorously stirred. The white precipitate was filtered and washed with iced water. This recrystallization was repeated three more times with 700 mL of H<sub>2</sub>O.

The final white precipitate  $S\text{-pnH}_2[-\text{tart}]_2 \cdot 2\text{H}_2\text{O}$  (172 g, 0.446 mol) was partially dissolved in 200 mL of  $\text{H}_2\text{O}$  and  $\text{Ca}(\text{OH})_2$  (67.2 g, 0.907 mol) was added drop-wise to the suspension with vigorous stirring. The mixture was kept stirring overnight at 40 °C. The resulting heavy precipitate was filtered and washed with iced water and all the filtrate was collected. KOH solid was added to the filtrate until the solution separated into two-layers. The upper layer was separated and to it was added 80 mL 37% HCl ( $d = 1.19 \text{ g/mL}$ , 0.966 mol). The mixed solution was evaporated until a white precipitate was observed. EtOH was added to the suspension to give a heavier white precipitation. The precipitate was filtered and washed with EtOH and ether. Yield 25.8 g, 31.8% (0.175 / 0.55 mmol based on  $S\text{-pn}$ ).

Optical purity was obtained from measurement on a polarimeter using a 25 mL aqueous solution containing the product (2.97 g,  $\alpha = -4.0 \text{ deg. mL g}^{-1} \text{ dm}^{-1}$ , theoretical value =  $-0.475 \text{ deg}$  for 1 dm light pass) with reference to 25 mL aqueous solution of sucrose (8.65 g,  $\alpha = 66.5 \text{ deg. mL g}^{-1} \text{ dm}^{-1}$ , theoretical value =  $23.0 \text{ deg}$  for 1 dm light pass). The observed value of  $S\text{-pn} \cdot 2\text{HCl}$  / Sucrose was  $-0.02042$  while theoretical value is  $-0.02064$ . Assuming that by-product is  $S\text{-pn} \cdot 2\text{HCl}$ , enantio-excess is calculated at 99%.

### II-2.3. Synthesis of $rac\text{-pn} \cdot 2\text{HCl}$

7.0 mL of  $rac\text{-1,2-diaminopropane}$  ( $d = 0.87 \text{ g/mol}$ , 82.6 mmol) was added to 13.6 mL of 37 % HCl ( $d = 1.19 \text{ g/mL}$ , 167 mmol). The mixture was evaporated to yield a white powder. It was then dissolved into a minimum amount of hot water. The concentrated hot solution was cooled down to room temperature and then added to EtOH while stirring until no precipitation occurs. The precipitate was filtered and washed with EtOH and ether. Yield 7.55 g, 62% (51.3 / 82.6 mmol)

## II-2.4. Synthesis of en·2HCl

A solution of 10 mL of ethylenediamine ( $d = 0.899$  g/mL, 150 mmol) in 30 mL of H<sub>2</sub>O was added to 30 mL of 37% HCl ( $d = 1.19$  g/mL, 362 mmol). The mixture was evaporated to yield a white powder, which was then dissolved in a minimum amount of hot water. The concentrated hot solution was cooled down to room temperature and EtOH was added while stirring until no more white precipitation occurs. The precipitate was filtered and washed with EtOH and ether. Yield 19.1 g, 96% (144 / 150 mmol).

## II-3.1. Synthesis of [Mn(*R*-pnH)(H<sub>2</sub>O)][Cr(CN)<sub>6</sub>]·H<sub>2</sub>O (RGN-LTP)

This compound was synthesized by a slightly modified method to that reported.<sup>15</sup> For this part of the synthesis, all manipulations were performed under an argon atmosphere. 2 mL of aqueous *R*-pn·2HCl (368 mg, 2.5 mmol) and K<sub>3</sub>[Cr(CN)<sub>6</sub>] (203 mg, 0.625 mmol) were mixed with 0.5 mL of 8.0 M KOH (4 mmol) and the mixture was placed at the bottom of a glass tube (14 mm inner diameter). 1.5 mL of H<sub>2</sub>O-EtOH (3:1) was then layered on top of this mixture, followed by layering with 2.5 mL of H<sub>2</sub>O-EtOH (1:3) solution of MnCl<sub>2</sub>·4H<sub>2</sub>O (372 mg, 1.88 mmol). The glass tube was sealed and kept in a dark place. After two months, green needle plate crystals were harvested. This method also yields cubic crystals of Prussian blue as byproduct in proportion not exceeding 10%. The crystals were filtered and washed with H<sub>2</sub>O, EtOH and ether. The desired crystals were separated manually under an optical microscope for further measurements. Yield 175 mg (including cubic crystal), 74.9% (0.468 / 0.625 mmol based on K<sub>3</sub>[Cr(CN)<sub>6</sub>]). Anal. Calcd for **RGN-LTP**, C<sub>9</sub>H<sub>15</sub>CrMnN<sub>8</sub>O<sub>2</sub>: %Calc. C, 28.89; H, 4.04; N, 29.94. Found: C, 28.90; H, 3.95; N, 30.34.

### II-3.2. Synthesis of $[\text{Mn}(\text{S-pnH})(\text{H}_2\text{O})][\text{Cr}(\text{CN})_6]\cdot\text{H}_2\text{O}$ (SGN-LTP)

This compound was synthesized from same protocol with **RGN-LTP** with using *S*-pn·2HCl instead of *R*-pn·2HCl. For this part of the synthesis, all manipulations were performed under an argon atmosphere. 3.0 mL of aqueous *S*-pn·2HCl (494 mg, 3.36 mmol) and  $\text{K}_3[\text{Cr}(\text{CN})_6]$  (0.225 g, 0.69 mmol) were mixed with 0.4 mL of 8.0 M KOH (3.2 mmol) and the mixture was placed at the bottom of a glass tube (10 mm inner diameter). 2.6 mL of  $\text{H}_2\text{O}$ -EtOH (3:1) was then layered on top of this mixture, followed by layering with 3.4 mL of  $\text{H}_2\text{O}$ -EtOH (1:3) solution of  $\text{MnCl}_2\cdot 4\text{H}_2\text{O}$  (501 mg, 2.53 mmol). The glass tube was sealed and kept in a dark place. After two months, green needle plate crystals were harvested. This method also yields cubic crystals of Prussian blue as byproduct in proportion not exceeding 10%. The crystals were filtered and washed with  $\text{H}_2\text{O}$ , EtOH and ether. The desired crystals were separated manually under an optical microscope for further measurements. Yield 131 mg (including cubic crystal), 50.7% (0.350 / 0.690 mmol based on  $\text{K}_3[\text{Cr}(\text{CN})_6]$ ). Anal. Calcd for **SGN-LTP**,  $\text{C}_9\text{H}_{15}\text{CrMnN}_8\text{O}_2$ : %Calc. C, 28.89; H, 4.04; N, 29.94. Found: C, 28.95; H, 3.85; N, 29.96.

### II-3.3. Synthesis of $[\text{Mn}(\text{rac-pnH})(\text{H}_2\text{O})][\text{Cr}(\text{CN})_6]\cdot\text{H}_2\text{O}$ (racGN)

All manipulations were performed under an argon atmosphere. 0.5 mL of aqueous *rac*-pn·2HCl (147 mg, 1.0 mmol) and  $\text{K}_3[\text{Cr}(\text{CN})_6]$  (16.3 mg, 0.05 mmol) was mixed to 0.1 mL of 8.0 M KOH (0.8 mmol) and the mixture was placed at the bottom of a glass tube (6 mm inner diameter). 0.4 mL of  $\text{H}_2\text{O}$ -EtOH (3:1) was then layered on top of this mixture, followed by layering with 0.5 mL of  $\text{H}_2\text{O}$ -EtOH (1:3) solution of  $\text{MnCl}_2\cdot 4\text{H}_2\text{O}$  (74.2 mg, 0.375 mmol). The glass tube was sealed and kept in a dark place. After a few weeks, green

needle plate crystals were harvested. This method also yields cubic crystals of Prussian blue as byproduct in variable proportion not exceeding 10%. The crystals were filtered and washed with H<sub>2</sub>O, EtOH and ether. The desired crystals were separated manually under an optical microscope for further measurements. Yield 14.1 mg (including cubic crystal), 76% (0.038 / 0.05 mmol based on K<sub>3</sub>[Cr(CN)<sub>6</sub>]). Anal. Calcd for *racGN*, C<sub>9</sub>H<sub>15</sub>CrMnN<sub>8</sub>O<sub>2</sub>: %Calc. C, 28.89; H, 4.04; N, 29.94. Found: C, 28.84; H, 4.37; N, 29.97.

#### II-3.4. Synthesis of [Mn(enH)(H<sub>2</sub>O)][Cr(CN)<sub>6</sub>]·H<sub>2</sub>O (*enGN*)

For this part all manipulations were performed under an argon atmosphere. 2 mL of aqueous en·2HCl (332 mg, 2.5 mmol) and K<sub>3</sub>[Cr(CN)<sub>6</sub>] (203 mg, 0.625 mmol) were mixed with 0.5 mL of 8 M KOH (4 mmol) and the mixture was placed at the bottom of a glass tube (14 mm inner diameter). 1.5 mL of H<sub>2</sub>O-EtOH (3:1) was then layered on top of this mixture, followed by layering with 2.5 mL of H<sub>2</sub>O-EtOH (1:3) solution of MnCl<sub>2</sub>·4H<sub>2</sub>O (372 mg, 1.88 mmol). The glass tube was sealed and kept in a dark place. After a few weeks, green needle plate crystals were harvested. This method also yields cubic crystals of Prussian blue as byproduct in proportion not exceeding 10%. The crystals were filtered and washed with H<sub>2</sub>O, EtOH and ether. The desired crystals were separated manually under an optical microscope for further measurements. Yield 170.6 mg (including cubic crystal), 75.8% (0.474 / 0.625 mmol based on K<sub>3</sub>[Cr(CN)<sub>6</sub>]) Anal. Calcd. for *enGN*, C<sub>8</sub>H<sub>13</sub>CrMnN<sub>8</sub>O<sub>2</sub>: %Calc. C, 26.52; H, 4.17; N, 30.98. Found: C, 26.57; H, 3.98; N, 31.01.

#### **II-4. Elemental analyses**

Elemental analyses for C, H and N were performed on a Perkin-Elmer 2400II at the Natural Science Center for Basic Research and Development (N-BARD), Hiroshima University.

#### **II-5. Infrared spectroscopy**

Infrared spectra were recorded by transmission through KBr disks containing ca. 0.5 % of the compounds using a HORIBA FT-IR spectrometer FT-720. For **RGN-HTP**, the KBr pressed disk was warmed to 323 K for 2 days before measurement. For **RGN-DP**, **racGN-DP** and **enGN-DP**, some powdered KBr containing the virgin sample was vacuumed at 383 K for 2 hours, and then pressed into disk. For **RGN-HP** and **racGN-HP**, each virgin sample was heated to 365 K at a rate of 1 K/min, exposed to air for overnight, then mixed with KBr and pressed into disk. For **RGN-HP** virgin sample was heated to 365 K at a rate of 1 K/min, soaked into water, dried under nitrogen, then mixed with KBr and pressed into disk. For **racGN-DP** (2nd), some powdered KBr containing **racGN-HP** was vacuumed at 383 K for 2 hours, and then pressed into disk.

#### **II-6. Polarimetry**

Optical purity was measured by transmission through a solution (1 dm light pass) using an ADP220 polarimeter (Bellingham and Stanley Ltd).



## II-7. UV-Vis spectroscopy

UV-vis spectra of  $K_3[Cr(CN)_6]$  was measured by transmission through an aqueous solution in a quartz cell (1 cm light pass) using a SHIMADZU UV 160A spectrometer. UV-vis absorption spectra of **RGN-LTP** were recorded by transmission through a single crystal (1.5 x 5 mm<sup>2</sup> and thickness of ca. 0.2 mm) held on cut slots between two aluminum sheets by use of an UVIKON-XL of BIOTEK Instruments. Due to the high absorption below 400 nm, the transmission was too low to allow for any measurement to be performed.

## II-8. Magnetic measurements

Magnetic measurements were carried out by use of a Quantum Design MPMS-5S SQUID magnetometer. Diamagnetic corrections were estimated using Pascal constants,<sup>23,24</sup> and background correction by experimental measurement of an empty gelatin capsule.

Magnetic properties for polycrystalline samples for **RGN-LTP**, **SGN-LTP**, *rac*GN and **en**GN were collected by in-situ measurement except for the rehydration of **en**GN-DP. The sample of **RGN-LTP** was transformed from virgin **RGN-LTP** to quenched **RGN-HTP**, relaxed **RGN-LTP**, dehydrated **RGN-DP** and rehydrated **RGN-HP**, sequentially. After each transformation, the phase was verified by locating its magnetic critical temperature. The **RGN-HTP** was obtained by warming the sample of **RGN-LTP** from 300 to 312 K at a rate of 0.25 K/min and cooled down to 100 K at a rate of -10 K/min. The relaxed **RGN-LTP** was obtained by annealing the sample from 280 to 295 K and back to 280 K at a rate of 0.25 K/min. **RGN-DP** was obtained by warming the sample from 310 to 360 K at a rate of 0.5 K/min and purged for one hour at 360 K. **RGN-HP** was obtained by exposing to the air for 1 week. The *S*-isomer, **SGN-LTP** was treated with same procedure for **RGN-LTP**. The sample

of *racGN* was transformed from *racGN* to dehydrated *racGN-DP*, rehydrated *racGN-HP*, and dehydrated *racGN-DP* (2nd), sequentially. The *racGN-DP* was obtained by heating the sample from 310 to 360 K at a warming rate of 0.5 K/min. Then, *racGN-HP* was obtained by exposing to the air for 1 month, then the phase was transformed into *racGN-DP* (2nd) by heating the sample from 310 to 360 K at a warming rate of 0.5 K/min. The sample of *enGN* was collected for virgin *enGN*, followed by those of the dehydrated *enGN-DP*, then rehydrated *enGN-HP*. The dehydrated *enGN-DP* was obtained by heating the virgin sample in a flow of helium from 310 to 360 K at a warming rate of 0.5 K/minute in the SQUID machine, then the dehydrated sample was soaked in distilled water to recover the initial state *enGN-HP*. The phase state was verified by locating the critical temperature after each transformation.

Zero-field-cooled and field-cooled measurements were performed in an applied field of 5 Oe and magnetic susceptibility were measured in an applied field of 100 Oe. Magnetic susceptibilities for quenched *RGN-HTP* were collected on cooling from 100 to 2 K, followed by warming from 106 to 300 K. For Dehydrated samples *RGN-DP*, *racGN-DP*, *racGN-DP* (2nd), and *enGN-DP*, magnetic susceptibilities were collected on cooling from 360 to 2 K. For the other phases, magnetic susceptibilities were collected on cooling from 300 to 2 K. Isothermal magnetization at 2 K was measured for each phase from -50 to 50 kOe.

Isothermal initial magnetizations were collected at 2 K on one single crystal, which were aligned along crystallographic axes determined by the aid of single crystal X-ray diffraction, from 0 to 50 kOe. Two single crystals were used to complete the full set of measurements. Measurements were done for *b*-axis (*RGN-LTP*), *c*-axis (*RGN-LTP*), *c*-axis (*RGN-HTP*), *b*-axis (*RGN-HTP*), *a*-axis (*RGN-LTP*), *a*-axis (*RGN-HTP*), *a*-axis (*RGN-DP*), *b*-axis

(**RGN-DP**) and *c*-axis (**RGN-DP**), sequentially. The crystallographic axes were determined more accurately from the minimum or maximum point of angular dependence of the magnetization. The phases were determined by their magnetic critical temperatures. The two crystals were covered with methyl methacrylate polymer (PMMA) using CH<sub>2</sub>Cl<sub>2</sub>.

The first single crystal (**RGN-LTP**) was set to the sample rotor with the *a*-axis parallel to the rotation axis, and MH curve for *b*-axis (**RGN-LTP**) was first measured and then the crystal was rotated by 90° followed by measuring the *c*-axis (**RGN-LTP**). In this orientation the virgin **RGN-LTP** was transformed into quenched **RGN-HTP** by warming from 290 K to 312 K at a rate of 0.25 K/min and cooled down to 100 K at a cooling rate of -10 K/min. MH curve for *c*-axis (**RGN-HTP**) was measured and the crystal was rotated by 90° followed by measuring along the *b*-axis (**RGN-HTP**). The quenched **RGN-HTP** was annealed to the relaxed **RGN-LTP** by warming the sample from 280 to 295 K and cooling to 280 K at a rate of 0.25 K/min. The same crystal (**RGN-LTP**) was remounted on the sample rotor with the *c*-axis parallel to the rotation axis and MH curve was measured for *a*-axis (**RGN-LTP**). The relaxed-**LTP** was transformed into quenched-**HTP** by warming from 290 to 312 K at a rate of 0.25 K/min twice and cooled down to 100 K at a cooling rate of -10 K/min. MH curve for *a*-axis (**RGN-HTP**) was measured. Then, the quenched-**HTP** was dehydrated by heating from 310 to 360 K at a rate of 2 K/min. MH curve for *a*-axis (**RGN-DP**) was measured and then the crystal was rotated by 90° followed by measuring the *b*-axis (**RGN-DP**). The second crystal was set to sample rotor with the *a*-axis parallel to the rotation axis. The crystal was dehydrated by heating from 310 to 360 K at a rate of 2 K/min, MH curves for *c*-axis (**RGN-DP**) was measured.

## II-9. Thermogravimetric and differential thermal analyses

Thermogravimetric and differential thermal analyses were performed on 10.060, 10.237, 9.799 and 10.574 mg of *RGN-LTP*, *SGN-LTP*, *racGN* and *enGN* sample, respectively, using a Rigaku Instrument TG8120 operating under dry nitrogen with heating from 290 to 363-380 K at a rate of 1 K/min, and cooling down to 290 K at a rate of 10 K/min. After cooling, the dehydrated sample was exposed to air overnight for *RGN-LTP*, *SGN-LTP*, and *racGN*. The dehydrated sample of *enGN-DP* was exposed to high humidity air (humidity  $\approx$  93%, temperature  $\approx$  310 K) for overnight. Further measurements were performed to higher temperatures by use of a Perkin-Elmer Pyris 6 TGA operating under dry nitrogen at a heating rate of 5 K/min for 21.841, 15.497 and 18.343 mg of *RGN-LTP*, *racGN*, and *enGN* sample, respectively.

## II-10. Differential scanning calorimetry

Calorimetric experiments were performed at two different warming rates using a Rigaku Instrument DSC8230 under nitrogen atmosphere. For the *RGN-LTP*, measurement with slow warming rate of 0.25 and 2 K/min was performed on a sample of 20.009 and 4.990 mg with 20.693 and 5.442 mg of  $\text{Al}_2\text{O}_3$  as references, respectively. For the *racGN*, measurement at a warming rate of 1 K/min was performed on 21.844 mg of sample which are tightly packed in an aluminum pan with lid with 10.42 mg of Aluminum lid as a reference.

## II-11. Powder X-ray diffraction

The powder X-ray diffraction patterns were measured on a Rigaku Rint 2000 system using  $\text{Cu-K}\alpha$  radiation and employing a scan rate of  $4.0^\circ/\text{min}$  and step of  $0.02^\circ$ . For the *RGN-LTP*,

the sample was transformed from the virgin **RG**N-LTP to quenched **RG**N-HTP, relaxed **RG**N-LTP, dehydrated **RG**N-DP and rehydrated **RG**N-LTP, sequentially. The quenched **RG**N-HTP was obtained by placing the virgin **RG**N-LTP in a heated desiccator and kept at 315 K for 1 hour. The relaxed **RG**N-LTP was obtained by placing the sample in a refrigerator operating at 283 K and kept for 2 hours. **RG**N-DP was obtained by placing relaxed **RG**N-LTP in a heated desiccator at 363 K for 30 min under nitrogen. Rehydrated **RG**N-HP was obtained by exposing the **RG**N-DP sample to air for 30 min. The *S*-isomer, **SG**N-LTP was treated with same protocol with **RG**N-LTP.

For the *rac*GN, the sample was transformed from virgin *rac*GN to dehydrated *rac*GN-DP, rehydrated *rac*GN-HP, and dehydrated *rac*GN-DP (2nd), sequentially. Dehydrated *rac*GN-DP was obtained by placing the sample in a heated desiccator kept at 363 K for 10 min under nitrogen. Rehydrated *rac*GN-HP was obtained by exposing to air for 30 min, then this hydrated phase was placed in a heated desiccator kept at 363 K for 10 min under nitrogen again to transform into *rac*GN-DP. For the **en**GN, the sample was transformed from virgin **en**GN to dehydrated **en**GN-DP, and then rehydrated **en**GN-HP. Dehydrated **en**GN-DP was obtained by placing the sample in a heated desiccator kept at 363 K for 10 min under nitrogen. Rehydrated **en**GN-HP was obtained by exposing to air for 1 hour. The simulated patterns were calculated from the single crystal X-ray data using RIETAN-2000.<sup>29</sup>

## II-12. Single crystal X-ray diffraction

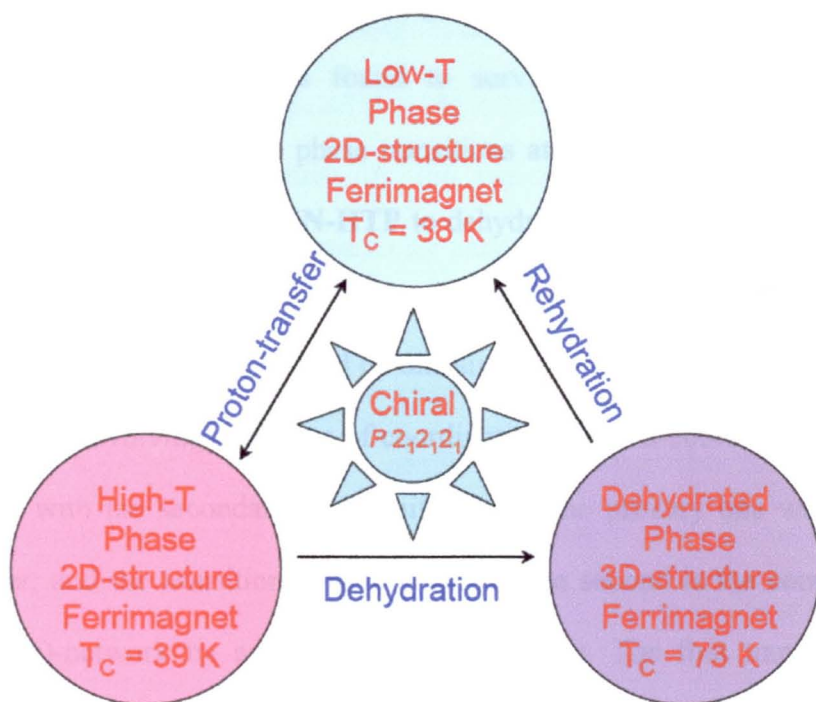
All the diffraction data were collected by in-situ measurements using a Bruker SMART-APEX diffractometer equipped with a CCD area detector and

graphite-monochromated MoK $\alpha$  radiation,  $\lambda = 0.71073 \text{ \AA}$ ,  $\omega$ -scan mode ( $0.3^\circ$ — steps). Semi-empirical absorption corrections on Laue equivalents were applied. The structures were solved by direct methods and refined by full-matrix least-squares against  $F^2$  of all data using SHELX-97. Hydrogen atoms on nitrogen and carbon atoms were included in calculated positions and not refined for **RGN** series. Meanwhile, only C6 atom for **racGN**, C4 and C5 atoms for **enGN** were included due to static disorder for the other series. The positions of the hydrogen atoms on oxygen atom were located from the different Fourier map unless the refinement is unstable. All the atoms were refined anisotropically except for hydrogen atoms.

For the **RGN-LTP**, the crystals were found to break during temperature cycle and this was associated with the different hardness when the crystals were glued to the glass fiber using araldite. Furthermore, direct flow of nitrogen onto the crystal during intensity measurement for **RGN-HTP** at 309 K where the structural phase transition was observed gradually affects the quality of the diffraction peaks. This occurs only in the first transformation from virgin **RGN-LTP** to **RGN-HTP**. To circumvent the two difficulties two precautions were taken. One is to wrap the selected crystal with a thin polyethylene sheet (cling film) without using glue and this is then glued to the glass fiber with araldite at one end and the other end is left open; otherwise it was not possible to properly dehydrate the crystal in-situ. The second problem was resolved by use of a clear drinking straw around the crystal. Neither of these appears to affect the diffracted intensities. For the **racGN** and **enGN**, the crystals were glued to the glass fiber using araldite.

## Chapter III

### **[Mn(*R*-pnH)(H<sub>2</sub>O)][Cr(CN)<sub>6</sub>]·H<sub>2</sub>O: A Chiral Soft Ferrimagnet Displaying Two Reversible Single Crystal-to-Single Crystal Transformations, Proton Transfer and Increment of Curie Temperature**



## Chapter III

### **[Mn(*R*-pnH)(H<sub>2</sub>O)][Cr(CN)<sub>6</sub>]·H<sub>2</sub>O: A Chiral Soft Ferrimagnet Displaying Two Reversible Single Crystal-to-Single Crystal Transformations, Proton Transfer and Increment of Curie Temperature**

#### **III-1. Abstract**

We report the structural and thermal, optical and magnetic properties of the *S*-enantiopure chiral layered magnetic network [Mn(*S*-pnH)(H<sub>2</sub>O)][Cr(CN)<sub>6</sub>]·H<sub>2</sub>O where pn = 1,2-diaminopropane. In addition to the common structural and magnetic features of its *S*-enantiopure congener, [Mn(*R*-pnH)(H<sub>2</sub>O)][Cr(CN)<sub>6</sub>]·H<sub>2</sub>O, consisting of a square-grid Mn-NC-Cr connections and a ferrimagnetic ground state ( $T_C = 38$  K) in its low temperature phase (***RGN-LTP***), the former is found to survive two consecutive reversible single crystal-to-single crystal structural phase transitions at 310 (***RGN-LTP*** to high temperature phase, ***RGN-HTP***) and 360 K (***RGN-HTP*** to dehydrated phase, ***RGN-DP***) while preserving the same space-group  $P 2_12_12_1$ . The structure determinations of all its phases and some of the magnetic properties were all performed on one single crystal in each case. The first transition is a subtle change involving exchange of coordinating and non-coordinating water molecules and Mn bond with the secondary amine nitrogen to the primary one which is assisted by proton-transfer, and the transition is of first-order. The second is the complete dehydration producing a 3D-network by additional cyanide bridges. The first transition results in an increase of  $T_C$  to 39 K and the second to 73 K. These are associated with rotation of the easy/intermediate/hard axes going from *a/b/c* crystallographic axes for ***RGN-LTP*** to *a/c/b* for ***RGN-HTP*** to *b/a/c* for ***RGN-DP***. TGA, DSC, IR and UV-vis spectroscopy provide additional evidences of the reversibility and reproducibility of the transitions as well as the thermodynamic order parameter of the transition and the mixed-valency character.



### III-2. Introduction

The field of magnetism based on molecules or molecular components is a fast advancing area research and is of major academic and industrial importance. As the desired long-range magnetic ordering is becoming quite common and can be designed, in some cases, for systems of interest, research is being directed towards improving the critical transition temperatures, the magnetic hardness and the energy products. These are thought to be accessible through design of the coordinating ligands, the choice of paramagnetic centers and the control of the structural and magnetic dimensionalities. These advances have led to the realization of multiproperty within one compound. Therefore in parallel to these works, there is a concerted effort to deliberately introduce other properties such as electrical<sup>9</sup> or proton conduction,<sup>25</sup> optical facets such as chirality,<sup>14-18</sup> non-linearity<sup>26</sup> or luminescence,<sup>27</sup> and most recently, porosity.<sup>28</sup> While several successes have been recorded, there is still major work in progress in a number of laboratories around the world. We have concentrated on introducing chirality in modified Prussian blue by the use of enantiopure amine ligands or in metal-organic radical systems in the search for new phenomena where coupling of magnetism with the chirality can be evidenced. Our work has led to several chiral magnets belonging to different crystal classes. Among them is  $[\text{Mn}^{\text{II}}(\text{S-pnH})(\text{H}_2\text{O})][\text{Cr}^{\text{III}}(\text{CN})_6]\cdot\text{H}_2\text{O}$  (**SGN-LTP**) which we abbreviated to ‘GN for green needle’.<sup>15</sup> This compound has several facets to it, which are incorporated by choice; it is heterometallic class-II mixed-valent, it has paramagnetic centers of different spin, and it is chiral by virtue of the presence of only one enantiomer in the structure. It is a soft ferrimagnet ( $T_{\text{C}} = 38 \text{ K}$ ;  $H_{\text{coercive}} < 10 \text{ Oe}$ ). Furthermore, neutron diffraction, ESR,  $\mu$ -SR and non-linear ac-susceptibilities reveal there is new physical phenomenon not observed previously that is associated with the chirality and magnetic order.<sup>19</sup> In order to verify such findings we have undertaken the synthesis of its racemic and its congener containing the *R*-enantiomer ligand,

$[\text{Mn}^{\text{II}}(\text{R-pnH})(\text{H}_2\text{O})][\text{Cr}^{\text{III}}(\text{CN})_6]\cdot\text{H}_2\text{O}$ . The structural, thermal, optical and magnetic properties

of the latter form the content of the present chapter.

This compound displays an amazing range of interesting properties that have not been encountered in any compounds of the sort. The crystals are robust and are able to survive two structural phase transitions reversibly, including dehydration and rehydration, through a series of sequences where eight crystal structures have been determined in its different forms on the same single crystal while preserving the same space-group. The associated magnetic properties have also been studied thoroughly. Interestingly, one of the phase transitions involves a rarely observed proton-transfer mechanism resembling a biological system such as a muscle and is thermodynamically of first-order. And the dehydration changes the crystal system from a 2D magnetic dimensionality to one of 3D and is accompanied by a giant leap of the Curie temperature from 38 through 39 and finally 73 K.

### **III-3. Results and discussion**

Considering the wide range of techniques used to elucidate the complexities in the structures and the properties through two reversible modifications, we present the experimental data and their discussions for the thermal, structural, optical and magnetic properties in-turn. Also due to orientation dependence of the magnetic properties we first present those studied on powdered samples and then on the aligned single crystals.

#### **III-3.1. Synthesis**

The original reported synthesis of green needles of  $[\text{Mn}(\text{S-pnH})(\text{H}_2\text{O})][\text{Cr}(\text{CN})_6]\cdot\text{H}_2\text{O}$  also resulted in the formation of yellow thin needle of a non-hydrate compound  $\text{K}_{0.4}[\text{Cr}(\text{CN})_6][\text{Mn}(\text{S-pn})](\text{S-pnH})_{0.6}$ <sup>14f</sup> and the cubic crystal of Prussian blue analogue,  $\text{Mn}[\text{Cr}(\text{CN})_6]_{2/3}\cdot 5-6\text{H}_2\text{O}$ .<sup>28</sup> Our approach used for the synthesis of  $[\text{Mn}(\text{R-pnH})(\text{H}_2\text{O})][\text{Cr}(\text{CN})_6]\cdot\text{H}_2\text{O}$  did not give any of the yellow form.

### III-3.2. Thermogravimetric and differential thermal analyses

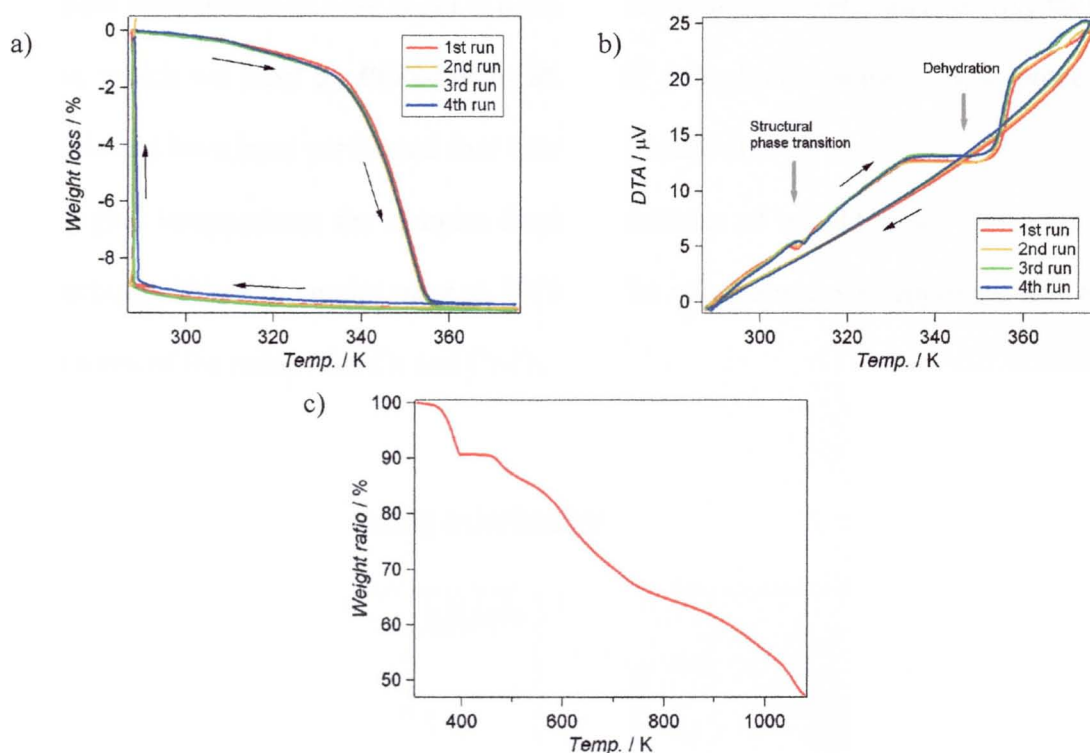


**Figure 3-1.** (a) Thermogravimetric and (b) DTA for **RGN-LTP** for several dehydration and rehydration cycles in the low temperature region (the black arrows point to the temperature cycle and the gray arrows to the transformations), and (c) TGA for the high temperature region.

The TG measurements of samples consisting of powdered crystals of virgin **RGN-LTP** under nitrogen atmosphere show a first weight loss around 350 K to a stable state up to 450 K where they decompose (Figure 3-1). The observed percentage weight loss (9.8%) is in good agreement with the departure of two water molecules per formula unit (9.63%). However, the DTA indicates two endothermic transformations, one at 310 K and the other around 350 K. The latter corresponds to the dehydration of the samples. The former is due to a structural phase transition. These two transformations are label as **RGN-LTP** (low temperature phase) to **RGN-HTP** (high temperature phase) and **RGN-HTP** to **RGN-DP** (dehydrated phase). On lowering the temperature of the samples having been heated only to 380 K under nitrogen the

weight gain is minimal. Interestingly, upon exposure of the samples to air (humidity  $\approx 50\%$ ) at ambient temperature ca. 290 K for  $\approx 8$  hours, they re-absorb water and recover their initial weights, which we label as **RGN-DP** to **RGN-HP** (rehydrated phase). These processes are reversible and have been performed four times consecutively.

At higher temperatures the samples display a cascade of weight losses starting at 450 K and reaching 47% of the molar mass at 1075 K. The value appears to approach that expected for the sums of the oxides,  $\text{MnO}_2$  and  $\text{Cr}_2\text{O}_3$ .

### III-3.3. Differential scanning calorimetry

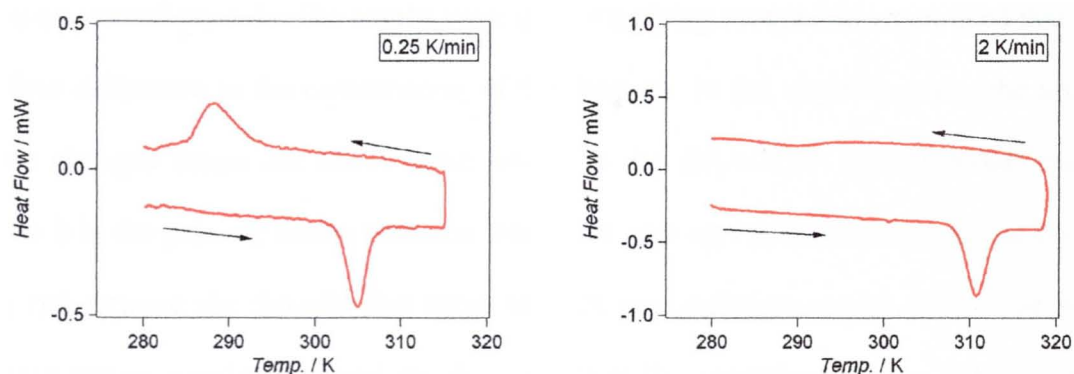


**Figure 3-2.** DSC curves showing the reversible transformation **RGN-LTP**  $\leftrightarrow$  **RGN-HTP** measured at two different scan speeds.

To quantify the phase transformation observed without a weight loss in the TGA, we performed differential calorimetry on powdered samples of **RGN-LTP** at two different scan-rates (Figure 3-2). At low scan-rate of 0.25 K/min the heat capacity on heating confirms the endothermic transformation at 305 K and on cooling it is recovered at a lower temperature of 290 K. This hysteresis suggests a first-order transition. Cycling the temperature at a higher scan-rate of 2 K/min. the transformation appears at a slightly elevated temperature of 311 K while there is no sign of a recovery down to 280 K. This suggests that it is possible to quench the high temperature phase, which is confirmed by crystallographic and magnetic

measurements (see later). The absorption was estimated to be 3.45 kJ/mol (0.825 kcal/mol) on warming and 3.59 kJ/mol (0.858 kcal/mol) on cooling. We therefore label another phase to identify the quenched state by quenched **RGN-HTP**.

### III-3.4. Crystal structures

The crystal structure of this compound at ambient conditions has been determined for several crystals from several batches and also on the same one at different times. Following the realization that there are several stable ground states as a function of temperature and that inter-conversions between them are reversible, we characterized the structures in its different states on several crystals. The results were quite satisfying except that we noticed that there is a subtle difference in the coordination of the diamine. In the virgin crystals, the secondary amine nitrogen forms the Mn-N bond while for the **RGN-HTP** and **RGN-DP** crystalline phases it is the primary amine nitrogen. Although, this was consistent for several crystals, it does not remove the thought that there may be two different crystal forms one with the primary amine coordinating and for the other it is the secondary amine. Subsequently, we undertook a careful re-examination of the crystal structures performed on one single crystal. This was not without problem. One is the cracking of the crystals on temperature cycling, second is the reproducibility of the different states as one change from the extreme limits. First, we encountered that the crystal thermal expansion is different to the araldite glue which causes breaking of the crystals which we finally resolved by applying glue to a cling film wrapping holding the crystal. Second we found that the stability of the crystals in a direct flow of nitrogen for intensity measurement of **RGN-HTP** at 309 K was not so good and so we protected the crystal by surrounding it with a clear drinking straw only at the first transformation from virgin **RGN-LTP**. The final protocol adopted for the reported structures, here, is given below pictorially. We have listed the structure determinations by numbers in red color and the transformation processes from one state to the other in blue. (Figure 3-3) The

transformation processes have been recorded in in-situ movie forms (see movie 3-1, -2, -3, -4, -5, -6). We describe below the structures in the three ground states, **RGN-LTP**, **RGN-HTP**, **RGN-DP** and its rehydrated form **RGN-HP** and discuss the changes at the different stages of the cycle.

### Protocol for X-ray measurements

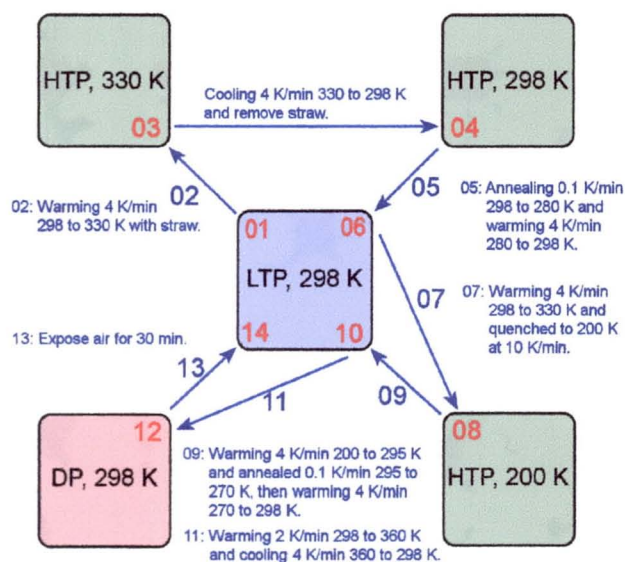


**Figure 3-3.** Protocol used for in-situ single crystal structure determinations.

Crystallographic Data for all phases achieved are given in table 3-1 and a list of the bond distances and angles is given in table 3-2. X-ray structural analyses of the all the data collections indicate there is a conservation of the space-group  $P 2_12_12_1$  in all its states as that found for the compound with the *S*-enantiomer of diaminopropane. The structure of the virgin crystal of the *R*-form at ambient condition is an exact mirror image of that reported for the *S*-form. As such we will only highlight some extra details that have not been reported and is important in following and understanding the rest of the manuscript.

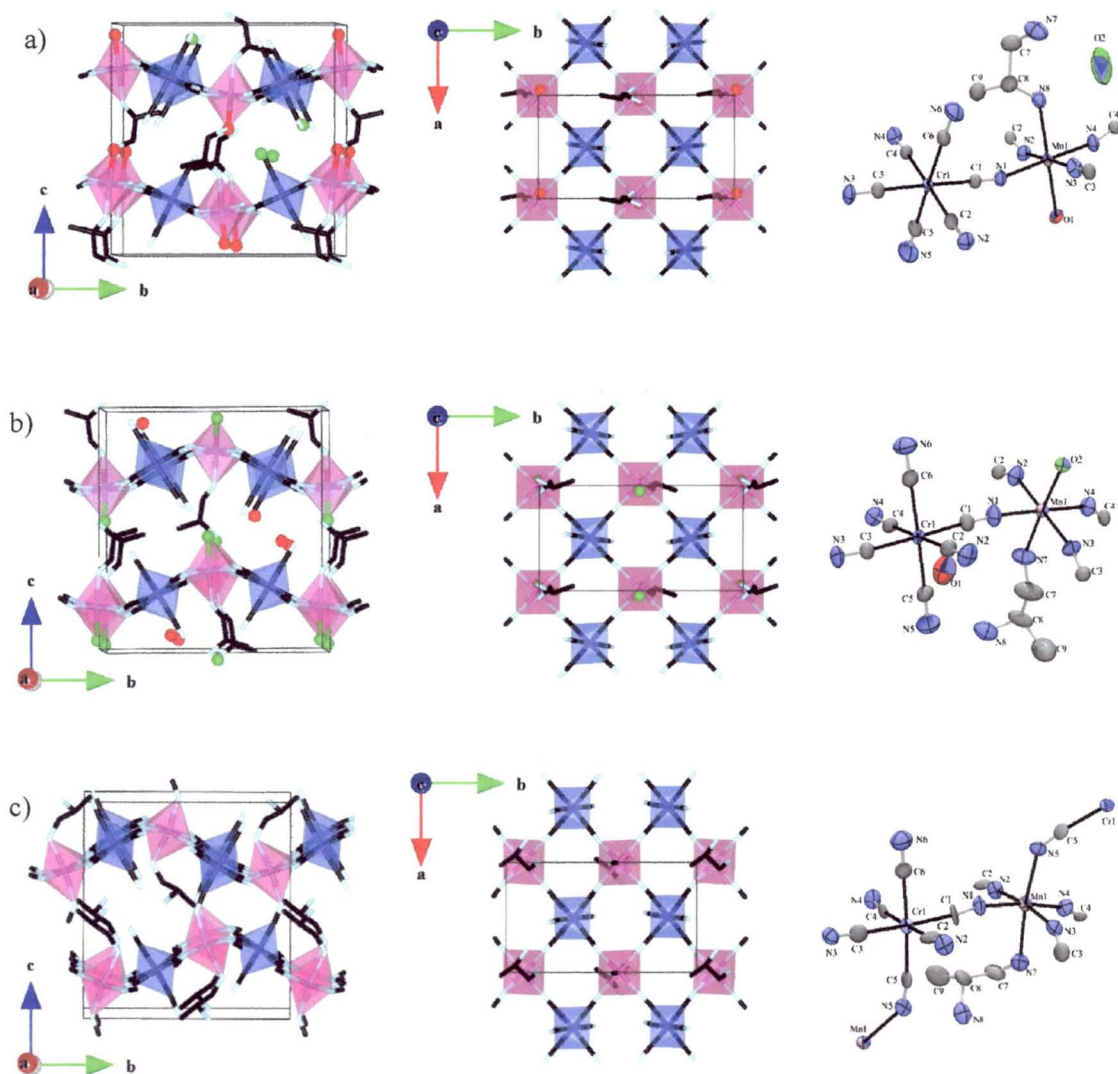


**Figure 3-4.** Projections of the structures along the  $a$ -axis (left), a view of the square grid layer of Mn (pink) and Cr (blue) atoms connected through cyanide (middle), and ORTEP drawing (right) for (a) **RGN-LTP**, (b) **RGN-HTP** and (c) **RGN-DP**. The two water molecules (red and green) are differentiated by the use of different colors.

**Table 3-1. Crystallographic data for virgin RGN-LTP, RGN-HTP at 330 and 298 K, relaxed RGN-LTP, quenched RGN-HTP, dehydrated RGN-DP and rehydrated RGN-HTP**

Compound	01 : Virgin RGN-LTP	03 : RGN-HTP <sup>a</sup>	04 : RGN-HTP <sup>b</sup>	06 : Relaxed RGN-LTP <sup>c</sup>	08 : Quenched RGN-HTP <sup>d</sup>	10 : Relaxed RGN-LTP <sup>e</sup>	12 : Dehydrated RGN-DP <sup>f</sup>	14 : Rehydrated RGN-HTP <sup>g</sup>
formula	C9H15CrMnN8O2	C9H15CrMnN8O2	C9H15CrMnN8O2	C9H15CrMnN8O2	C9H15CrMnN8O2	C9H15CrMnN8O2	C9H11CrMnN8	C9H15CrMnN8O2
fw	374.23	374.23	374.23	374.23	374.23	374.23	338.20	374.23
T, K	298 K	330 K	298 K	298 K	200 K	298 K	298 K	298 K
atmosphere	Air	Nitrogen	Air	Air	Nitrogen	Air	Nitrogen	Air
crystal System	Orthorhombic	Orthorhombic	Orthorhombic	Orthorhombic	Orthorhombic	Orthorhombic	Orthorhombic	Orthorhombic
space Group	<i>P</i> 2 <sub>1</sub> 2 <sub>1</sub> 2 <sub>1</sub>	<i>P</i> 2 <sub>1</sub> 2 <sub>1</sub> 2 <sub>1</sub>	<i>P</i> 2 <sub>1</sub> 2 <sub>1</sub> 2 <sub>1</sub>	<i>P</i> 2 <sub>1</sub> 2 <sub>1</sub> 2 <sub>1</sub>	<i>P</i> 2 <sub>1</sub> 2 <sub>1</sub> 2 <sub>1</sub>	<i>P</i> 2 <sub>1</sub> 2 <sub>1</sub> 2 <sub>1</sub>	<i>P</i> 2 <sub>1</sub> 2 <sub>1</sub> 2 <sub>1</sub>	<i>P</i> 2 <sub>1</sub> 2 <sub>1</sub> 2 <sub>1</sub>
<i>a</i> , Å	7.6420(6)	7.4503(16)	7.4439(7)	7.6421(10)	7.4250(6)	7.6459(7)	7.712(3)	7.6695(16)
<i>b</i> , Å	14.5365(12)	14.465(3)	14.4725(14)	14.5416(19)	14.5177(11)	14.5442(12)	13.401(5)	14.586(3)
<i>c</i> , Å	14.9570(12)	15.649(3)	15.6319(15)	14.958(2)	15.5242(12)	14.9647(13)	14.058(5)	15.013(3)
<i>V</i> , Å <sup>3</sup>	1661.5(2)	1686.4(6)	1684.1(3)	1662.2(4)	1673.4(2)	1664.1(3)	1452.8(9)	1679.5(6)
Z	4	4	4	4	4	4	4	4
<i>D</i> <sub>c</sub> , g/cm <sup>3</sup>	1.496	1.474	1.476	1.495	1.485	1.494	1.546	1.480
$\mu$ (Mo K $\alpha$ ), mm <sup>-1</sup>	1.429	1.408	1.410	1.428	1.419	1.426	1.615	1.413
crystal size, mm <sup>3</sup>	0.50 × 0.20 × 0.10	0.50 × 0.20 × 0.10	0.50 × 0.20 × 0.10	0.50 × 0.20 × 0.10	0.50 × 0.20 × 0.10	0.50 × 0.20 × 0.10	0.50 × 0.20 × 0.10	0.50 × 0.20 × 0.10
<i>T</i> <sub>min</sub> and <i>T</i> <sub>max</sub>	0.827, 1.000	0.823, 1.000	0.825, 1.000	0.794, 1.000	0.844, 1.000	0.806, 1.000	0.475, 1.000	0.633, 1.000
$\theta$ <sub>min</sub> and $\theta$ <sub>max</sub> , deg	2.722, 27.88	2.603, 27.26	2.606, 27.72	2.720, 27.88	2.624, 27.88	2.722, 27.71	<sup>b</sup> 3.040, 23.87	2.793, 26.53
no. of total reflections	5716	5794	5776	5688	5749	5686	3548	5256
no. of unique reflections ( <i>R</i> <sub>int</sub> )	3505	3583	3579	3517	3561	3530	2198	3433
no. of observed [ <i>I</i> ≥ 2 $\sigma$ ( <i>I</i> )]	2944	2814	2923	2949	3168	2967	1592	2357
no. of parameters	205	192	200	209	204	204	174	192
<i>R</i> / <i>wR</i> 2 [ <i>I</i> ≥ 2 $\sigma$ ( <i>I</i> )]	0.0309, 0.0725	0.0371, 0.0904	0.0364, 0.882	0.0322, 0.0743	0.0303, 0.0733	0.0311, 0.0727	0.0707, 0.1594	0.0897, 0.1937
<i>R</i> / <i>wR</i> 2 (all data)	0.0387, 0.0750	0.0505, 0.0942	0.0455, 0.913	0.0402, 0.0772	0.0352, 0.0749	0.0390, 0.0751	0.1096, 0.1817	0.1497, 0.2300
<i>G</i> OF	0.982	0.981	0.963	0.978	1.003	0.982	1.136	1.256
<i>F</i> lack	-0.01(3)	0.02(4)	-0.01(3)	-0.04(3)	-0.05(2)	-0.03(3)	0.14(12)	-0.08(11)
$\Delta\rho$ <sup>h</sup> , e/Å <sup>3</sup>	0.421, -0.363	0.487, -0.503	0.510, -0.562	0.416, -0.489	0.665, -0.381	0.450, -0.346	0.588, -0.621	-0.756, 1.097

<sup>a</sup>Data were collected after virgin RGN-LTP in straw was warmed at a rate of 4 K/min from 298 to 330 K under nitrogen. <sup>b</sup>Data were collected after RGN-HTP in straw was cooled at a rate of 4 K/min from 330 to 298 K under nitrogen, and straw was taken off. <sup>c</sup>Data were collected after RGN-HTP was treated at a cooling rate of 0.1 K/min from 295 to 280 K for annealing, then at a warming rate of 4 K/min from 280 to 298 K under nitrogen. <sup>d</sup>Data were collected after relaxed RGN-LTP was treated under nitrogen at a warming rate of 4 K/min from 298 to 330 K, then at a cooling rate of 10 K/min from 330 to 200 K for quenching. <sup>e</sup>Full scan was operated after quenched RGN-HTP in straw was treated under nitrogen at a warming rate of 4 K/min from 200 to 295 K, and annealed at a cooling rate of 0.1 K/min from 295 to 290 K, then warmed at a rate of 4 K/min from 290 to 298 K. <sup>f</sup>Data were collected after relaxed RGN-LTP was treated under nitrogen at a warming rate of 2 K/min from 298 to 360 K, then at a cooling rate of 4 K/min from 360 to 298 K. <sup>g</sup>Data were collected after RGN-DP was exposed air for 30 min.



**Table 3-2.** Selected bond distances, angles and metal separations for *RGN-LTP*, *RGN-HTP* and *RGN-DP*.

Selected bond distances (Å) for octahedral geometries for Mn and Cr

	<i>RGN-LTP</i> <sup>a</sup>	<i>RGN-HTP</i> <sup>b</sup>	<i>RGN-DP</i> <sup>c</sup>
Mn(1)-N(1)	2.208(3)	2.193(4)	2.245(14)
Mn(1)-N(2)	2.230(3)	2.212(4)	2.180(15)
Mn(1)-N(3)	2.205(3)	2.213(4)	2.201(16)
Mn(1)-N(4)	2.202(3)	2.234(4)	2.169(14)
Mn(1)-O/N <sup>e</sup>	2.235(2)	2.218(2)	2.259(9)
Mn(1)-N <sup>d</sup>	2.314(2)	2.283(3)	2.371(9)
Cr(1)-C(1)	2.067(3)	2.072(4)	2.114(15)
Cr(1)-C(2)	2.076(3)	2.082(5)	2.027(18)
Cr(1)-C(3)	2.075(3)	2.078(4)	2.043(18)
Cr(1)-C(4)	2.064(3)	2.075(4)	2.060(15)
Cr(1)-C(5)	2.054(3)	2.071(3)	2.080(10)
Cr(1)-C(6)	2.072(3)	2.059(3)	2.063(11)

<sup>a</sup>From the parameter of virgin *RGN-LTP*. <sup>b</sup>From the parameter of *RGN-HTP*. <sup>c</sup>From the parameter of *RGN-DP*.<sup>d</sup>N(8)/N(7)/N(7) for *RGN-LTP*/*HTP*/*DP*, respectively. <sup>e</sup>O(1)/O(2)/N(5) for *RGN-LTP*/*HTP*/*DP*, respectively.

Bond angles (°) for octahedral geometries for Mn and Cr

	<i>RGN-LTP</i> <sup>a</sup>	<i>RGN-HTP</i> <sup>b</sup>	<i>RGN-DP</i> <sup>c</sup>
N(1)-Mn(1)-N(2)	91.17(8)	90.68(11)	89.0(3)
N(1)-Mn(1)-N(3)	89.07(9)	91.20(12)	88.5(5)
N(1)-Mn(1)-N <sup>d</sup>	95.45(10)	89.53(13)	92.3(6)
N(1)-Mn(1)-O/N <sup>e</sup>	83.79(10)	91.24(12)	91.2(5)
N(2)-Mn(1)-N(4)	87.47(9)	89.11(12)	88.9(5)
N(2)-Mn(1)-N <sup>d</sup>	89.06(10)	85.47(14)	89.4(6)
N(2)-Mn(1)-O/N <sup>e</sup>	92.16(10)	97.61(13)	99.6(5)
N(3)-Mn(1)-N(4)	92.23(9)	88.98(11)	92.5(3)
N(3)-Mn(1)-N <sup>d</sup>	92.47(10)	93.25(14)	81.7(5)
N(3)-Mn(1)-O/N <sup>e</sup>	86.31(10)	83.64(12)	89.5(5)
N(4)-Mn(1)-N <sup>d</sup>	86.50(10)	88.88(13)	80.9(6)
N(4)-Mn(1)-O/N <sup>e</sup>	94.29(10)	90.36(11)	95.8(6)
N(1)-Mn(1)-N(4)	177.61(14)	178.40(14)	172.9(6)
N(2)-Mn(1)-N(3)	178.42(11)	177.72(13)	170.6(6)
N-Mn(1)-O/N <sup>e</sup>	178.57(8)	176.81(11)	170.4(4)
C(1)-Cr(1)-C(2)	89.21(10)	87.81(13)	91.8(4)
C(1)-Cr(1)-C(4)	90.45(17)	93.09(18)	90.2(6)

C(1)-Cr(1)-C(5)	89.93(14)	90.30(17)	92.8(7)
C(1)-Cr(1)-C(6)	87.33(14)	90.25(17)	90.5(6)
C(2)-Cr(1)-C(3)	90.66(16)	91.8(2)	87.1(7)
C(2)-Cr(1)-C(5)	90.86(14)	90.54(17)	95.5(6)
C(2)-Cr(1)-C(6)	89.74(14)	90.87(15)	85.6(6)
C(3)-Cr(1)-C(4)	89.63(10)	87.22(13)	90.6(4)
C(3)-Cr(1)-C(5)	88.56(15)	90.97(16)	91.0(7)
C(3)-Cr(1)-C(6)	94.18(15)	88.49(17)	85.8(7)
C(4)-Cr(1)-C(5)	87.37(15)	90.77(17)	88.6(7)
C(4)-Cr(1)-C(6)	92.01(14)	87.82(15)	90.2(6)
C(1)-Cr(1)-C(3)	178.49(16)	178.69(19)	176.1(8)
C(2)-Cr(1)-C(4)	178.20(16)	178.4(2)	175.3(7)
C(5)-Cr(1)-C(6)	177.18(19)	178.51(14)	176.5(4)

<sup>4</sup>N(8)/N(7)/N(7) for *RGN-LTP/-HTP/-DP*, respectively. <sup>4</sup>O(1)/O(2)/N(5) for *RGN-LTP/-HTP/-DP*, respectively.

#### Selected bond angles (°) for two-dimensional sheet

	<i>RGN-LTP</i> <sup>a</sup>	<i>RGN-HTP</i> <sup>b</sup>	<i>RGN-DP</i> <sup>c</sup>
C(1)-N(1)-Mn(1)	165.0(3)	171.9(4)	163.9(16)
C(2) <sup>#1</sup> -N(2)-Mn(1)	152.0(3)	153.3(4)	173.0(15)
C(3) <sup>#2</sup> -N(3)-Mn(1)	177.8(3)	166.6(4)	151.3(16)
C(4) <sup>#3</sup> -N(4)-Mn(1)	162.3(4)	150.8(4)	161.6(16)
C(5) <sup>#4</sup> -N(5)-Mn(1)			140.5(7)
N(1)-C(1)-Cr(1)	177.8(4)	176.2(4)	173.1(17)
N(2) <sup>#5</sup> -C(2)-Cr(1)	176.2(3)	176.9(4)	179.1(18)
N(3) <sup>#6</sup> -C(3)-Cr(1)	177.0(4)	176.2(4)	176.8(19)
N(4) <sup>#7</sup> -C(4)-Cr(1)	177.6(4)	173.9(4)	170.8(16)
N(5) <sup>#8</sup> -C(5)-Cr(1)			173.2(8)

Symmetry codes: #1  $x-1, y, z$ ; #2  $-x, y-1/2, -z+1/2$ ; #3  $-x-1, y-1/2, -z+1/2$ ; #4  $-x-1/2, -y+1, z+1/2$ ; #5  $x+1, y, z$ ; #6  $-x, y+1/2, -z+1/2$ ; #7  $-x-1, y+1/2, -z+1/2$ ; #8  $-x-1/2, -y+1, z-1/2$ .

#### Distances for hydrogen bonds (Å)

	<i>RGN-LTP</i> <sup>a</sup>		<i>RGN-HTP</i> <sup>b</sup>
N(7)⋯O(1) <sup>#1</sup>	2.954(4)	N(8)⋯O(2)	2.958(4)
N(7)⋯O(2)	2.835(6)	N(8)⋯O(1)	2.862(6)
O(1)⋯N(5) <sup>#2</sup>	2.742(4)	O(2)⋯N(5) <sup>#4</sup>	2.724(4)
O(1)⋯N(6) <sup>#3</sup>	2.763(3)	O(2)⋯N(6) <sup>#5</sup>	2.752(4)

Symmetry codes: #1  $-x+1/2, -y+1, z+1/2$ ; #2  $x-1/2, -y+1/2, -z$ ; #3  $-x+1/2, -y+1, z-1/2$ ; #4  $x-1/2, -y+1/2, -z+1$ ; #5  $-x+1/2, -y+1, z+1/2$ .

Intra-network metal separations (Å) through one cyanide group.

	RGN-LTP <sup>a</sup>	RGN-HTP <sup>b</sup>	RGN-DP <sup>c</sup>
Mn(1)⋯Cr(1) <sup>f</sup>	5.3642(8)	5.3911(9)	5.448(4)
Mn(1)⋯Cr(1) <sup>#1, g</sup>	5.2670(8)	5.2821(9)	5.386(4)
Mn(1)⋯Cr(1) <sup>#2, h</sup>	5.4147(8)	5.3778(9)	5.189(4)
Mn(1)⋯Cr(1) <sup>#3, i</sup>	5.3368(8)	5.2486(9)	5.247(4)
Mn(1)⋯Cr(1) <sup>#4, j</sup>			5.092(3)
Mn(1)⋯Cr(1) (Ave.)	5.3457(16)	5.3249(18)	5.272(8)

Metal separation through <sup>f</sup>C(1)-N(1), <sup>g</sup>C(2)-N(2), <sup>h</sup>C(3)-N(3), <sup>i</sup>C(4)-N(4), <sup>j</sup>C(5)-N(5). Symmetry codes: #1 x-1, y, z; #2 -x+1, y+1/2, -z+1/2; #3 -x, y+1/2, -z+1/2; #4 -x+1/2, -y+1, z+1/2.

Selected intra-network metal separations (Å) through two cyanide groups.

	RGN-LTP <sup>a</sup>	RGN-HTP <sup>b</sup>	RGN-DP <sup>c</sup>
Mn(1)⋯Mn(1) <sup>#1, k</sup>	7.6420(8)	7.4439(9)	7.712(5)
Mn(1)⋯Mn(1) <sup>#2, k</sup>	7.6420(8)	7.4439(9)	7.712(5)
Mn(1)⋯Mn(1) <sup>#3, l</sup>	7.4708(7)	7.6026(9)	7.194(3)
Mn(1)⋯Mn(1) <sup>#4, l</sup>	7.4708(7)	7.6026(9)	7.194(3)
Cr(1)⋯Cr(1) <sup>#1, k</sup>	7.6420(13)	7.444(2)	7.712(5)
Cr(1)⋯Cr(1) <sup>#2, k</sup>	7.6420(13)	7.444(2)	7.712(5)
Cr(1)⋯Cr(1) <sup>#5, l</sup>	7.2753(7)	7.2507(8)	6.839(3)
Cr(1)⋯Cr(1) <sup>#6, l</sup>	7.2753(7)	7.2507(8)	6.839(3)

Metal separation along to <sup>k</sup>// a-axis and <sup>l</sup>// b-axis. Symmetry codes: #1 x+1, y, z; #2 x-1, y, z; #3 -x, y+1/2, -z+1/2; #4 -x, y-1/2, -z+1/2; #5 -x+1, y+1/2, -z+1/2; #6 -x+1, y-1/2, -z+1/2.

Selected inter-network metal separations (Å).

	RGN-LTP <sup>a</sup>	RGN-HTP <sup>b</sup>
Mn(1)⋯Cr(1) <sup>#1</sup>	7.3217(6)	7.6883(9)
Mn(1)⋯Cr(1) <sup>#2 / #3</sup>	7.7780(7)	7.4696(8)
Mn(1)⋯Mn(1) <sup>#4</sup>	8.3453(7)	8.5886(10)
Mn(1)⋯Mn(1) <sup>#5</sup>	8.3453(7)	8.5886(10)
Mn(1)⋯Mn(1) <sup>#1</sup>	8.4566(7)	8.7350(10)
Mn(1)⋯Mn(1) <sup>#2</sup>	8.4566(7)	8.7350(10)
Cr(1)⋯Cr(1) <sup>#6</sup>	8.1168(9)	8.2477(11)
Cr(1)⋯Cr(1) <sup>#3</sup>	8.1168(9)	8.2477(11)
Cr(1)⋯Cr(1) <sup>#7</sup>	8.6856(9)	9.0727(11)
Cr(1)⋯Cr(1) <sup>#8</sup>	8.6856(9)	9.0727(11)

Symmetry codes: #1 -x+1/2, -y+1, z+1/2; #2 -x+1/2, -y+1, z-1/2; #3 x-1/2, -y+1/2, -z; #4 -x-1/2, -y+1, z+1/2; #5 -x-1/2, -y+1, z-1/2; #6 x+1/2, -y+1/2, -z; #7 x+1/2, -y+1/2, -z+1; #8 x-1/2, -y+1/2, -z+1.

### III-3.4.1. Structures of virgin *RGN-LTP* (1), relaxed *RGN-LTP* (6), relaxed *RGN-LTP* (10), and rehydrated *RGN-HP* (14) at 298 K

The low temperature phase has been observed on several crystals and at several stages through the protocol used of this study on one single crystal and their structure determinations confirm the reversibility at all stages. We have performed all the structures at 298 K to be consistent and for easy comparison. It is clear from the reliability factors that direct comparisons of the geometries can be carried out with complete confidence. The key feature of the structure of the *RGN-LTP* is the 2D-square grid of Mn and Cr(CN)<sub>4</sub> where the Mn and Cr alternate in the *ab*-plane and bridged by cyanide (Figure 3-4a). However, the layers are not planar but are corrugated and propagated along the *b*-axis and are in-phase with its neighboring layers. Viewing along the *c*-axis, that is perpendicular to the layers, we find that adjacent layers are staggered. The remaining two cyanide groups complete the octahedral coordination of the Cr atom and pointing out of the layers while the amine and one water molecule are coordinated trans- to each other to the Mn atom. Both metals show slight distortion coordination from perfect octahedral geometry where Mn(1)-N/O distances range from 2.202(3) to 2.314(2) Å and N-Mn-N/O angles are in the range 83.79(10) - 95.45(10)° and 177.61(14) - 178.57(8)° for *cis* and *trans* positions. While Cr(1)-C distances range from 2.054(3) to 2.076(3) Å and C-Cr-C angles are in the range of 87.33(14) - 94.18(15)° and 177.18(19) - 178.49(16)° for *cis* and *trans* positions. Another water molecule is situated in the galleries between the layers. To balance the charges a proton is needed and based on chemical grounds, it was thought to be on the non-coordinated nitrogen of the amine in the previous report of the compound with the *S*-enantiomer. We find that this proton, involved in strong hydrogen bonding between the diamine, the coordinated and the non-coordinated water molecules, is coupled to the transition from *RGN-LTP* and *RGN-HTP*. Important to note with respect to the structure of *RGN-HTP* is that the amine is coordinated to the Mn atom via the nitrogen  $\alpha$ -carbon.

### III-3.4.2. Structures of *RGN-HTP* at 330 K (3), *RGN-HTP* at 298 K (4), and quenched *RGN-HTP* at 200 K (8)

The structure of the *RGN-HTP* phase has been determined at different temperatures to verify the reversibility as well as to confirm the thermodynamic order of the phase transition. We find that the latter is of first-order and it was, therefore, possible to quench the crystal in the high temperature phase by fast cooling and this allowed us to study the low temperature magnetic properties (see later).

The main feature of the structure of the *RGN-HTP* remains the same as the *RGN-LTP* for all three determinations, while the most striking difference is an increase of the *c*-axis (14.9 to 15.6 Å; 4.6%) from *RGN-LTP* to *RGN-HTP* (Figure 3-4b). The structural phase transition from *RGN-LTP* to *RGN-HTP* was then easily identified by collecting a 2D frame on the CCD as a function of temperature (see movie 2). The coordination of the metals exhibits less distortion from an octahedron compared to the *RGN-LTP* where Mn(1)-N/O distances range from 2.193(4) to 2.283(3) Å and N-Mn-N/O angles are in the range of 85.47(14) - 97.61(13)° and 176.81(11) - 178.40(14)° for *cis* and *trans* positions. While Cr(1)-C distances range from 2.059(3) to 2.082(5) Å and C-Cr-C angles are in the range of 87.22(13) - 93.09(18)° and 178.4(2) - 178.69(19)° for *cis* and *trans* positions. Within the 2-D sheets, the average Mn-Cr separations for *RGN-HTP* 5.3249(18) Å is slightly shorter than that for *RGN-LTP* (5.3457(16) Å), and the shortest intersheet metal separations are observed between the Mn and Cr atoms (7.3217(6) and 7.4696(8) Å for *RGN-LTP* and *RGN-HTP*, respectively), while the shortest intersheet homometallic contacts are greater than 8 Å (8.1168(9) and 8.2477(11) Å for *RGN-LTP* and *RGN-HTP*, respectively). To our surprise, the largest change was the way the amine is coordinated to the Mn atom. In contrast to the *RGN-LTP* where the nitrogen on the  $\alpha$ -carbon makes a bond with the Mn, for *RGN-HTP* it is the one on the  $\beta$ -carbon. This difference, which was observed when the crystal structures of the two phases were performed on different crystals, is reproducible when both were performed on the same crystal. There are

two ways this can take place and they are discussed in the next section. It involves the hydrogen bonding between the layers. Between the 2-D sheets, the non-coordinating nitrogen atom (N(7) of the amine for LTP and N(8) for HTP) forms two hydrogen bonds with the oxygen atom of the coordinating water (N $\cdots$ O(1') / O(2), 2.954(4) and 2.958(4) Å for **RGN-LTP** and **RGN-HTP**, respectively) and crystal water (N $\cdots$ O(2) / O(1), 2.835(6) and 2.862(6) Å for **RGN-LTP** and **RGN-HTP**, respectively). The oxygen atom (O(1) for LTP and O(2) for HTP) of coordinating water forms two more hydrogen bonds between nitrogen atoms of cyanide group in neighboring layer; (O $\cdots$ N(5'), 2.742(4) and 2.763(3) Å; O $\cdots$ N(6'), 2.724(4) and 2.752(4) Å for **RGN-LTP** and **RGN-HTP**, respectively).

### III-3.4.3. Structure of DP (12) at 298 K

Preparation of the crystal structure for the determination of the dehydrated phase (**RGN-DP**) was performed by heating the single crystal at a rate of 2 K/min up to 360 K and cooled down to 298 K for structural measurement. This procedure was done in a nitrogen stream. Recording of the diffraction pattern as a function of temperature shows the consecutive transitions from **RGN-LTP** to **RGN-HTP** and then from **RGN-HTP** to **RGN-DP**. While the Bragg spots are of the same size and shape on going from **RGN-LTP** to **RGN-HTP**, they are severely elongated for **RGN-DP** and on returning to **RGN-HTP** upon rehydration. However, after data reduction and analysis we were able to refine the structure for **RGN-DP** to acceptable reliabilities.

The X-ray structural analysis of **RGN-DP** reveals the same  $P2_12_12_1$  space group but instead it displays three-dimensional connectivity between Mn and Cr via the previously non-bridging cyanides (Figure 3-4c). Both the coordinating and non-coordinating water molecules are absent from the structure, while the free cyanide takes the place of the departed water. This causes severe movements of the layers and eventually the layers stack in eclipse form when viewed along the  $c$ -axis. The amine is as that observed in the **RGN-HTP** structure.

Mn ion exhibits distorted octahedral geometry (Mn-N distance are in the range from 2.169(14) to 2.371(9) Å and N-Mn-N angles are in the range of 80.9(6) - 99.6(5)° and 170.4(4) - 172.9(6)° for *cis* and *trans* position) comprising nitrogen atoms of five [Cr(CN)<sub>6</sub>]<sup>3-</sup> ions and pnH molecule. Mn(1) has four bridging cyanide nitrogen atoms (N(1), N(2), N(3) and N(4)) in equatorial positions, nitrogen atom N(7) from pn and nitrogen atom N(5) of bridging cyanide to complete its octahedral geometry. Replacement of the oxygen atom O(1) (**RGN-LTP** and **RGN-HTP**) to the N(5) of layer bridging cyanide (**RGN-DP**), brings the crystal structure to the higher dimension (2-D to 3-D). The geometries of the Cr and Mn octahedral suggest more distortion than those observed for **RGN-LTP** and **RGN-HTP**. More distortions are also evidenced within the cyanide network, where the observed minimum Mn-N-C and Cr-C-N angles in **RGN-DP** are 140.5(7) and 170.8(16)°, respectively, compared to 152.0(3) and 176.2(3)° for **RGN-LTP** and 150.8(4) and 173.9(4)° for **RGN-HTP**. Heterometal (Cr...Mn) separations for **RGN-DP** are considerably shorter (5.092(3), 5.189(4) Å) than those for **RGN-LTP** (5.2670(8) - 5.4147(8) Å) and **RGN-HTP** (5.2486(9) - 5.3911(9) Å). Homometal separations (Mn...Mn and Cr...Cr) linked by two cyanide groups along the *ab*-plane in **RGN-DP** are different from the other phases. In both **RGN-LTP** and **RGN-HTP**, these separations range from 7.2507(8) to 7.6420(13) Å describing that the bimetallic square from Mn(1), Cr(1), Mn(1') and Cr(1') ions is slightly distorted from the ideal square. On the contrary, homometal separations in **RGN-DP** along the *b*-axis are 7.194(3) and 6.839(3) Å, while those along the *a*-axis are 7.712(5) Å (x2). The difference indicates that the bimetallic square is compressed along the *b*-axis during dehydration.

Comparison with **RGN-HTP**, **RGN-DP** has same space-group, but has different structural motifs. The length of the *c*-axis and the cell volume for **RGN-DP** (14.058(5) Å, 1452.8(9) Å<sup>3</sup>) are smaller than that for **RGN-HTP** (15.6319(15) Å, 1684.1(3) Å<sup>3</sup>). The unit cell volume is decreased 231.3 Å<sup>3</sup> by dehydration.

### III-3.5. Powder X-ray diffraction

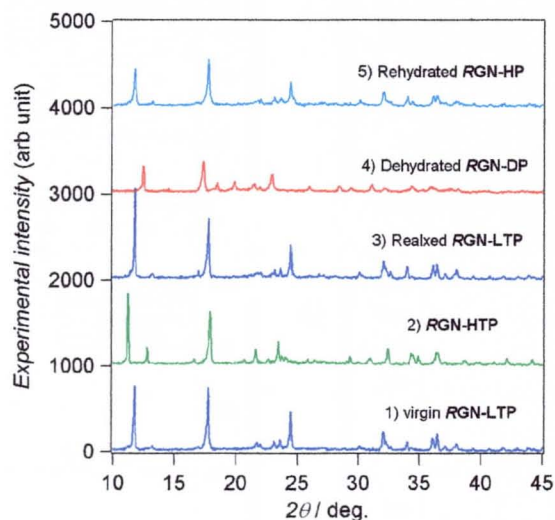


**Figure 3-5.** Experimental XRPD (Cu K $\alpha$ ) patterns for virgin **RGN-LTP**, **RGN-HTP**, relaxed **RGN-LTP**, **RGN-DP**, and **RGN-HP** from bottom to top.

Powder X-ray diffraction for all phases were collected by in-situ measurements. The results are shown in figure 3-5 and 3-6, including the calculated diffraction patterns using the single-crystal data. It is clear that the pattern for virgin **RGN-LTP**, relaxed **RGN-LTP** and **RGN-HP** are as expected from the single crystal experiments, indicating the two structural changes are bulk properties. However, the loss of intensity was observed after dehydration.

To investigate the hydration process, the same sample was placed on a glass plate, heated to 360 K for 30 min and exposed to the air, again. During the hydration, narrow  $2\theta$  range was collected repeatedly. As can be seen in figure 3-7, when the dehydrated sample was exposed to air, 002 peak of **RGN-DP** ( $2\theta = 12.4^\circ$ ) and that of **RGN-LTP** ( $2\theta = 11.7^\circ$ ) start decreasing and growing, respectively, and no peak observed from **RGN-HTP**. It should be noted that this experiment was performed at 302 K where **RGN-HTP** is stable. If the hydration processes are from **RGN-DP** through **RGN-HTP** to **RGN-LTP**, this experimental condition would trap **HTP** and show peaks of this phase. Therefore it is clear that hydration process change **RGN-DP** to **RGN-LTP** directly.



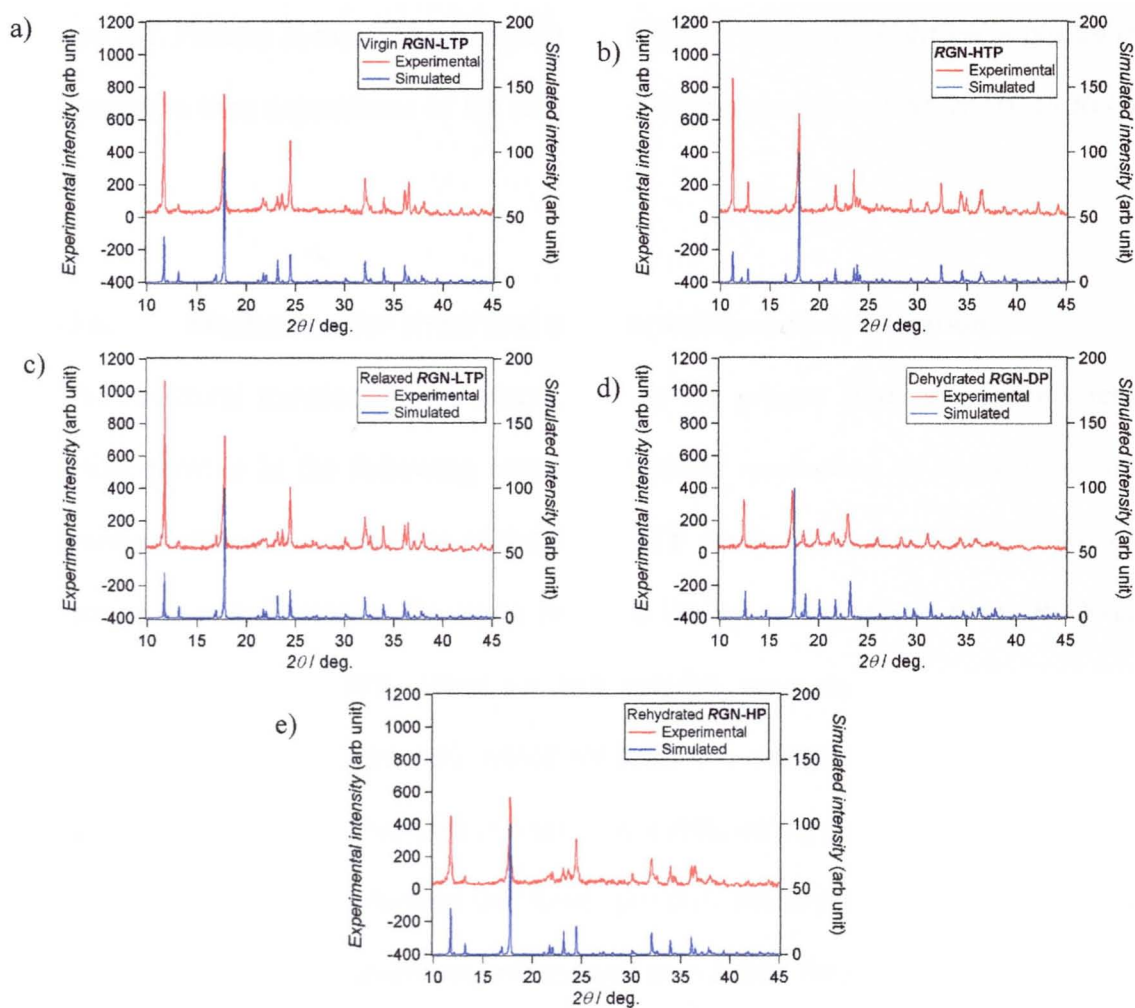


**Figure 3-6.** Experimental and simulated XRPD (Cu K $\alpha$ ) patterns for (a) **RGN-LTP**, (b) **RGN-HTP**, (c) relaxed **RGN-LTP**, (d) **RGN-DP**, and (e) **RGN-HP**.

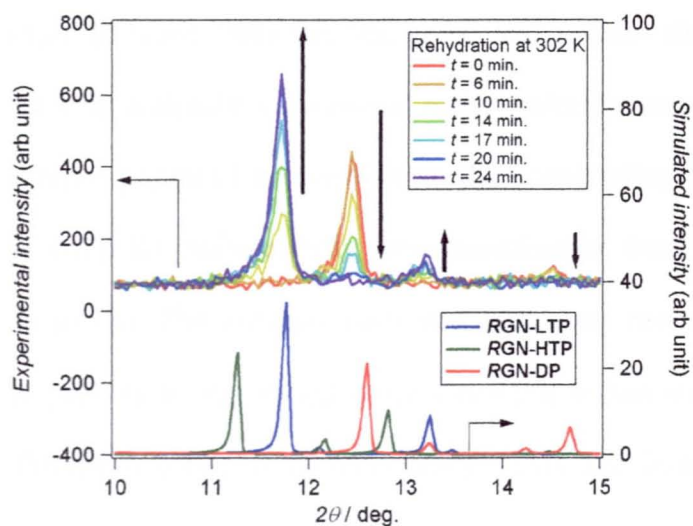


**Figure 3-7.** Powder X-ray diffraction patterns (Cu-K $\alpha$ ) for the three different phases (bottom) and exposure time dependence of the rehydration transformation of **RGN-DP** to **RGN-HP** in air.

### III-3.6. Mechanism for structural transformation and dehydration

The structural transformations encountered in the present study are unprecedented. We therefore provide in the following section a possible mechanism to explain the one major difference between the structures of the **RGN-LTP** compared to **RGN-HTP**, that is the way the amine is coordinated to the layer, being to the secondary nitrogen for **RGN-LTP** and primary one for **RGN-HTP**. There are two possible ways this can occur. One is through rotation of the amine (Figure 3-8), which we believe is energetically unfavorable and for the other one has to consider that there is a series of events taking place. The other way is through proton transfer. In this mechanism the ‘loose’ proton is the key and its hydrogen bonding with the water molecules is of major importance and also define the energy barrier. This transition is experimentally found to be of first order and therefore all the events happen in one concerted fashion. As can be seen in figure 3-9, first the proton is believed to be on the non-coordinated nitrogen atom N(7) of the amine. It hops to the water molecule O(1) coordinated to the Mn on one layer and the H<sub>3</sub>O<sup>+</sup> formed becomes loose (step I). This proton makes water molecule to leave from the Mn atom, and reaches the nitrogen N(8') on a  $\alpha$ -carbon of adjacent *R*-pn molecule, via a crystal water molecule, meanwhile the N-Mn bond dissociates and the other proton of pn transfers to the coordinating water molecule due to electronic repulsion (step II). Subsequently, new coordination bonds are formed between Mn-N and Mn-O (step III). The nitrogen atom was previously non-coordinating amine on  $\beta$ -carbon, and the oxygen atom was crystal water. Once this proton moving is accomplished, this reaction goes through one side to the other along *a*-axis like domino, accompanies with spot shape metamorphosis in the movie (steps IV, V, VI). However, since in both structures

the amine is coordinated to the peaks of the corrugated sheets and the water molecules are in the troughs, we propose that the layer corrugation must change by one pitch in the transition. Although the two structures are almost identical, there must be a subtle energy difference between the two so that the compound can reversibly settle in one or the other depending on the temperature. (Figure 3-10)

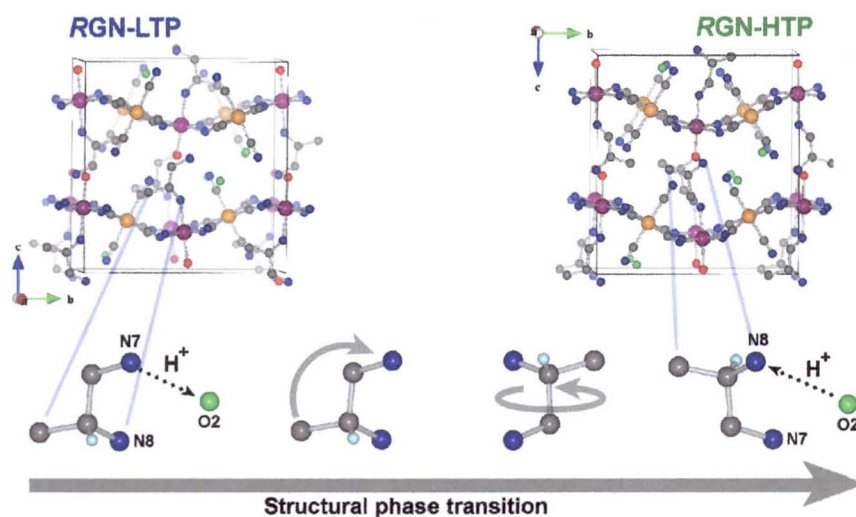


**Figure 3-8.** One of the possible mechanisms for structural transition at 310 K. pn molecules rotate through the structural change.

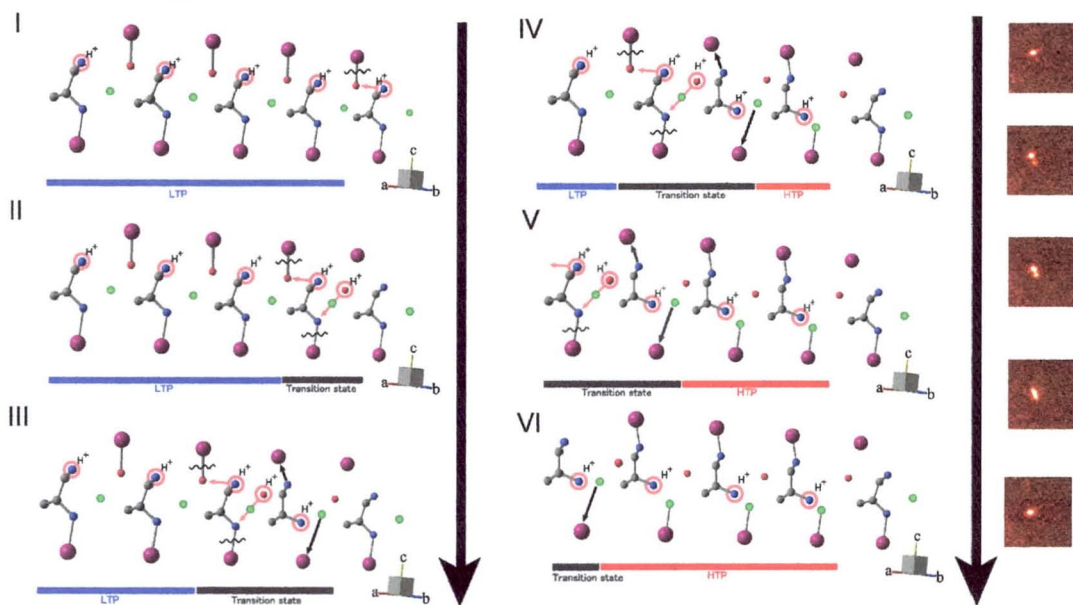


**Figure 3-9.** The proton-transfer mechanism for the structural transition at 310 K and the evolution of one Bragg reflection through the transition showing the existence of both phases.

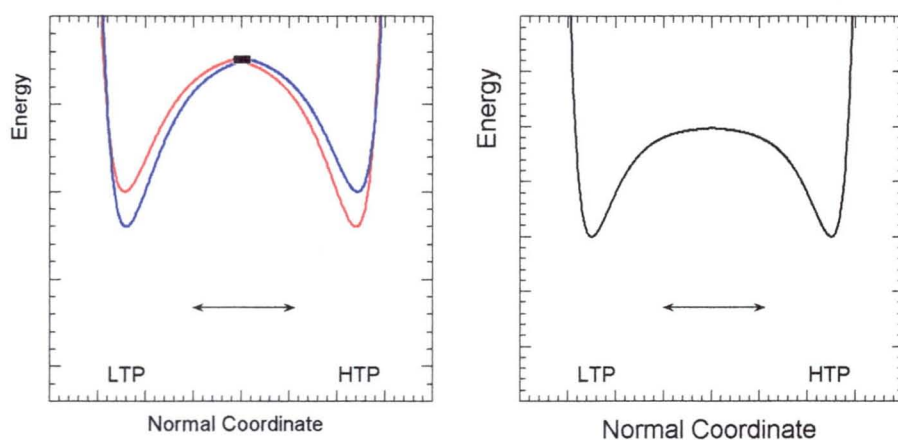


**Figure 3-10.** Potential energy curves for the reversible transformation of **RGN-LTP** to **RGN-HTP**.

In the process of dehydration, all the water molecules leave from the crystal and non-coordinating cyanide groups in adjacent layer coordinate to vacant Mn site (Figure 3-11). The dehydrated form retains the connections to the amine as in the **RGN-HTP** structure but when it is rehydrated at room temperature, it appears to return to the **RGN-LTP** without the

passage through the **RGN-HTP** in agreement to the stability of the two phases above and below the transition temperatures of 310 K.

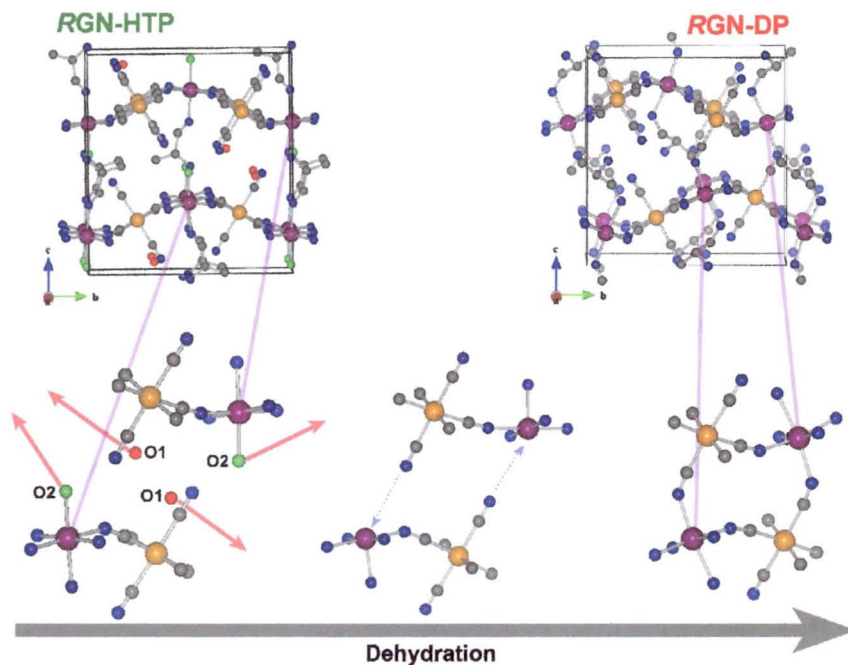


**Figure 3-11.** Evolution of the structure during the dehydration and the associated bond breaking and bond forming steps.

### III-3.7. Infrared spectroscopy

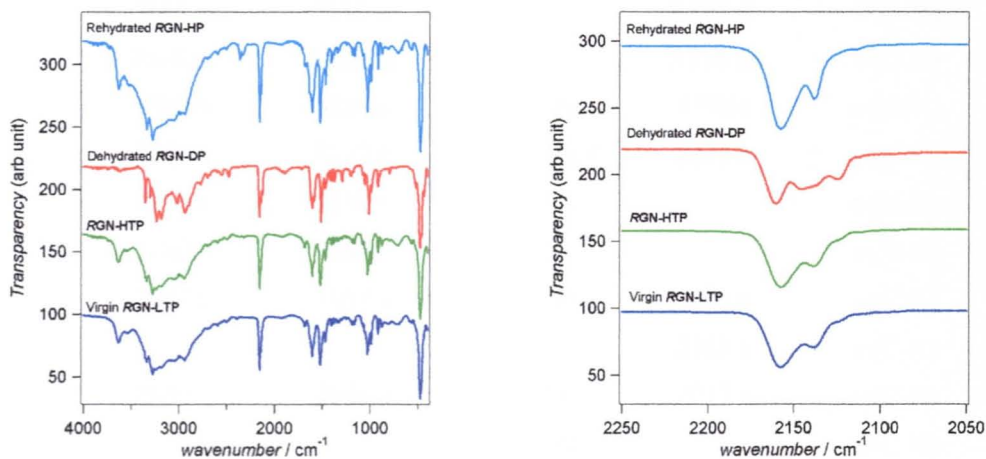


**Figure 3-12.** Transmission infrared spectra of the three phases.

The infrared spectra of the three phases are shown in figure 3-12. The bands can be assigned using group frequencies as follows (Table 3-3). The asymmetric and symmetric stretching modes of the water molecules are observed at the highest energy peaks at 3635 and 3541  $\text{cm}^{-1}$ , respectively. Its bending mode is observed at 1680  $\text{cm}^{-1}$ . All three bands are absent from the spectrum of the **RGN-DP** confirming the dehydration of **RGN-LTP** and **RGN-HTP**. The corresponding NH stretching modes and those of CH are observed at lower energies. We note that some sharpening of these bands are observed in the spectrum of **RGN-DP** compared to **RGN-LTP**, **RGN-HTP**, and **RGN-HP** and which may be associated with the presence of hydrogen bonds in the latter two. Only two sharp stretching modes of the cyanide are observed in the spectra of **RGN-LTP**, **RGN-HTP**, and **RGN-HP** and their energies are the same for the three. However, for **RGN-DP** there are two extra peaks of less intensity which may be due to the difference between those within and between layers. A very strong peak at 474  $\text{cm}^{-1}$  is seen in all spectra which may be due to Cr-C mode.

**Table 3-3.** Frequencies and assignments of the bands in the spectra of **RGN-LTP**, **RGN-HTP**, **RGN-DP**, and **RGN-HP**.

<b>RGN-LTP</b>	<b>RGN-HTP</b>	<b>RGN-DP</b>	<b>RGN-HP</b>	
3635 m	3631 m		3629 m	$\nu(\text{O-H})$
3541 m	3546 m		3534 m	$\nu(\text{O-H})$
3338 s	3338 s	3352 m	3336 s	$\nu(\text{N-H})$
3273 s	3237 s	3300 m	3273 s	$\nu(\text{N-H})$
3236 s	3236 s	3232 s		$\nu(\text{N-H})$
3180 s	3182 s	3182 s		$\nu(\text{N-H})$
3047 s	3047 s	3018 m	3056 s	$\nu(\text{C-H})$
			2983 s	$\nu(\text{C-H})$
2939 s	2941 s	2937 s	2937 s	$\nu(\text{C-H})$
		2771 m		$\nu(\text{C-H})$
2702 w	2701 w	2700 w	2703 w	
2677 w	2675 w	2675 w	2675 w	
2596 w	2596 w	2600 w	2595 w	

		2558 w		
2503 w	2501 w	2478 w	2503 vw	
2158 s	2158 s	2160 s	2158 s	$\nu(\text{C}\equiv\text{N})$
		2146 m		$\nu(\text{C}\equiv\text{N})$
2139 m	2139 m	2138 sh	2139 m	$\nu(\text{C}\equiv\text{N})$
		2125 m		$\nu(\text{C}\equiv\text{N})$
1932 vw, br	1921 vw, br	1923 w, br	1925 vw, br	
1680 w	1680 w		1676 m	$\delta(\text{O-H})$
		1618 m	1628 m	$\delta(\text{N-H})$
1603 s	1602 s	1603 s	1602 s	$\delta(\text{N-H})$
		1581 m		$\delta(\text{N-H})$
1518 s	1518 s	1510 s	1520 s	$\delta(\text{C-H})$
1462 m	1462 m	1470 m	1462 m	$\delta(\text{C-H})$
1400 w	1400 w	1416 w	1403 w	$\delta(\text{C-H})$
1373 w	1373 w	1394 w	1375 w	$\delta(\text{C-H})$
1336 w	1338 w	1369 w	1338 w	
1321 w	1323 w	1290 w	1321 w	
1186 w	1186 w	1196 w	1186 w	$\nu(\text{C-N})$
1163 w	1161 w	1174 w	1161 e	$\nu(\text{C-N})$
1078 w	1078 w	1078 w	1078 w	$\nu(\text{C-N})$
1055 w	1055 vw	1055 w	1053 w	$\nu(\text{C-N})$
1024 m	1024 s	1009 s	1024 w	$\nu(\text{C-N})$
985 m	985 m	985 m	985 m	$\nu(\text{C-N})$
914 m	914 m	914 m	914 m	$\delta(\text{N-H})$
874 w	873 w	899 w	876 w	$\delta(\text{N-H})$
806 w, br		794 w	810 w,br	$\delta(\text{N-H})$
714 w, br	706 w, br		708 w, br	
588 w			590 vw	
567 w	557 w	523 m	567 vw	
474 vs	474 vs	476 vs	474 vs	$\nu(\text{C}-\text{C})$
		436 m		

### III-3.8. UV-Vis spectroscopy

The transmission UV-vis spectrum of a single crystal is shown in figure 3-13. In contrast to the colors of the individual components which is yellow for  $\text{Cr}(\text{CN})_6$  and colorless for  $\text{MnON}_5$ , that of **RGN-LTP** is green. However, the color is not so intense. The transmission spectrum shows three bands in the visible region. The green color is due to the window at 19 kK. The three bands are all additional to those of the individual components, thus are intervalence bands ( $\text{Mn} \rightarrow \text{Cr}$  or  $\text{Cr} \rightarrow \text{Mn}$ ) and their presence can be explained by a simple molecular-orbital scheme and considering that the crystal field splitting is much larger for the  $\text{Cr}(\text{CN})_6$  center. The weak intensities of the bands suggest that they may be spin-forbidden. The most likely spin forbidden will be the  $\text{Cr} \rightarrow \text{Mn}$  intervalence transitions. Therefore we assign the lowest energy to the transition from the  $t_{2g}(\text{Cr}) \rightarrow t_{2g}(\text{Mn})$  centered at 13 kK, the middle energy band to the  $t_{2g}(\text{Cr}) \rightarrow e_g(\text{Mn})$  at 16.5 kK and the higher energy band at 21 kK is also  $t_{2g}(\text{Cr}) \rightarrow e_g(\text{Mn})$ . The fine structure in the lower energy band (13800, 13300, 12826, 12444  $\text{cm}^{-1}$ ) may have two origins. One is that they are vibrational structures but the spacings are irregular. The other is that they are due to splitting of the  $t_{2g}$  levels as a consequence of the departure from octahedral symmetry.

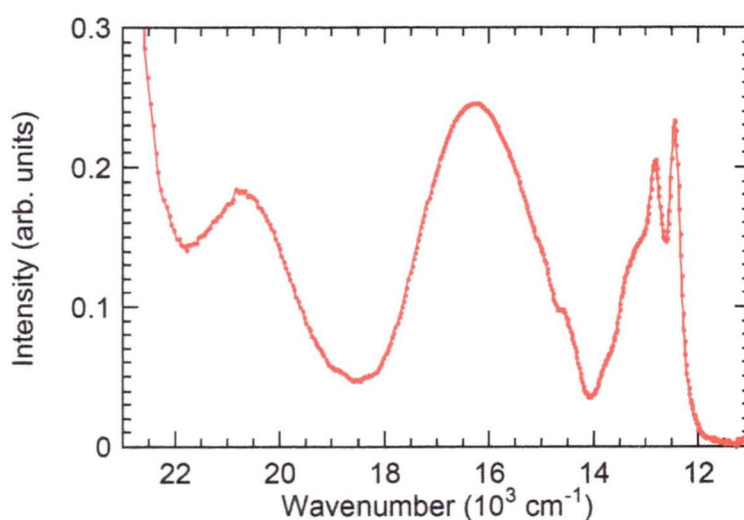


**Figure 3-13.** UV-Vis absorption spectrum measured by transmission through a single crystal of **RGN-LTP** in its virgin state.



### III-3.9. Magnetic properties

All the magnetic data was collected by in-situ measurement. At first, the magnetic measurements for virgin **RGN-LTP** were performed. The same experiments for quenched **RGN-HTP** were duplicated after the sample has been warmed from room temperature to 312 K at a rate of 0.25 K/min and cooled down rapidly to 100 K at a rate of -10 K/min. Then, measurements for relaxed **RGN-LTP** were performed after quenched **RGN-HTP** was annealed by changing the temperature from 280 to 295 K, and back to 280 K at a rate of 0.25 K/min. Afterward, the data for DP were collected after relaxed **RGN-LTP** was dehydrated by heating from 310 to 360 K at a rate of 0.5 K. Finally, those of rehydrated **RGN-LTP** were measured after **RGN-DP** was exposed to air for 2 weeks.

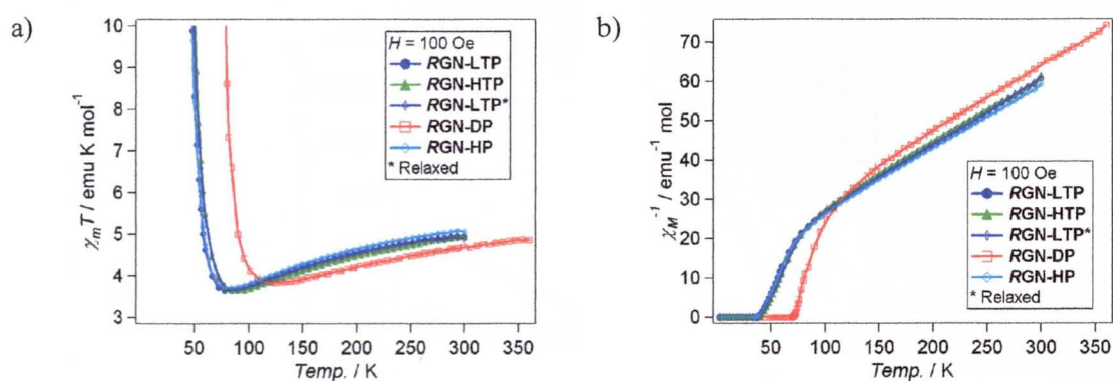


**Figure 3-14.** Temperature dependence of (a)  $\chi_M T$  and (b)  $\chi_M^{-1}$  in an applied field of 100 Oe for virgin **RGN-LTP**, quenched **RGN-HTP**, relaxed **RGN-LTP**, dehydrated **RGN-DP**, and rehydrated **RGN-HP**.

The temperature dependences of  $\chi_M T$  of all compounds are displayed in Figure 3-14a. The  $\chi_M T$  values for virgin **RGN-LTP**, quenched **RGN-HTP**, relaxed **RGN-LTP**, dehydrated **RGN-DP** and rehydrated **RGN-HP** are 4.94, 4.94, 4.90, 4.69 and 5.06  $\text{emu K mol}^{-1}$  at 300 K, and decrease with decreasing temperature down to minimum value of 3.64 (84 K), 3.65 (96 K), 3.65 (84 K), 3.83 (126 K) 3.71  $\text{emu K mol}^{-1}$  (84 K), respectively. Upon further cooling,

$\chi_M T$  increases to a maximum value of 838 (33 K), 885 (33 K), 866 (33 K), 1810 (54 K) and 853  $\text{emu K mol}^{-1}$  (33 K) and decrease below this temperature. Dehydrated **RGN-DP** shows lower  $\chi_M T$  value in the high temperature region and higher maximum value than that of the other phases, indicating strong antiferromagnetic interaction between spin centers.

The  $\chi_M^{-1}$  value for **RGN-LTP**, **RGN-HTP**, relaxed **RGN-LTP**, **RGN-DP**, and **RGN-HP**, follow the Curie-Weiss law ( $\chi_M = C / (T - \theta)$ ) in the range 300 - 114 K, 300 - 126 K, 300 - 108 K, 360 - 162 K and 300 - 108 K with Weiss constants  $\theta$  of -64.6, -73.0, -62.5, -83.3 and -68.3 K, respectively, indicating antiferromagnetic interaction between  $\text{Cr}^{\text{III}}$  and  $\text{Mn}^{\text{II}}$  ions through the cyanide bridge as well as with Curie constants  $C$  of 5.98, 6.06, 5.91, 5.93, and 6.25  $\text{emu K mol}^{-1}$ , respectively, which are in good agreement with theoretical value ( $6.25 \text{ emu K mol}^{-1}$ ).

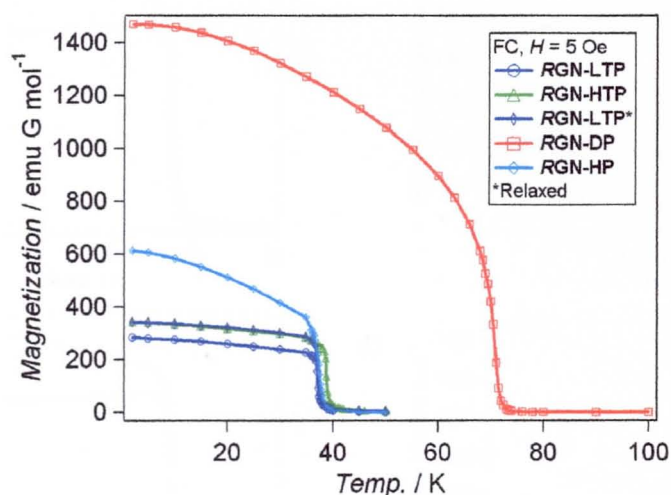
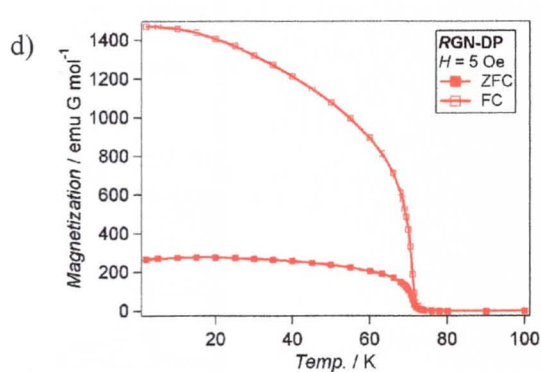
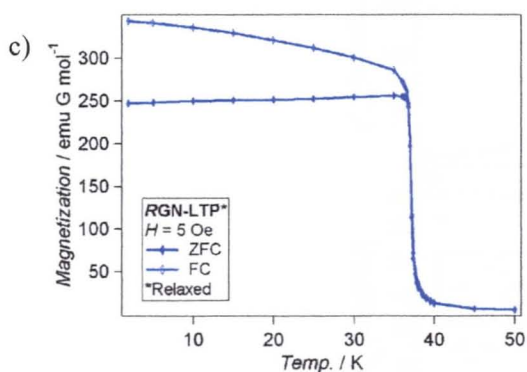
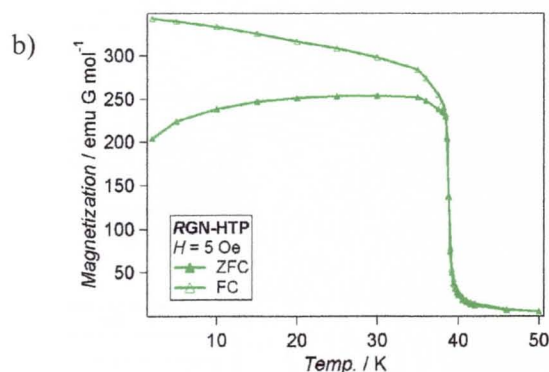
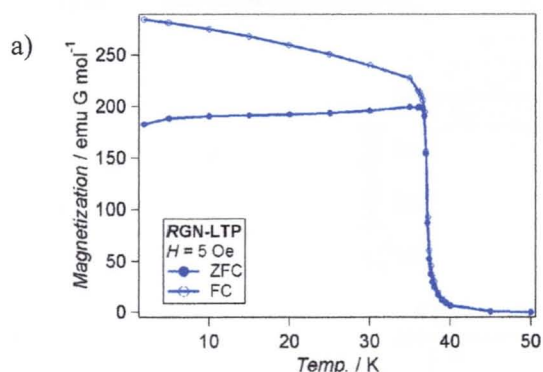


**Figure 3-15.** Temperature dependence of FC magnetization in an applied field of 5 Oe for **RGN-LTP**, **RGN-HTP**, relaxed **RGN-LTP**, **RGN-DP**, and **RGN-HP**.

In the zero-field-cooled (ZFC) and field-cooled (FC) measurement, a long-range magnetic ordering is observed below 38, 39, 38, 73 and 38 K for **RGN-LTP**, **RGN-HTP**, relaxed **RGN-LTP**, **RGN-DP**, and **RGN-HP** (Figure 3-15, 16). Structural phase transition and dehydration increase  $T_C$  up slightly and dramatically. A correlation is seen between the Weiss

constants  $\theta$  and the critical temperature  $T_C$ , except for rehydrated **RGN-LTP**.

The difference of the  $T_C$  value between **RGN-HTP** and **RGN-LTP** can be explained by exchange interaction. For **RGN-LTP**, the average metal separations between Mn and Cr atom in two-dimensional sheets for **RGN-HTP** (5.3249(18) Å), is shorter than that for **RGN-LTP** (5.3457(16) Å). Therefore **RGN-HTP** has more overlap between metal and cyanide ligand orbital than **RGN-LTP**, which gives higher  $T_C$  value for **RGN-HTP**. Meanwhile, the nearly doubled  $T_C$  for **RGN-DP** is assumed to be due to not only increasing number of magnetic neighbors through cyanide group but also shortening distances between Mn and Cr atoms through cyanide group (5.272(8) Å).



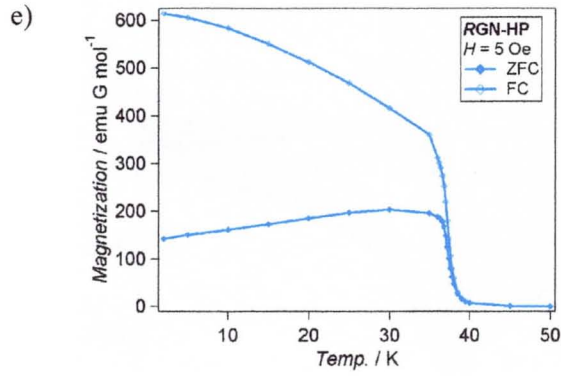


**Figure 3-16.** Temperature dependence of ZFC and FC magnetization for (a) **RGN-LTP**, (b) **RGN-HTP**, (c) relaxed **RGN-LTP**, (d) **RGN-DP**, and (e) **RGN-HP** in an applied field of 5 Oe.

### III-3.10. Ac-susceptibilities

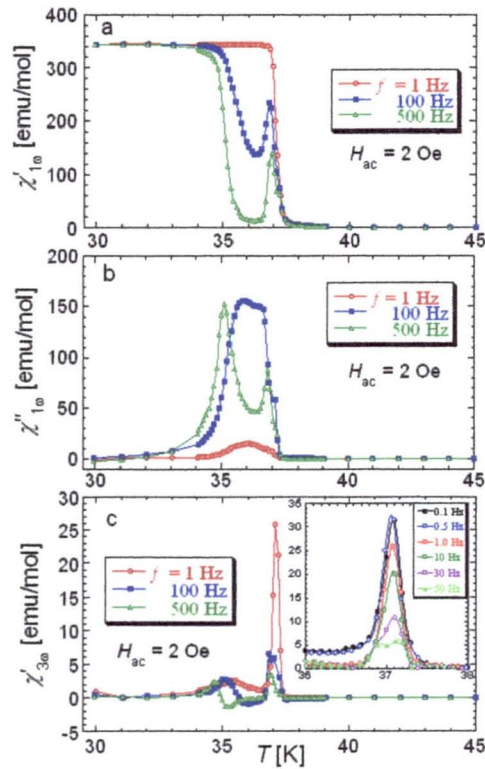


**Figure 3-17.** Frequency dependence of in- and out-of-phases of  $1\omega$  magnetic susceptibility (a, b) and in-phase  $3\omega$  magnetic susceptibility (c) with the external oscillating field applied along the chiral axis,  $a$ -axis, with the amplitude 2 Oe and the frequency  $f = 1, 100, 500$  Hz.

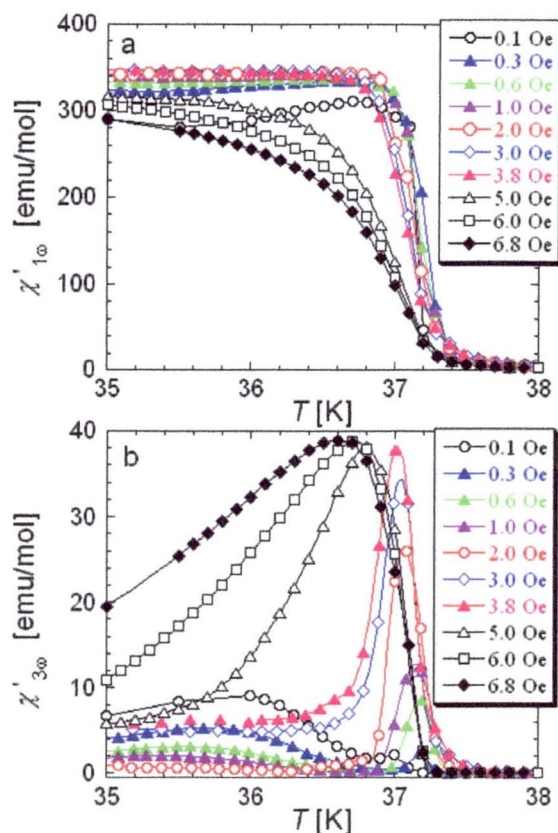


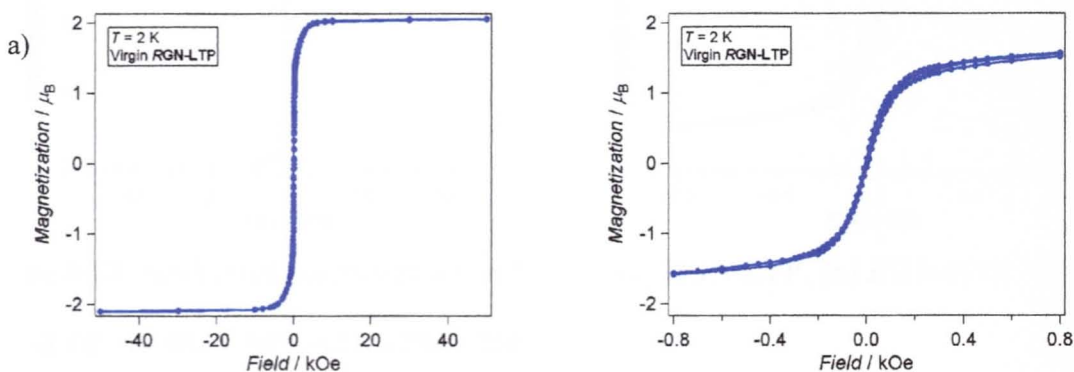
**Figure 3-18.** Ac field amplitude dependence of in-phase  $1\omega$  (a) and  $3\omega$  (b) magnetic susceptibilities against the external oscillating field applied along the chiral axis,  $a$ -axis, with the frequency  $f = 1$  Hz.

An extensive work has been performed on the ac-susceptibility measurements (Figures 3-17 and 18) of this compound by Prof. Masaki Mito and his group at the Kyushu Institute of Technology (Tobata, Kitakyushu), including first and higher harmonics, as a function of frequency, amplitude of the oscillating field, dc-field and temperature as well as external pressure which will be published separately. These measurements were performed on both powdered and aligned single crystals samples prepared by the author and they reveal an anomalous behavior around the magnetic ordering transition which depends on the orientation of the field, the frequency and field of the oscillating field. Very sharp peaks near the transition and an enhancement of the third harmonic at the expense of the first harmonic as a

function of applied field have been associated with resonance effects defining the length scale of the magnetic chirality as proposed by theoretical models using a Dzyaloshinski-Moriya approach. While the sharp anomaly is prominent for  $[\text{Mn}(S\text{-pnH})(\text{H}_2\text{O})][\text{Cr}(\text{CN})_6]\cdot\text{H}_2\text{O}$ , its absence for  $[\text{Mn}(rac\text{-pnH})(\text{H}_2\text{O})][\text{Cr}(\text{CN})_6]\cdot\text{H}_2\text{O}$  is clear indication of the manifestation of the direct relation between structural chirality and magnetic chirality. The presence of a quasi-static mode, also known by Goldstone mode, has been identified. In the ordered state the chiral domain structure appears to lock-in with the frequency of 1 Hz for an applied field of 3.8 Oe. It suffices to say for the present paper that the observation of non-linear susceptibility confirms the long-range magnetic ordering. A preliminary report of these results has already appeared.

### III-3.11. Hysteresis loops

Hysteresis loops were observed for **RGN-DP** and **RGN-HP** at 2 K, but not observed for **RGN-LTP**, **RGN-HTP**, relaxed **RGN-LTP**, (Figure 3-19). The observed saturation magnetization values for **RGN-LTP**, **RGN-HTP**, relaxed **RGN-LTP**, **RGN-DP** and **RGN-HP** were 2.07, 2.06, 2.07, 2.05 and 2.00  $\mu_B$ , respectively, which is in good agreement with the theoretical value of antiferromagnetic coupling between  $\text{Cr}^{3+}$  and  $\text{Mn}^{2+}$  ions ( $5/2 - 3/2 = 1$ ,  $M_S = 2 \mu_B$ ). The largest observed coercive field among all phases is only 40 Oe in **RGN-DP**, describing all phases are soft ferrimagnets.



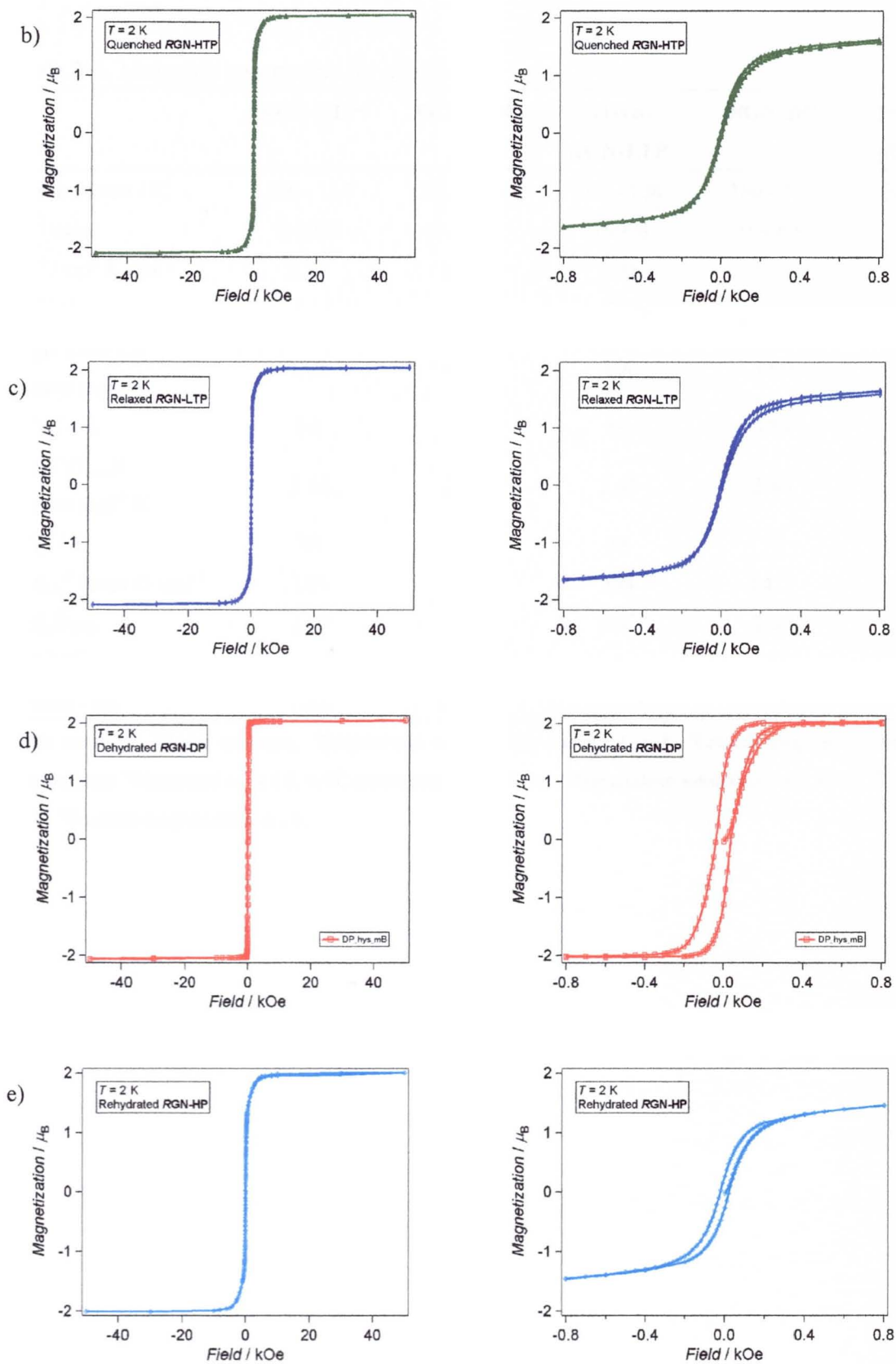


Figure 3-19. Isothermal magnetization at 2 K for (a) **RGN-LTP**, (b) **RGN-HTP**, (c) relaxed **RGN-LTP**, (d) **RGN-DP**, and (e) **RGN-HP**.

**Table 3-4.** Magnetic parameters for all phases

	<b>RGN-LTP</b>	<b>RGN-HTP</b>	relaxed <b>RGN-LTP</b>	<b>RGN-DP</b>	rehydrated <b>RGN-HP</b>
<i>Fitting area / K</i>	300 - 114	300 - 126	300 - 108	360 - 162	300 - 108
<i>R<sup>2</sup> value</i>	0.9999	0.9997	0.9998	0.9998	0.9998
<i>C<sup>a</sup> / cm<sup>3</sup> K mol<sup>-1</sup></i>	5.98	6.07	5.91	5.93	6.25
<i>ϕ / K</i>	- 64.6	- 73.0	- 62.5	- 83.3	-68.3
<i>χ<sub>M</sub>T (300 K) / emu mol<sup>-1</sup> K</i>	4.94	4.94	4.90	4.69	5.06
<i>T<sub>min</sub><sup>c</sup> / K</i>	84	96	84	126	84
<i>χ<sub>M</sub>T (T<sub>min</sub>) / emu mol<sup>-1</sup> K</i>	3.64	3.65	3.65	3.83	3.71
<i>T<sub>C</sub><sup>d</sup> / K</i>	38	39	38	73	38
<i>M<sub>2K</sub><sup>e</sup> / emu G mol<sup>-1</sup></i>	285	344	344	1471	614
<i>M<sub>sat</sub><sup>f</sup> / μ<sub>B</sub></i>	2.07	2.06	2.07	2.05	2.00
<i>H<sub>C</sub><sup>g</sup> / Oe</i>	5	4	6	40	20
<i>M<sub>REM</sub><sup>h</sup> / μ<sub>B</sub></i>	0.062	0.055	0.074	1.128	0.267

<sup>a</sup>Curie constants. <sup>b</sup>Weiss constants. <sup>c</sup>Temperatures at minimum values of  $\chi_M T$ . <sup>d</sup>Critical temperatures based on FC measurements. <sup>e</sup>Magnetization at 2 K in FC measurement ( $H = 5$  Oe). <sup>f</sup>Magnetization saturation value at 2 K. <sup>g</sup>Coercive field at 2 K. <sup>h</sup>Remnant magnetization at 2 K.



### III-3.12. Isothermal magnetization on single crystals

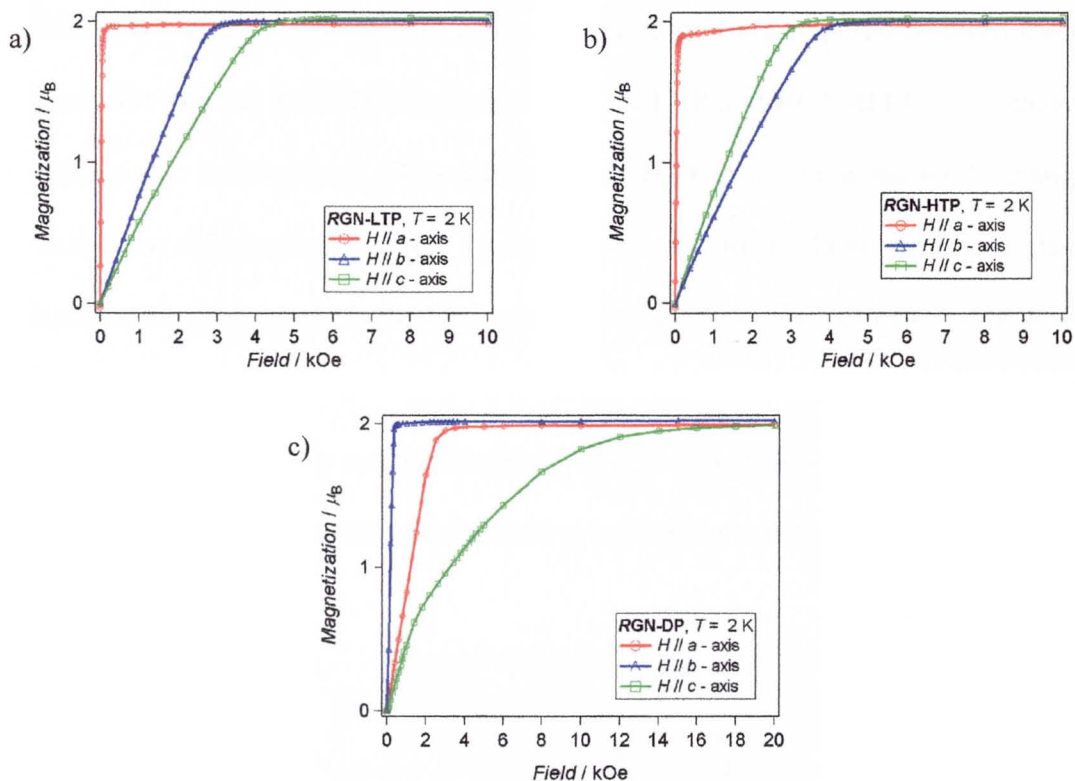


**Figure 3-20.** Initial Magnetization curves for (a) **RGN-LTP**, (b) **RGN-HTP**, and (c) **RGN-DP** at 2 K. Magnetic field was applied along the three principal crystallographic axes.

All phases have different magnetic anisotropy. For **RGN-LTP**, the initial magnetization curves for the three principal crystallographic axes are shown in figure 3-20 and the saturation value for each axis, each phase is in table 3-5. As can be seen the easy, intermediate and hard axes are  $a$ -,  $b$ - and  $c$ -axis and the magnetizations with field applied along these axes saturate at 100, 3000 and 4500 Oe, respectively. This magnetic anisotropy is changed after structural phase transition and dehydration. For the quenched **RGN-HTP** the easy, intermediate and hard axes are  $a$ -,  $c$ - and  $b$ -axis and saturation of magnetizations are reached at 50, 3500 and 4500 Oe, respectively. For **RGN-DP** the easy, intermediate and hard axes are  $b$ -,  $a$ - and  $c$ -axis and saturation at 400, 2500 and 16000 Oe, respectively. In all these cases the easy axis of magnetization remains within the Mn-Cr layer but rotates from  $a$ - to  $b$ -axis upon dehydration. The intermediate axis rotates from  $b$ - for **RGN-LTP** to  $c$ - for **RGN-HTP** and to  $a$ -axis for

**RGN-DP.** The hard axis changes from *c*- for **RGN-LTP** to *b*- for **RGN-HTP** and back to *c*-axis for **RGN-DP**. One noticeable change is the large field required to align the moment along the hard axis for **RGN-DP** compared to **RGN-LTP** and **RGN-HTP**. The reason for the intermediate axis rotation from **RGN-LTP** to **RGN-HTP** is not expected while change of the easy axis upon dehydration may not be so unusual due to the large structural change that accompanies the process where the homometal distance along *b*-axis in **RGN-DP** is shortened. During the measurement, the hard- and intermediate-axis change from **RGN-LTP** to **RGN-HTP** was observed by rotating sample (Figure 3-21). The dehydration was easily found from the drop of the magnetization value during heating the sample (Figure 3-22).

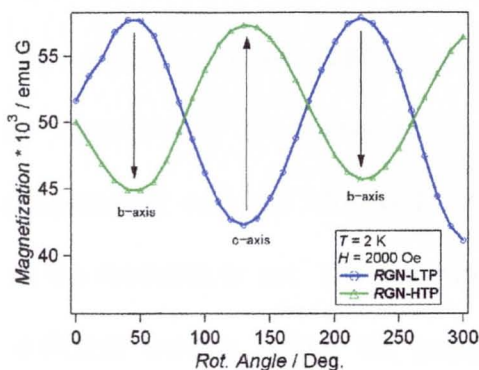


**Figure 3-21.** Angular dependence of the magnetization for **RGN-LTP** (blue) and **RGN-HTP** (green) at 2 K showing the change of anisotropy.

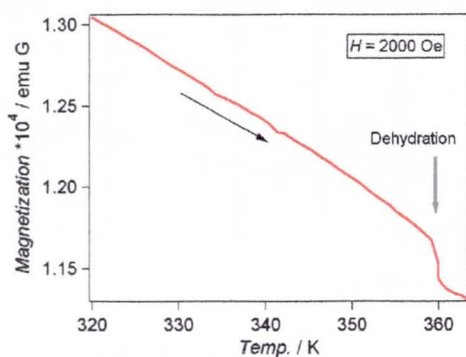


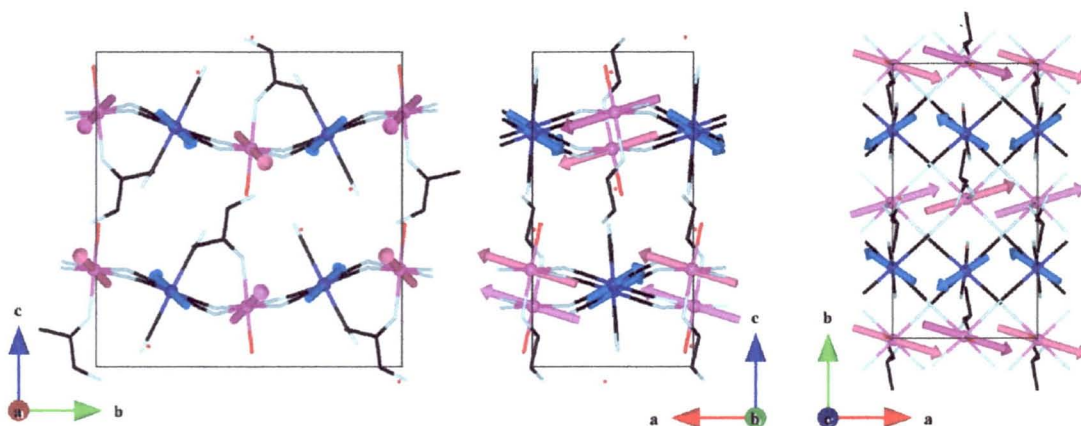
**Figure 3-22.** Magnetization change upon dehydration measured on a single crystal.

**Table 3-5.** Magnetic field when magnetization is saturated along each axis for all phases.

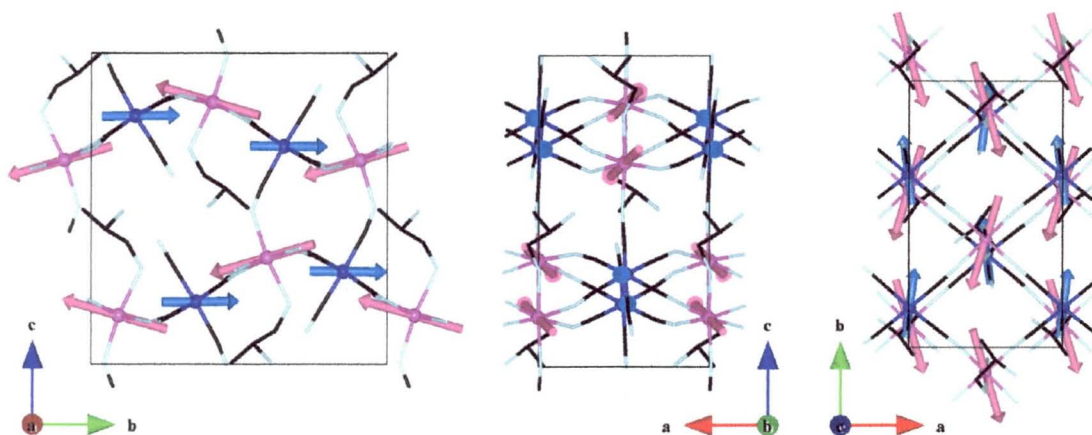
	<i>RGN-LTP</i>	<i>RGN-HTP</i>	<i>RGN-DP</i>
Easy axis, sat. Field / Oe	<i>a</i> -axis, 100	<i>a</i> -axis, 50	<i>b</i> -axis, 400
Intermediate axis, sat. Field / Oe	<i>b</i> -axis, 3000	<i>c</i> -axis, 3500	<i>a</i> -axis, 2500
Hard axis, sat. Field / Oe	<i>c</i> -axis, 4500	<i>b</i> -axis, 4500	<i>c</i> -axis, 16000

### III-3.13. Magnetic structures

The magnetic structures were determined by Clara Gonzalez at the Institute Laue Langevin (Grenoble, France) on samples prepared by the author, using a combination of single-crystal diffraction on the VIVALDI Laue diffractometer and D10. Using group analysis for the orthorhombic space-group the diffraction data were found to satisfy a  $\Gamma_4$  irreducible representation for **LTP** and **HTP** but a  $\Gamma_3$  for **DP**. This means antiferromagnetic alignment of Cr and Mn moments along the *a*-axis for **LTP** and **HTP** and along the *b*-axis for **DP** (Figures 3-23 and 24). Although the directions of the moments in the different phases and the ferrimagnetism are in good agreement with the observed magnetization measurements on single-crystals, the canting of the moments is not. The theoretical prediction of the magnetic Bragg intensities for the different models within the group analysis may have to be reconsidered.



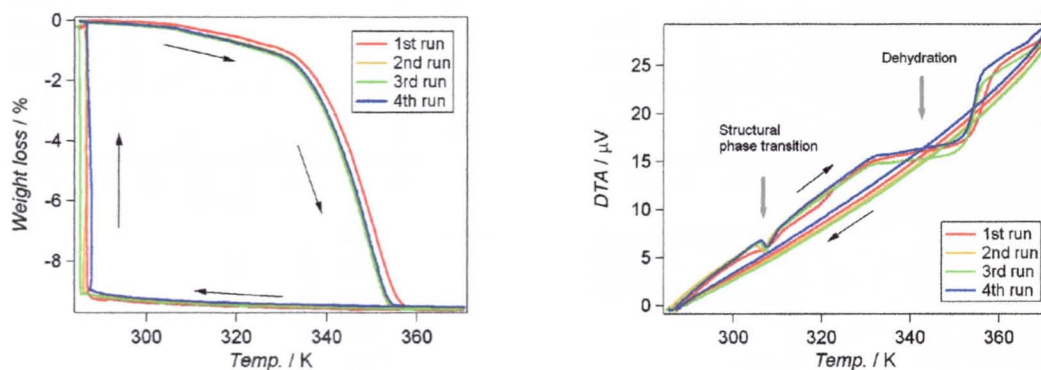
**Figure 3-23.** Magnetic structure of *RGN-LTP* of GN corresponding to  $\Gamma_4$ . Views along the *a*, *b* and *c* axes.



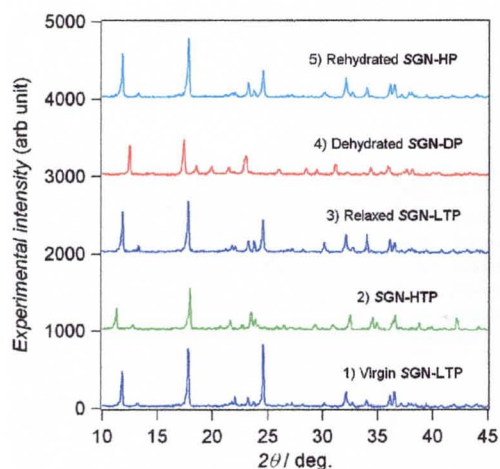
**Figure 3-24.** Magnetic structure of **RGN-DP** of GN corresponding to  $\Gamma_3$ . Views along the  $a$ ,  $b$  and  $c$  axes.

### III-3.14. Conformation of structural phase transition and dehydration for *S*-isomer $[\text{Mn}(\text{S-pnH})(\text{H}_2\text{O})][\text{Cr}(\text{CN})_6]\cdot\text{H}_2\text{O}$

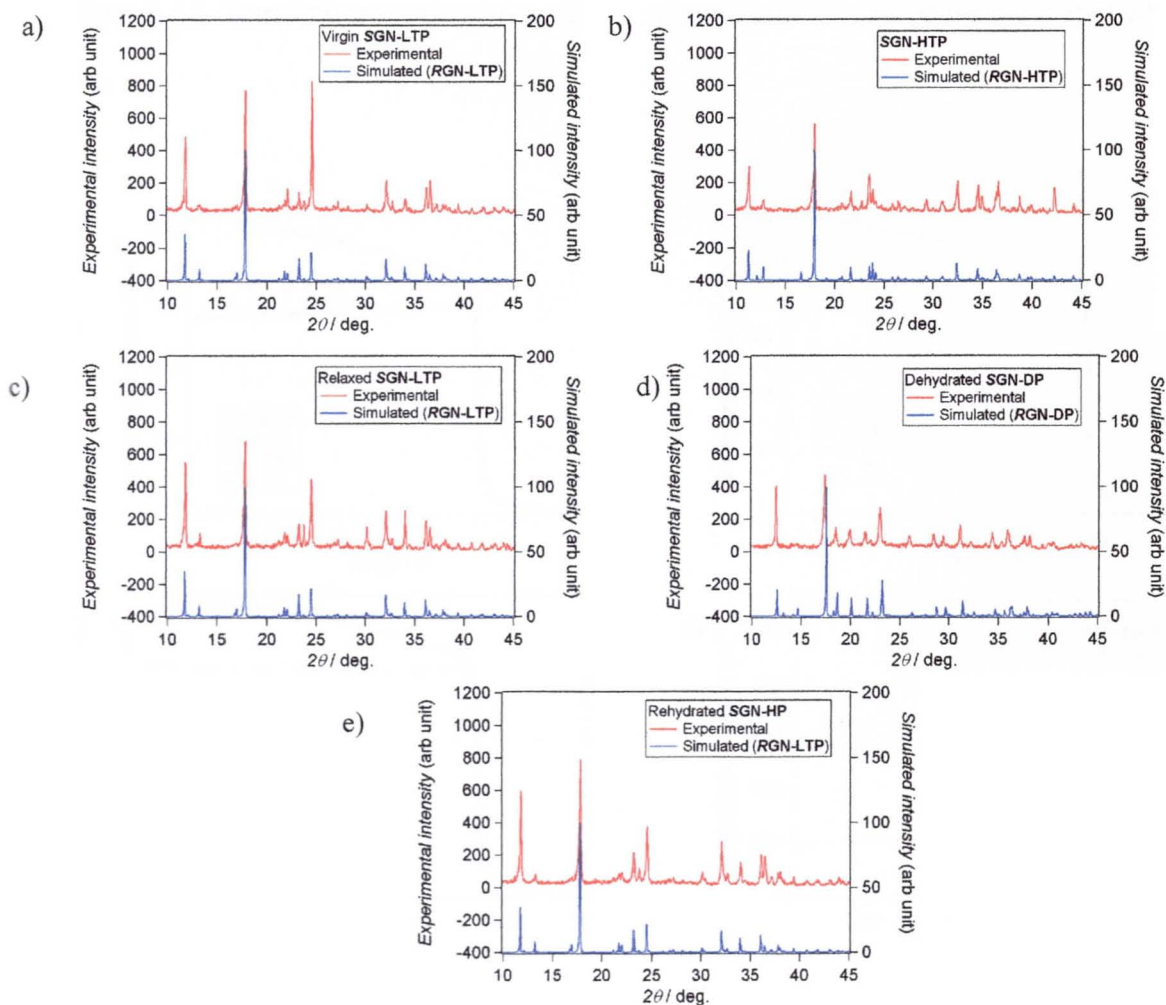
The reversible structural phase transition and dehydration for *S*-isomer of GN are confirmed through TG-DTA measurement (Figure 3-25), powder X-ray diffraction (Figure 3-26, 27), and zero-field-cooled, field-cooled measurements (Figure 3-28, 29)



**Figure 3-25.** (a) Thermogravimetric and (b) DTA for **SGN-LTP** for several dehydration and rehydration cycles in the low temperature region (the black arrows point to the temperature cycle and the gray arrows to the transformations).

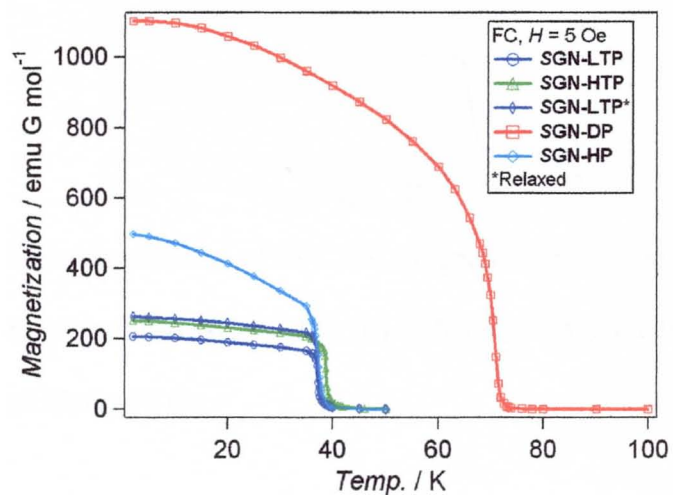


**Figure 3-26.** Experimental XRPD ( $\text{Cu K}\alpha$ ) patterns for virgin **SGN-LTP**, **SGN-HTP**, relaxed **SGN-LTP**, dehydrated **SGN-DP**, and rehydrated **SGN-HP** from bottom to top.

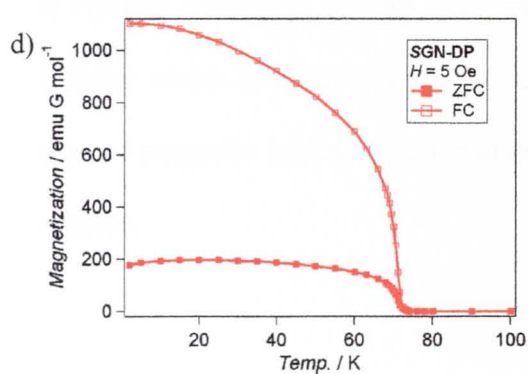
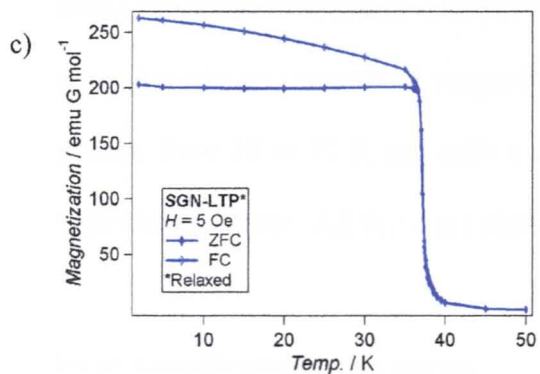
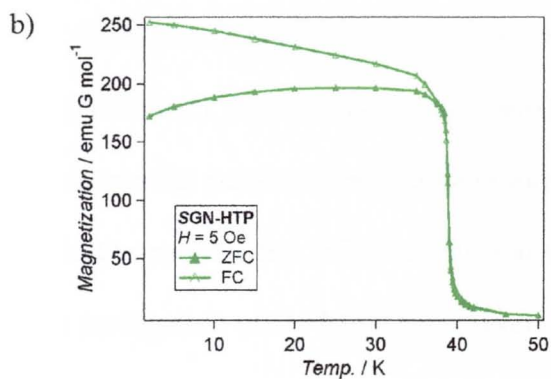
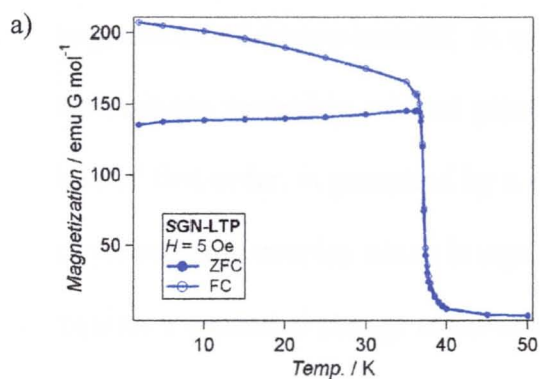


**Figure 3-27.** Experimental XRPD ( $\text{Cu K}\alpha$ ) patterns with simulated patterns from *R*-isomer crystallographic data for (a) **SGN-LTP**, (b) **SGN-HTP**, (c) relaxed **SGN-LTP**, (d) **SGN-DP**, and (e) rehydrated **SGN-HP**.

and (e) SGN-HP.



**Figure 3-28.** Temperature dependence of FC magnetization for all phase in an applied field of 5 Oe.



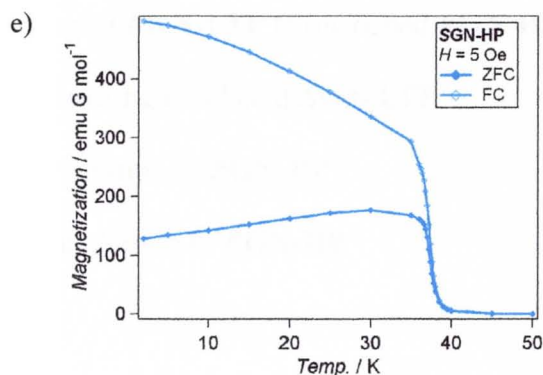


**Figure 3-29.** Temperature dependence of ZFC, FC magnetization for (a) virgin **SGN-LTP**, (b) quenched **SGN-HTP**, (c) relaxed **SGN-LTP**, (d) dehydrated **SGN-DP**, and (e) rehydrated **SGN-HP** in an applied field of 5 Oe.

### III-4. Conclusion


$[\text{Mn}\{(R/S)\text{-pnH}\}(\text{H}_2\text{O})][\text{Cr}(\text{CN})_6]\cdot\text{H}_2\text{O}$  prove to be the compounds with the highest number of functionalities which include heterometallic mixed-valency, chirality, ferrimagnetism and proton-transfer, as well as surviving two single crystal-to-single crystal phase transitions reversibly without great loss of crystallinity. One of the phase transitions, which is of first-order, is promoted by a rare proton-transfer between amine/ammonium and water/hydroxonium couples which brings changes in the coordination of the amine and water and requires a concerted change of curvature of the corrugation of the Mn-CN-Cr layers as is commonly observed in muscles. Dehydration of the crystals introduces bridges between the layers resulting to an increase in magnetic dimensionality which in-turn enhances the Curie temperature from 38 to 73 K and adds a small amount of magnetic hardness and changes to the magnetic anisotropy. All these are absolutely reversible.


### Movies of transformation processes.


Movie 3-1 : 02 Movie **RGN-LTP** to **RGN-HTP** 

Movie 3-2 : 05 Movie **RGN-HTP** to relaxed **RGN-LTP** 

Movie 3-3 : 07 Movie relaxed **RG**N-LTP to quenched **RG**N-HTP 

Movie 3-4 : 09 Movie Annealing to relaxed **RG**N-LTP 

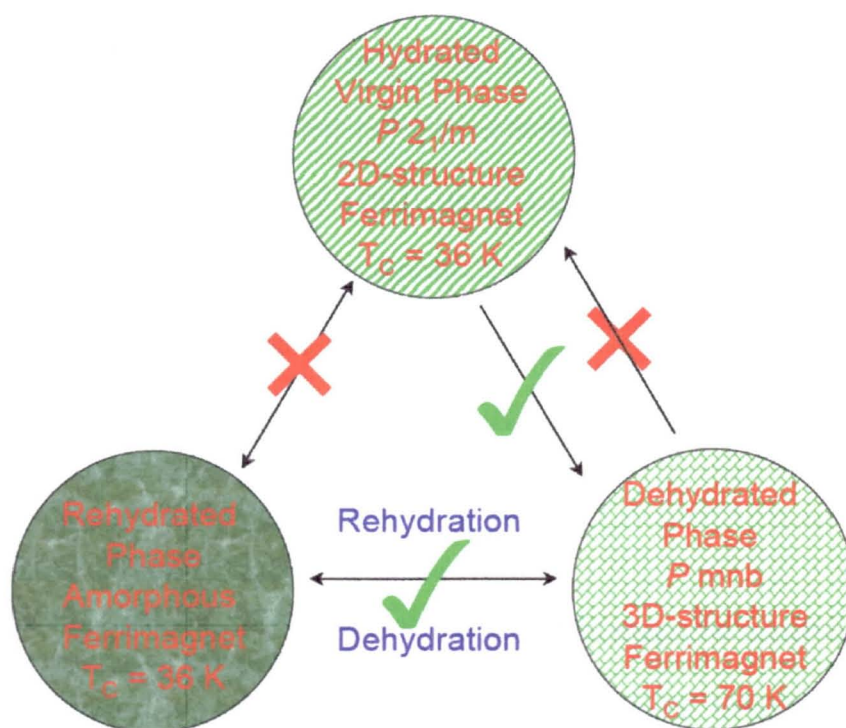
Movie 3-5 : 11 Movie dehydration to **RG**N-DP 

Movie 3-6 : 13 Movie Rehydration to **RG**N-HP 



## Chapter IV

### [Mn(*rac*-pnH)(H<sub>2</sub>O)][Cr(CN)<sub>6</sub>]·H<sub>2</sub>O: Reversible Dehydration-Rehydration Induces Increment-Decrement of Dimensionality, Curie Temperature and Magnetic Hardness



## Chapter IV

### **[Mn(*rac*-pnH)(H<sub>2</sub>O)][Cr(CN)<sub>6</sub>]·H<sub>2</sub>O: Reversible Dehydration-Rehydration Induces Increment-Decrement of Dimensionality, Curie Temperature and Magnetic Hardness**

#### IV-1. Abstract

We report the synthesis, crystal structure and magnetic properties of the two-dimensional achiral soft-ferrimagnet [Mn(*rac*-pnH)(H<sub>2</sub>O)][Cr(CN)<sub>6</sub>]·H<sub>2</sub>O (*rac*GN, pn = 1,2-diaminopropane) as a comparison to the well-investigated two-dimensional chiral enantiopure ferrimagnets [Mn(*R/S*-pnH)(H<sub>2</sub>O)][Cr(CN)<sub>6</sub>]·H<sub>2</sub>O (*RGN-LTP/SGN-LTP*). *rac*GN crystallizes in the monoclinic achiral *P* 2<sub>1</sub>/m space-group having a two-dimensional square-network of Mn-Cr with bridging cyanide, and behaves as a soft ferrimagnet below 36 K. *rac*GN shows reversible dehydration-rehydration where the crystal structure of the dehydrated *rac*GN-DP is formed of a three-dimensional network with an additional cyanide bridge and adopts the orthorhombic achiral *P* mnb space-group. *rac*GN-DP exhibits a ferrimagnetic behavior at 70 K and coercive field at 2 K of 63 Oe which are nearly doubled the critical temperature and 8 times the coercive field of the virgin sample.

#### IV-2. Introduction

There is growing interest in exploring multifunctional magnetic materials, in particular in the search for organic-inorganic hybrid materials combining magnetism with electrical properties,<sup>9</sup> optical properties,<sup>26,27</sup> photoreactivity,<sup>7</sup> guest sensitive Curie temperature,<sup>8</sup> and chirality.<sup>14-18</sup> These materials are not only of interest for their novelty with multifunctionalities but are also desired for academic purposes to understand the way electrons interact in hybrid systems to generate coupled phenomena. In this context, chirality and/or porosity with magnetism is of special interest. The materials of this category are believed to open new

windows for new devices.<sup>10-11</sup> The chiral magnet  $[\text{Mn}(S\text{-pnH})(\text{H}_2\text{O})][\text{Cr}(\text{CN})_6]\cdot\text{H}_2\text{O}$  (**SGN-LTP**) was reported by our group employing the simplest chiral diamine ligand in 2003.<sup>15</sup> This compound belongs to the orthorhombic chiral space-group  $P 2_12_12_1$  and it adopts a two-dimensional network structure. Below the Curie temperature ( $T_C = 38$  K) the saturation magnetization is  $2 \mu_B$ , which are in good agreement with the theoretical value for an antiferromagnetic ordering of  $\text{Cr}^{3+}$  ( $S = 3/2$ ) and  $\text{Mn}^{2+}$  ( $S = 5/2$ ) ions. So far, other investigation using ESR,  $\mu$ -SR, neutron powder diffraction, single crystal neutron diffraction have been performed and all points to novel physical phenomenon in molecular magnet with chiral space-group.<sup>19</sup> Although, these measurements have been done only with enantiopure chiral compound **RGN-LTP/SGN-LTP**, a test of this conclusion using the racemic compound is crucial. In addition to these studies on the **RGN-LTP/SGN-LTP**, we have demonstrated earlier that several ground states can be stabilized as a function of either temperature or water content as well the reversible conversions between them with the associated physical properties.

Here, we report the synthesis, single-crystal structure determinations of the two different forms, thermogravimetric analyses, optical spectroscopy and the magnetic properties of the achiral magnet  $[\text{Mn}(\text{rac-pnH})(\text{H}_2\text{O})][\text{Cr}(\text{CN})_6]\cdot\text{H}_2\text{O}$  (**racGN**) as a reference to the chiral magnet **RGN-LTP/SGN-LTP** and shows that certain basic properties are similar.

### **IV-3. Results and discussion**

#### **IV-3.1. Crystal structures**

We recently observed reversible single crystal-to-single crystal transformation associated with a structural phase transition and dehydration of  $[\text{Mn}(R\text{-pnH})(\text{H}_2\text{O})][\text{Cr}(\text{CN})_6]\cdot\text{H}_2\text{O}$  (**RGN-LTP**). These results motivated us to investigate other stable ground states as a function of the temperature. A similar in-situ crystal structure analysis study was undertaken starting

from a virgin crystal for *racGN*. Crystallographic Data for all phases achieved are given in table 4-1 and a list of the bond distances and angles is given in table 4-2.

When the crystal was heated to 360 K, the diffraction patterns change (see movie 4-1) and crystal structure of the dehydrated phase (*racGN-DP*) was obtained successfully. After the structural analysis of the dehydrated phase, the crystal was exposed to the air and the diffraction spots change were monitored for 2 hours (see movie 4-2). Unit cell parameters obtained from these spots are almost the same as those of the virgin crystal, but the spots were too broad to realize a full crystal structure. However, when the hydrated crystal was heated to 360 K again, the dehydrated crystal structure was restored (see movie 4-3). Subsequently, the crystal was kept in the small plastic box with water at 298 K for 1 week, but the results were the same as the previous hydrated crystal. The quality of the spots was again too diffuse to permit the determination of the crystal structure. As can be seen in the figure 4-2, the crystal was transformed from one state to the other. We have listed the structure determinations by numbers in blue color and the transformation processes from one state to the other in red. The transformation processes have been recorded in in-situ movies except for the last hydration. We describe below the structures of virgin (*racGN*) and dehydrated phase (*racGN-DP*) and discuss the changes at the different stage.

**Table 4-1.** Crystallographic Data for virgin *racGN* (1), dehydrated *racGN-DP*(3), rehydrated *racGN-HP* (5), dehydrated *racGN-DP* (7), rehydrated *racGN-HP* (9).

Compound	1 <sup>a</sup> : <i>racGN</i>	3 <sup>a</sup> : <i>racGN-DP</i> <sup>b</sup>	5 <sup>a</sup> : <i>racGN-HP</i> <sup>c</sup>	7 <sup>a</sup> : <i>racGN-DP</i> <sup>d</sup>	9 <sup>a</sup> : <i>racGN-HP</i> <sup>e</sup>
formula	C <sub>9</sub> H <sub>15</sub> CrMnN <sub>8</sub> O <sub>2</sub>	C <sub>9</sub> H <sub>11</sub> CrMnN <sub>8</sub>	C <sub>9</sub> H <sub>15</sub> CrMnN <sub>8</sub> O <sub>2</sub>	C <sub>9</sub> H <sub>11</sub> CrMnN <sub>8</sub>	C <sub>9</sub> H <sub>15</sub> CrMnN <sub>8</sub> O <sub>2</sub>
fw	374.23	338.20	374.23	338.20	374.23
<i>T</i> , K	298	298	298	298	298
atmosphere	Air	Nitrogen	Air	Nitrogen	Air
exposure time, sec	25	40	40	40	25
no. of frames	1010	710	970	1050	1280
crystal system	Monoclinic	Orthorhombic	Monoclinic	Orthorhombic	Monoclinic
space-group	<i>P</i> 2 <sub>1</sub> / <i>m</i>	<i>P</i> mnb <sup>g</sup>	-	<i>P</i> mnb <sup>g</sup>	-
<i>a</i> , Å	7.6945(14)	7.730(4)	7.631(5)	7.7245(12)	7.696(4)
<i>b</i> , Å	14.543(3)	13.627(7)	14.430(9)	13.609(2)	14.556(8)
<i>c</i> , Å	7.9749(14)	14.064(7)	7.925(5)	14.061(2)	7.996(4)
$\beta$ , °	110.918(3)	90	110.958(11)	90	110.941(9)
<i>V</i> , Å <sup>3</sup>	833.6(3)	1481.4(14)	815.0(9)	1478.1(4)	836.6(8)
<i>Z</i>	2	4	-	4	-
<i>D</i> <sub>C</sub> , g/cm <sup>3</sup>	1.491	1.516	-	1.520	-
$\mu$ (Mo K $\alpha$ ), mm <sup>-1</sup>	1.424	1.584	-	1.588	-
crystal size, mm <sup>3</sup>	0.5 x 0.2 x 0.05	0.5 x 0.2 x 0.05	0.5 x 0.2 x 0.05	0.5 x 0.2 x 0.05	0.5 x 0.2 x 0.05
<i>T</i> <sub>min</sub> and <i>T</i> <sub>max</sub>	0.7364, 1.0000	0.7775, 1.0000	-	0.7891, 1.0000	-
$\theta$ <sub>min</sub> and $\theta$ <sub>max</sub> , deg	2.734, 27.66	2.896, 24.14	-	2.994, 25.18	-
total no. of reflections	4042	4755	-	6945	-
no. of unique reflections ( <i>R</i> <sub>int</sub> )	1916	1764	-	1792	-
no. of observed [ <i>I</i> ≥ 2σ( <i>I</i> )]	1512	1064	-	1101	-
no. of parameters	125	112	-	112	-
<i>R</i> 1 / <i>wR</i> 2 [ <i>I</i> ≥ 2σ( <i>I</i> )]	0.0364, 0.0949	0.0559, 0.1224	-	0.0492, 0.1101	-
<i>R</i> 1 / <i>wR</i> 2 (all data)	0.0476, 0.1008	0.1018, 0.1350	-	0.0882, 0.1197	-
GOF	0.975	0.928	-	0.936	-
$\Delta\rho$ e/Å <sup>3</sup>	-0.283, 0.622	-0.549, 1.138	-	-0.318, 0.879	-

<sup>a</sup>Numbers correspond to the figure 4-2. <sup>b</sup>Data were collected after the virgin *racGN* sample was heated to 360 K at a rate of 2 K/min and cooled down to 298 K at a rate of -10 K/min. under a nitrogen atmosphere. <sup>c</sup>Data were collected after *racGN-DP* was exposed to air at 298 K for 2 hours. <sup>d</sup>Data were collected after rehydrated *racGN-HP* was heated to 360 K at a rate of 2 K/min and cooled down to 298 K at a rate of -10 K/min. under nitrogen atmosphere. <sup>e</sup>Data were collected after *racGN-DP* was kept in the small plastic box with water at 298 K for 1 week. <sup>f</sup>Max and min residual density. <sup>g</sup>This space-group is the same as the symmetry for *P* nma (No. 62) which is employed for uniform definition of axes for the *RGN* series.

Table 4-2. Selected bond distances, angles and metal separations for virgin *rac*GN and dehydrated *rac*GN-DP.

Selected bond distances (Å) for octahedral geometries for Mn and Cr.

	<i>rac</i> GN		<i>rac</i> GN-DP
Mn(1)-N(1)	2.225(2)	Mn(1)-N(1)	2.217(4)
Mn(1)-N(2)	2.212(2)	Mn(1)-N(2)	2.191(4)
Mn(1)-O(1)	2.214(3)	Mn(1)-N(3)	2.258(6)
Mn(1)-N(6)	2.307(4)	Mn(1)-N(5)	2.437(9)
Cr(1)-C(1)	2.075(3)	Cr(1)-C(1)	2.090(5)
Cr(1)-C(2)	2.068(3)	Cr(1)-C(2)	2.065(4)
Cr(1)-C(3)	2.059(3)	Cr(1)-C(3)	2.085(7)

Bond angles (°) for octahedral geometries for Mn and Cr.

	<i>rac</i> GN		<i>rac</i> GN-DP
N(1)-Mn(1)-N(2)	91.06(10)	N(1)-Mn(1)-N(2)	88.51(15)
N(1)-Mn(1)-N(1) <sup>#1</sup>	88.87(13)	N(1)-Mn(1)-N(3)	97.50(14)
N(1)-Mn(1)-N(6)	88.03(9)	N(1)-Mn(1)-N(1) <sup>#3</sup>	89.87(19)
N(1)-Mn(1)-O(1)	90.84(8)	N(1)-Mn(1)-N(5)	90.19(19)
N(2)-Mn(1)-N(2) <sup>#1</sup>	89.00(13)	N(2)-Mn(1)-N(3)	92.26(15)
N(2)-Mn(1)-N(6)	92.22(9)	N(2)-Mn(1)-N(2) <sup>#3</sup>	91.5(2)
N(2)-Mn(1)-O(1)	88.91(9)	N(2)-Mn(1)-N(5)	80.20(19)
N(1)-Mn(1)-N(2) <sup>#1</sup>	179.74(9)	N(1)-Mn(1)-N(2) <sup>#3</sup>	170.24(16)
O(1)-Mn(1)-N(6)	178.42(12)	N(3)-Mn(1)-N(5)	169.1(3)
C(1)-Cr(1)-C(2)	89.78(10)	C(1)-Cr(1)-C(2)	89.90(17)
C(1)-Cr(1)-C(3)	88.13(11)	C(1)-Cr(1)-C(3)	94.24(17)
C(1)-Cr(1)-C(2) <sup>#2</sup>	90.22(10)	C(1)-Cr(1)-C(4)	89.2(2)
C(1)-Cr(1)-C(3) <sup>#2</sup>	91.87(11)	C(1)-Cr(1)-C(1) <sup>#4</sup>	90.2(2)
C(2)-Cr(1)-C(3)	88.80(11)	C(2)-Cr(1)-C(3)	88.86(19)
C(2)-Cr(1)-C(3) <sup>#2</sup>	91.20(11)	C(2)-Cr(1)-C(4)	87.7(2)
		C(2)-Cr(1)-C(2) <sup>#4</sup>	89.8(3)
		C(1)-Cr(1)-C(2) <sup>#4</sup>	176.88(19)
		C(3)-Cr(1)-C(4)	175.1(3)

Symmetry codes: #1  $x, -y+1/2, z$ ; #2  $-x, -y, -z$ ; #3  $-x+3/2, y, z$ ; #4  $-x+1/2, y, z$ .

Selected bond angles (°) for two-dimensional sheet.

	<i>racGN</i>		<i>racGN-DP</i>
C(1)-N(1)-Mn(1)	162.9(2)	C(1)-N(1)-Mn(1)	169.5(4)
C(2) <sup>#1</sup> -N(2)-Mn(1)	166.4(2)	C(2) <sup>#3</sup> -N(2)-Mn(1)	159.1(4)
C(3)-N(3)-Mn(1)		C(3) <sup>#4</sup> -N(3)-Mn(1)	147.5(5)
N(1)-C(1)-Cr(1)	177.2(2)	N(1)-C(1)-Cr(1)	177.0(4)
N(2) <sup>#2</sup> -C(2)-Cr(1)	177.4(2)	N(2) <sup>#5</sup> -C(2)-Cr(1)	174.3(4)
N(3)-C(3)-Cr(1)		N(3) <sup>#6</sup> -C(3)-Cr(1)	172.8(6)

Symmetry codes: #1 x+1,y,z; #2 x-1,y,z; #3 x,y+1/2,-z+1/2; #4 -x+1,-y+1/2,z+1/2; #5 x,y-1/2,-z+1/2; #6 -x+1,-y+1/2,z-1/2.

Distances for hydrogen bonds (Å).

	<i>racGN</i>
N(5)⋯O(2)	2.781(11)
O(1)⋯N(3) <sup>#1</sup>	2.785(3)

Symmetry codes: #1 x, y, -1+z.

Intra-network metal separations (Å) through one cyanide group.

	<i>racGN</i>		<i>racGN-DP</i>
Mn(1)⋯Cr(1) <sup>a</sup>	5.3644(8)	Mn(1)⋯Cr(1) <sup>c</sup>	5.430(2)
Mn(1)⋯Cr(1) <sup>#1, b</sup>	5.3814(8)	Mn(1)⋯Cr(1) <sup>#2, d</sup>	5.276(2)
Mn(1)⋯Cr(1) <sup>#3 c</sup>		Mn(1)⋯Cr(1) <sup>#3 e</sup>	5.201(3)
Mn(1)⋯Cr(1) (Ave.)	5.3729(11)	Mn(1)⋯Cr(1) (Ave.)	5.323(4)

Metal separation through <sup>a</sup>C(1)-N(1), <sup>b</sup>C(2)-N(2), <sup>c</sup>C(3)-N(3). Symmetry codes: #1 x+1, y, z; #2 x, y+1/2, -z+1/2; #3 -x+1, -y+1/2, z+1/2.

Selected intra-network metal separations (Å) through two cyanide groups.

	<i>racGN</i>		<i>racGN-DP</i>
Mn(1)⋯Mn(1) <sup>#1, d</sup>	7.694(2)	Mn(1)⋯Mn(1) <sup>#1, d</sup>	7.730(4)
Mn(1)⋯Mn(1) <sup>#2, d</sup>	7.694(2)	Mn(1)⋯Mn(1) <sup>#2, d</sup>	7.730(4)
Mn(1)⋯Mn(1) <sup>#3, e</sup>	7.5012(15)	Mn(1)⋯Mn(1) <sup>#7, e</sup>	7.317(4)
Mn(1)⋯Mn(1) <sup>#4, e</sup>	7.5012(15)	Mn(1)⋯Mn(1) <sup>#8, e</sup>	7.317(4)
Cr(1)⋯Cr(1) <sup>#1, d</sup>	7.6945(14)	Cr(1)⋯Cr(1) <sup>#1, d</sup>	7.730(4)
Cr(1)⋯Cr(1) <sup>#2, d</sup>	7.6945(14)	Cr(1)⋯Cr(1) <sup>#2, d</sup>	7.730(4)
Cr(1)⋯Cr(1) <sup>#5, e</sup>	7.272(2)	Cr(1)⋯Cr(1) <sup>#7, e</sup>	6.909(4)
Cr(1)⋯Cr(1) <sup>#6, e</sup>	7.272(2)	Cr(1)⋯Cr(1) <sup>#8, e</sup>	6.909(4)

Metal separation along to <sup>d</sup>// a-axis and <sup>e</sup>// b-axis. Symmetry codes: #1 x+1, y, z; #2 x-1, y, z; #3 1-x, -y, -z; #4 1-x, 1-y, -z; #5 -x, y+1/2, -z; #6 -x, y-1/2, -z; #7 x, y+1/2, -z+1/2; #8 x, y-1/2, -z+1/2.

Selected inter-network metal separations (Å).

	<i>racGN</i>
Mn(1)⋯Cr(1) <sup>#1</sup>	7.5376(11)
Mn(1)⋯Mn(1) <sup>#2</sup>	7.9749(12)
Mn(1)⋯Mn(1) <sup>#1</sup>	7.9749(12)
Mn(1)⋯Mn(1) <sup>#3</sup>	8.8875(10)
Mn(1)⋯Mn(1) <sup>#4</sup>	8.8875(10)
Cr(1)⋯Cr(1) <sup>#2</sup>	7.9749(11)
Cr(1)⋯Cr(1) <sup>#1</sup>	7.9749(11)
Cr(1)⋯Cr(1) <sup>#3</sup>	8.8875(9)
Cr(1)⋯Cr(1) <sup>#4</sup>	8.8875(9)

Symmetry codes: #1  $x, y, z-1$ ; #2  $x, y, z+1$ ; #3  $x+1, y, z+1$ ; #4  $x-1, y, z-1$ .

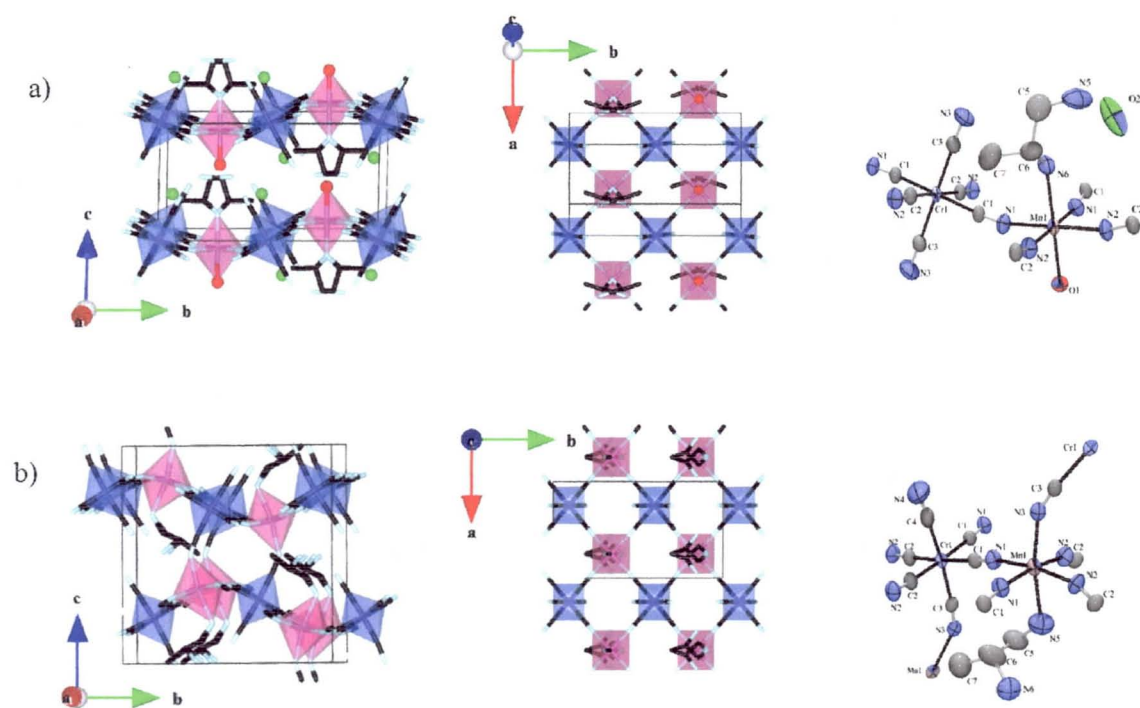


**Figure 4-1.** Projections of the structures along the *a*-axis (left), a view of the square grid layer of Mn (pink) and Cr (blue) atoms connected through cyanide (middle), and ORTEP drawing (right) for (a) *racGN*, and (b) *racGN-DP*. The two water molecules (red and green) are differentiated by the use of different colors.



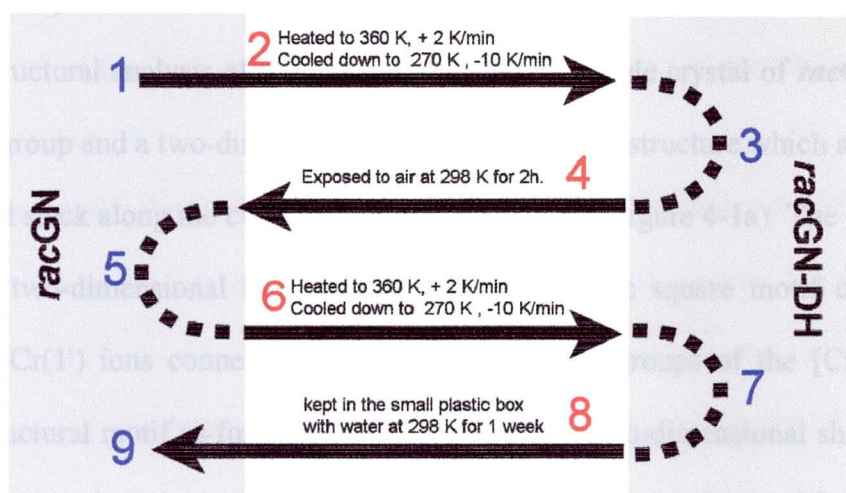


**Figure 4-2.** The protocol adopted for in-situ single crystal X-ray determinations.

Unlike the observations made for the **RGN-LTP** sample, where two well-defined transformations take place. The first at 315 K involving a first-order structural phase transition assisted by a proton-transfer where the amine is detached from one layer and attached to the neighbor layer through the other nitrogen in the place of the coordinated water molecules which then becomes uncoordinated while the non-coordinated water molecules takes the bonding place of the amine. The second transformation involves complete dehydration which is accompanied by the formation of further cyanide bridges resulting in a 3D-network. The crystals of **racGN** in contrast show only one transformation which involved both the amine movement from coordination of one nitrogen to the other and from layer to layer and the dehydration. The major structural differences are therefore the change of dimensionality and the coordination of the diamine. For the virgin phase (**racGN**) the crystal structure is similar to those of **RGN-LTP/SGN-LTP** having a two-dimensional Mn-Cr square-grid network and secondary amine nitrogen forms the Mn-N bond while the dehydrated phase (**racGN-DP**) has a three-dimensional crystal structure and Mn-N bond with primary amine nitrogen.

#### IV-3.1.1. Crystal structure of virgin *racGN*

X-ray structural analysis of the diffraction data on a single crystal of *racGN* suggests a  $P 2_1/m$  space-group and a two-dimensional corrugated layered structure which are parallel to the  $ab$ -plane and stack along the  $c$ -axis in an eclipsed manner (Figure 4-1a). The repeating unit of the anionic two-dimensional layer consists of a bimetallic square motif of Mn(1), Cr(1), Mn(1') and Cr(1') ions connected by equatorial cyanide groups of the  $[\text{Cr}(\text{CN})_6]^{3-}$  ion. A common structural motif as for *RGN-LTP* is seen in the two-dimensional sheet consisting of bimetallic square, but the structures differ in space-group and the stacking manner of the sheets. The space-group for *RGN-LTP/SGN-LTP* is  $P 2_12_12_1$ , and it is changed to  $P 2_1/m$  by use of racemic mixture of pn which introduces a mirror plane on Mn atom as well as an inversion center on Cr atom. In the crystal structure of *RGN-LTP/SGN-LTP* the two-dimensional sheets are stacked as [ABAB], where alternate layers are generated by the  $2_1$  axis along the  $c$ -axis. In contrast, for *racGN* the two-dimensional sheets are stacked in an eclipsed fashion on top of each other [AAAA], which consequently, halved the  $c$ -axis found in *RGN-LTP/SGN-LTP*.  $\beta$  angles are  $90^\circ$  (Orthorhombic) and  $110^\circ$  (Monoclinic) in *RGN-LTP/SGN-LTP* and *racGN*, respectively.

Mn ion exhibits octahedral geometry comprising nitrogen atoms of four  $[\text{Cr}(\text{CN})_6]^{3-}$  ion and pnH and oxygen of water molecules. Mn(1) has four bridging cyanide nitrogen atoms (N(1), N(2), N(1') and N(2')) in the equatorial positions, nitrogen atom N(6) from pn and oxygen atom O(1) from water molecule to complete its octahedral geometry. The Mn(1)-N(6) distance, 2.307(4) Å, is longer than the others (2.212(2) - 2.225(2) Å), describing octahedral geometry with one elongated bond. In contrast for *RGN-LTP*, the Mn(1)-N/O distances range from 2.202(3) to 2.235(2) Å and the N-Mn-N/O angles are in the range of 83.79(10) to 95.45(10) ° for cis positions. The octahedral geometry of Mn(1) for *racGN* appears to be more distorted than *RGN-LTP*. The Mn-N-C and Cr-C-N bond angles within the layer range from 162.9(2) - 166.4(2)° and 177.2(2) - 177.4(2)° respectively for *racGN*. For the *RGN-LTP*,

the former range was wider, 152.0(3) - 177.8(3)° but the latter is similar, 176.2(3) - 177.8(4)°, respectively. Thus the corrugation of the two-dimensional layer of *rac*GN is less pronounced than that of *RGN-LTP*.

In the two-dimensional sheet, the average separations between the Mn and Cr atoms through CN bridge is 5.3729(11) Å for *rac*GN, which is slightly longer than that for *RGN-LTP* (5.3457(16) Å). The shortest intersheet metal-metal separation for *rac*GN is observed between the Mn and Cr atoms (7.5376(11) Å), while the shortest intersheet homometallic contacts are longer than 7.9 Å (7.9749(11) Å). From the viewpoint of the magnetic dipole interaction, a distance of less than 10 Å describes a ferromagnetic interaction between two-dimensional sheets, which is the same situation as for the *RGN-LTP* compound.

Between two-dimensional sheets, the nitrogen atom N(5) in non-coordinating amine is found to have one hydrogen bond with the oxygen atoms of crystal water (N(5)⋯O(2), 2.781(11) Å) molecules, but not with the oxygen atom of coordinating water (N(5)⋯O(1'), 3.903(9) Å) which is found in *RGN-LTP* (2.835(6) Å). The oxygen atom O(1) of coordinating water is found to have two hydrogen bonds between nitrogen of cyanide group in neighboring layer (O(1)⋯N(3'), 2.785(3) Å). One hydrogen bond is generated by mirror symmetry from the other.

The crystal structure analysis described above revealed a statistical disorder of the diamine ligand on two equivalent crystallographic positions where one is occupied the *S*-enantiomer and the other by the *R*-enantiomer. Within this model there is a common atom (N6) which has full occupancy and all the other atoms are on half occupancies. N6 is also the one coordinated to the Mn atom. The structure was resolved within the achiral space-group *P* 2<sub>1</sub>/m. We therefore tested the possibility of finding solutions where the two enantiomers are fully ordered or the compound contains either of the two enantiomers by spontaneous resolution upon crystallization. Search for a doubled unit cell was only successful for a x 2b x c but attempt to do full structure refinement resulted in locating only the metal ions. Given

that the extinctions are similar for both  $P2_1$  and  $P 2_1/m$ , we attempted several models using the former. When the crystal structure was solved as enantiopure *R*- and *S*-isomer, the flack parameters were 2.2% and 15.6%, respectively. However, unusual bond lengths, C6-C7 (1.786 Å) and C5-N5 (1.310 Å), were observed. Then, the crystal structure was refined using both isomers but as adjustable quantity an acceptable refinement was obtained for  $R : S = 53 : 47$ . For all other trials refinement, none of them converged during refinement. These results indicate the presence of statistical disorder of the two enantiomers in crystal structure.

#### IV-3.1.2. Crystal structure of *rac*GN-DP

The crystal structure of dehydrated *rac*GN-DP was obtained from in-situ measurement. The same single crystal used above was heated to 360 K and cooled down to 298 K for structural measurement. All procedures were done in a nitrogen stream. The X-ray structural analysis on dehydrated *rac*GN-DP found the  $P mnb$  space-group and a three-dimensional crystal structure (Figure 4-1b). The two-dimensional sheets in the *ab*-plane stack in a staggered fashion along the *c*-axis as a consequence of a sliding of the corrugated sheets to introduce the new cyano bridges between the sheets. These new connections change the crystal system and also the symmetry. In the virgin phase, the mirror plane is perpendicular to the *b*-axis and the Cr ion is on an inversion center, whereas in the dehydrated phase, the mirror planes are perpendicular to the *a*-axis and the Cr ion is on the mirror plane, and *n* glide symmetry is introduced.

After dehydration, the coordinating oxygen atom O(1) (*rac*GN) is replaced by the nitrogen atom N(3) in bridging cyanide group. The Mn ion exhibits distorted octahedral geometry comprising atoms of five  $[\text{Cr}(\text{CN})_6]^{3-}$  ions and nitrogen of pnH. Mn(1) has four bridging cyanide nitrogen atoms (N(1), N(2), N(1') and N(2')) in equatorial positions, nitrogen atom N(5) from pn and nitrogen atom N(3) of bridging cyanide to complete its octahedral geometry. It should be noted that coordination of the diamine is switched after dehydration,

being Mn-N(6) in *racGN* to Mn-N(5) in *racGN-DP*. This change suggests the existence of structural phase transition which changes coordination nitrogen atom as observed for *RGN-LTP*.

The Mn(1)-N(3) and Mn(1)-N(5) distances are 2.258(6) and 2.437(9) Å which are longer than the others (2.191(4) - 2.217(4) Å), describing an axially elongated octahedral geometry and suggests that dehydrated *racGN-DP* has a more distorted Mn octahedron than *racGN*. In the cyanide network, the observed minimum Mn-N-C and Cr-C-N angles of dehydrated *racGN-DP* is 147.5(5) and 172.8(6), respectively, which are smaller than those of *racGN* (162.9(2), 177.2(2)°). Heterometal separations linked by one cyanide group for the dehydrated *racGN-DP* have shorter distance (5.201(3), 5.430(2) Å) than that for the *racGN* (5.3814(8), 5.3644(8) Å). The disorder of the diamine is also present in the structure of *racGN-DP*. However, there are now two common atoms, the coordinating nitrogen N(5) and the methyl carbon.

#### IV-3.2. Thermogravimetric analyses

The TG measurements of samples consisting of powdered crystals of *racGN* under nitrogen atmosphere show a first weight loss starting at 340 K to a stable state up to 450 K where they decompose (Figure 4-3). The observed percentage weight loss (9.6%) is in good agreement with the departure of two water molecules per formula unit (9.63%).

On lowering the temperature of the samples having been heated only to 370 K under nitrogen the weight gain is minimal. Interestingly, upon exposure of the samples to air (humidity  $\approx$  50%) at ambient temperature ca. 290 K for  $\approx$  7 hours, they re-absorb water and recover their initial weights, which we label as dehydrated *racGN-DP* to hydrated *racGN-HP*. These processes are reversible and have been performed four times consecutively.

As mentioned in the part of *racGN-DP* crystal structure, it is expected to have two endothermic peaks in DTA curve during dehydration. However, only one peak can be seen,

indicating that structural phase transition and dehydration occurs at the same time and the small peak from structural phase transition is covered by large peak from dehydration.

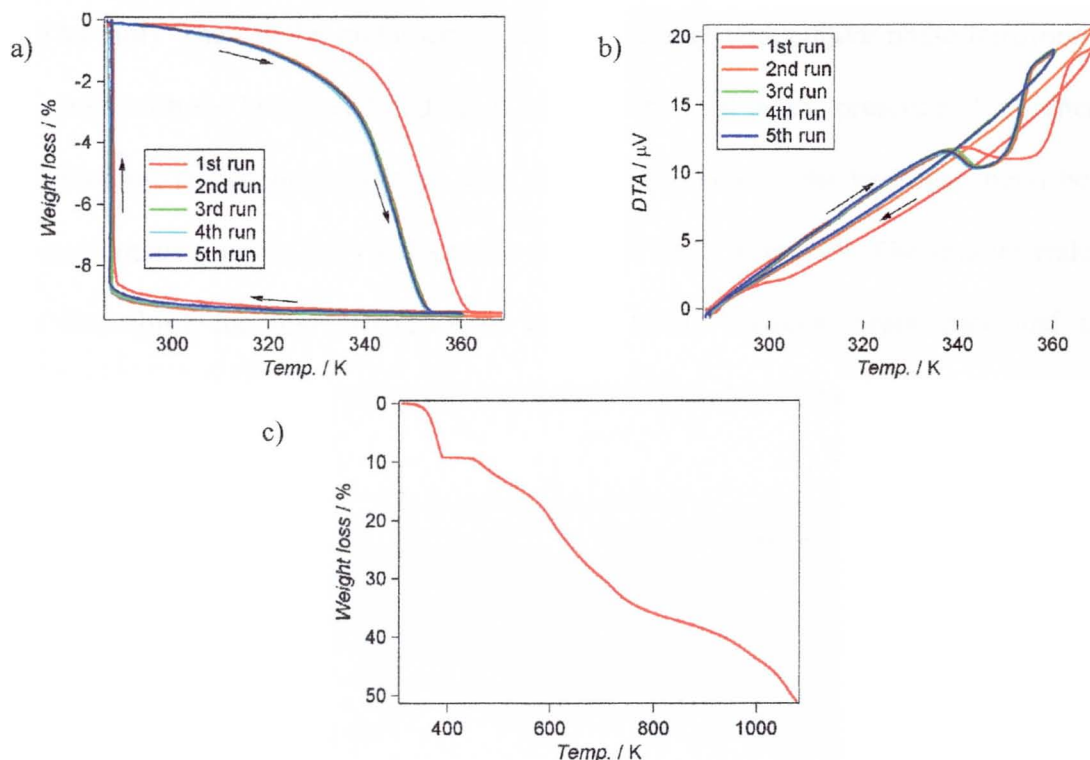


**Figure 4-3.** (a) Thermogravimetric and (b) DTA for *racGN* for several cycles of dehydration and rehydration in the low temperature region, and (c) TGA for the high temperature region.

### IV-3.3. Differential scanning calorimetry

The result from the crystal structure determinations is that there is a possibility that a transformation from a low temperature phase to a high temperature phase may be present as found for *RGN-LTP* which is then followed by the dehydration. For *RGN-LTP* the two processes are well separated by 50 K and in the case of *racGN* the two may be close in temperature. To search for the structural phase transformation, we performed differential calorimetry on powdered samples of *racGN*.

The powdered sample was sealed in aluminum pan with lid to shift the dehydration process to higher temperatures (Figure 4-4). The DSC curve showed a large endothermic peak

from 360 K with small peak around 370 K. This peak might be from the structural phase transition found at 310 K for **RGN-LTP**. The integration of this peak estimates to be 1.16 kJ/mol (0.277 kcal/mol) which is approximately one third of the absorption in **RGN-LTP** (3.45 kJ/mol). The smaller endothermic peak and higher temperature phase transition may be associated with the hydrogen bonding. It can be explained by the presence of a higher barrier for a proton-transfer mechanism to take place due to lack of the hydrogen bond between a non-coordinating amine N(5) and a water molecule O(1') in **racGN**. The smaller endothermic peak describing the less difference of energy levels between virgin state and the high temperature phase that first amine of *rac*-pn associates to Mn-N bond.

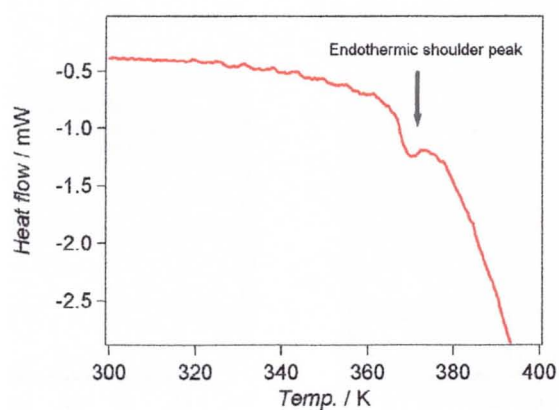


**Figure 4-4.** DSC curves for *racGN*.

#### **IV-3.4. Powder X-ray diffraction**

To verify the structural change by dehydration and hydration, powder X-ray diffraction for each phase was collected by in-situ measurement (Figure 4-5). Diffraction data for virgin sample of *racGN* was collected on the glass plate. The same experiment for **racGN-DP** was performed after the sample had been dehydrated for 10 min at 360 K, then the sample was exposed to air for 30 min to measure **racGN-HP**, and dehydrated for 10 min at 360 K again to measure **racGN-DP** (2nd). The results are shown in figure 4-6 with diffraction pattern using the single-crystal data.

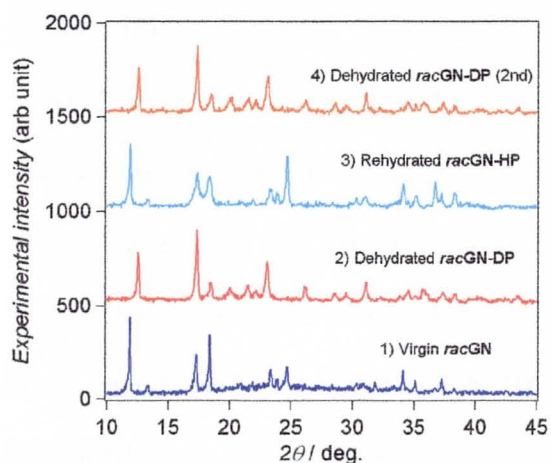


**Figure 4-5.** Experimental XRPD patterns for virgin *racGN*, dehydrated *racGN-DP*, rehydrated *racGN-HP*, and *racGN-DP* (2nd) which is dehydrated sample of *racGN-HP*. (Cu  $K\alpha$ ).

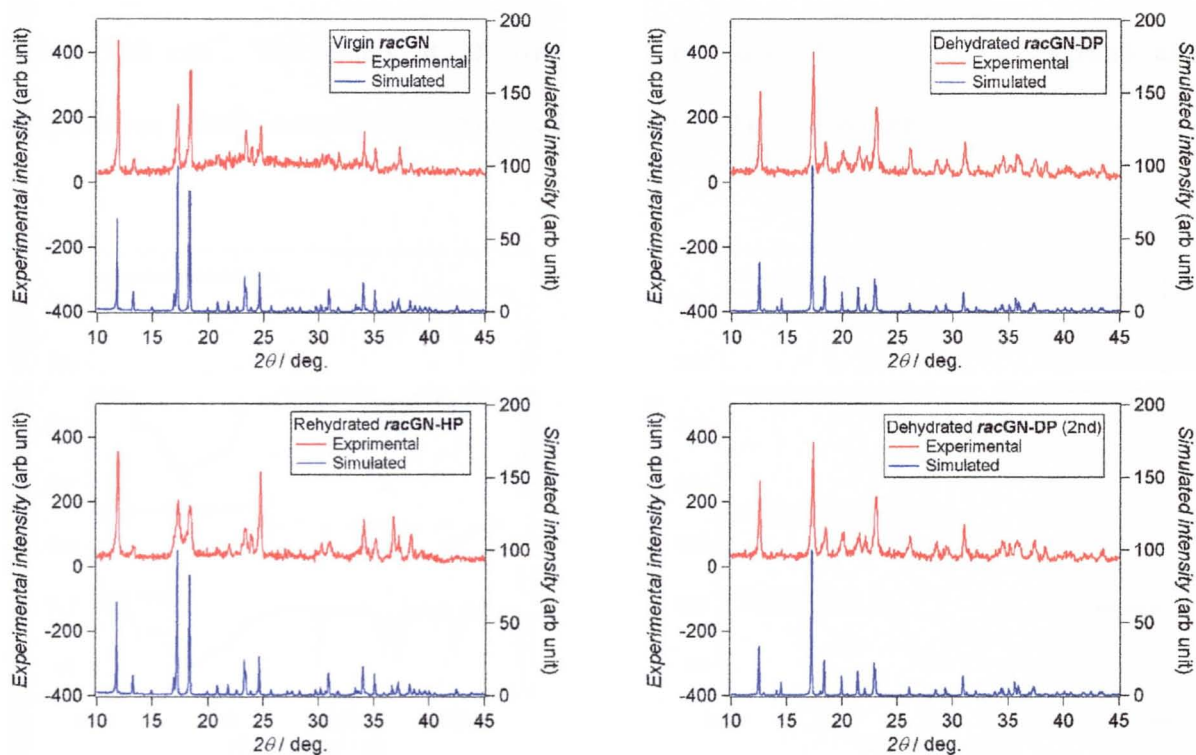


**Figure 4-6.** Experimental and simulated XRPD patterns for *racGN*, *racGN-DP*, *racGN-HP*, and *racGN-DP* (2nd). (Cu  $K\alpha$ ). For the hydrated *racGN-HP*, the crystallographic data of virgin *racGN* was used for the simulation.



#### IV-3.5. Infrared spectroscopy

Infrared spectra of *racGN*, dehydrated *racGN-DP*, rehydrated *racGN-HP*, and its dehydrated *racGN-DP*(2nd) are shown in figure 4-7. In the spectra, bands associated to H<sub>2</sub>O, pn and CN can be identified (Table 4-3). The OH and NH stretching modes are observed above 3000 cm<sup>-1</sup>. The CN stretching modes are observed in the range 2200 - 2100 cm<sup>-1</sup>. The presence of two such peaks in *racGN*, and rehydrated *racGN-HP* may be due to bridging and terminal cyano groups. Meanwhile only one broad peak can be seen for dehydrated phases. It might be from mixture of four crystallographically independent cyano groups. The bending modes of H<sub>2</sub>O and amine group in pn are seen at 1680 and 1600-1580 cm<sup>-1</sup>, respectively. The bending mode of C-H, stretching mode of C-N, and bending mode of N-H are seen 1520 - 1400, 1200 - 980, 920 - 790 cm<sup>-1</sup>, respectively. The M-O and M-N bond stretch modes appear below 530 cm<sup>-1</sup>. The peaks at 3631(m), 3543(m), and 1678(w) cm<sup>-1</sup> disappears after dehydration, which is consistent with the assignment for H<sub>2</sub>O molecules.

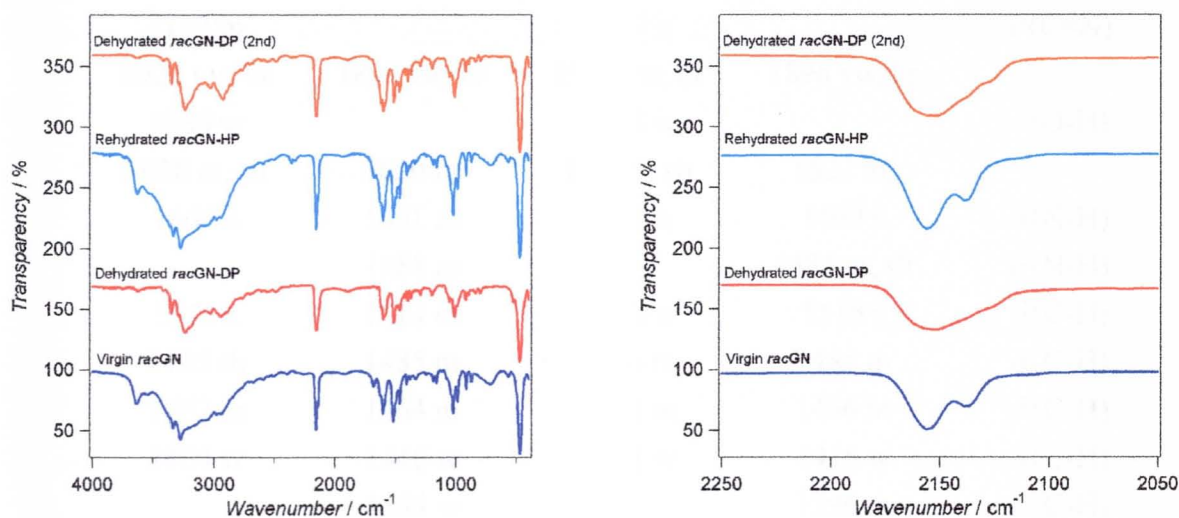


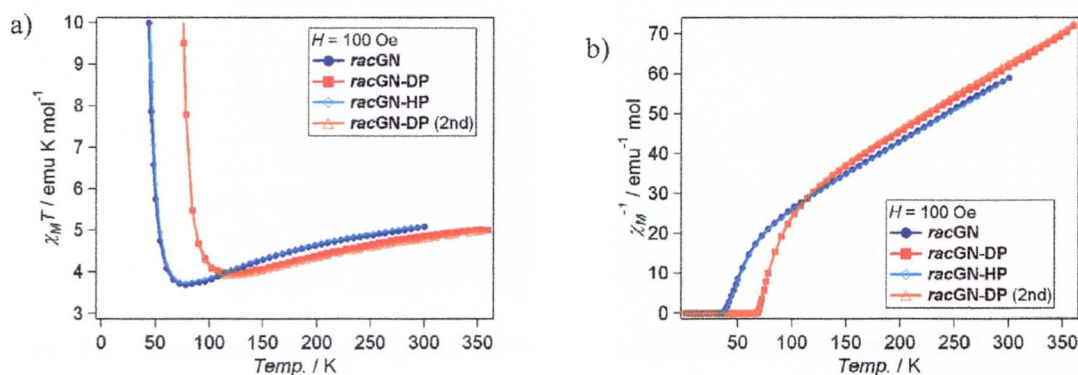
Figure 4-7. Infrared transmission spectra for *racGN*, *racGN-DP*, *racGN-HP*, and *racGN-DP* (2nd).

**Table 4-3.** Frequencies and assignments of the bands in the spectra of *racGN*, *racGN-DP*, *racGN-HP*, and *racGN-DP* (2nd).

<i>racGN</i>	<i>racGN-DP</i>	<i>racGN-HP</i>	<i>racGN-DP</i> (2nd)	
3631 m		3627 m		$\nu(\text{O-H})$
3543 m		3533 m, sh		$\nu(\text{O-H})$
	3413 vw		3413 vw	$\nu(\text{N-H})$
3336 s	3348 m	3336 s	3348 m	$\nu(\text{N-H})$
3274 s	3294 m	3273 s	3294 m	$\nu(\text{N-H})$
	3238 s		3240 s	$\nu(\text{N-H})$
3062 s, br	3030 m	3062 s, br	3030 m	$\nu(\text{C-H})$
2981 s		2981 s		$\nu(\text{C-H})$
2941 s	2940 m	2941 s	2926 m	$\nu(\text{C-H})$
	2767 w		2769 w	
2702 w	2704 w	2706 w	2704 w	
2673 w	2676 w	2675 w	2679 w	
2592 w	2603 w	2596 w	2605 vw	
	2555 vw		2553 vw	
2503 w	2484 vw	2505 vw	2486 vw	
2156 s	2152 s, br	2156 s	2152 s, br	$\nu(\text{C}\equiv\text{N})$
2137 m		2139 s		$\nu(\text{C}\equiv\text{N})$
1924 vw, br	1890 vw, br	1928 vw, br	1896 vw, br	
1680 w		1678 w		$\delta(\text{O-H})$
1628 m, sh	1620 m	1630 s, sh	1622 m,	
1603 s	1601 m	1603 s	1600 s	$\delta(\text{N-H})$
	1581 m		1581 m, sh	$\delta(\text{N-H})$
1518 s	1514 m	1520 s	1516 s	$\delta(\text{C-H})$
1495 sh	1485 m	1496 m	1485 m	$\delta(\text{C-H})$
1462 m	1464 m	1462 m	1466 m	$\delta(\text{C-H})$
1404 w	1416 w	1404 w	1416 w	$\delta(\text{C-H})$
	1394 w		1396 m	$\delta(\text{C-H})$
1377 w	1371 w	1379 w	1371 w	
1338 w		1339 w		
1323 w	1292 w	1325 w	1294 w	
1244 vw		1244 vw		
1186 w	1196 w	1186 w	1196 w	$\nu(\text{C-N})$
1161 w		1161 w		$\nu(\text{C-N})$

	1053 w		1053 w	$\nu(\text{C-N})$
1022 s	1010 m	1024 s	1010 m	$\nu(\text{C-N})$
985 m	987 w	985 m	987 w	$\nu(\text{C-N})$
914 m	916 w	915 w	918 w	$\delta(\text{N-H})$
874 m	897 w	874 w	897 w	$\delta(\text{N-H})$
	837 w		837 vw	$\delta(\text{N-H})$
	798 w		798 vw	$\delta(\text{N-H})$
714 w, br		715 w, br		
569 vw	524 w	567 w	524 w	
470 vs	474 vs	474 vs	474 vs	$\nu(\text{Cr-C})$

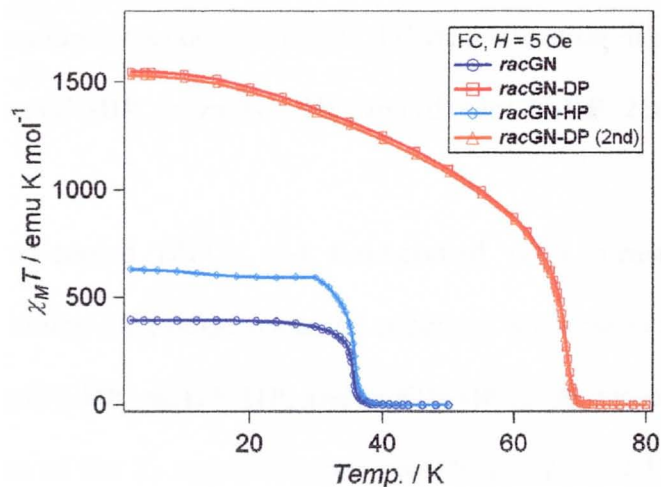
#### IV-3.6. Magnetic properties



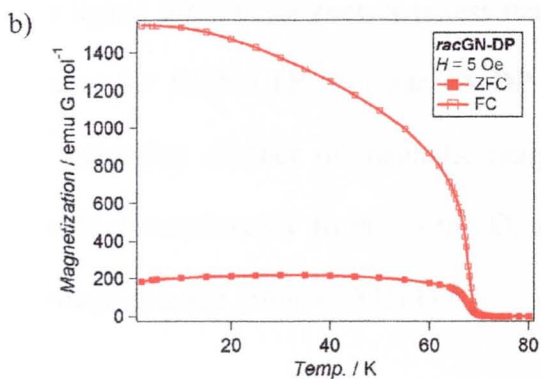
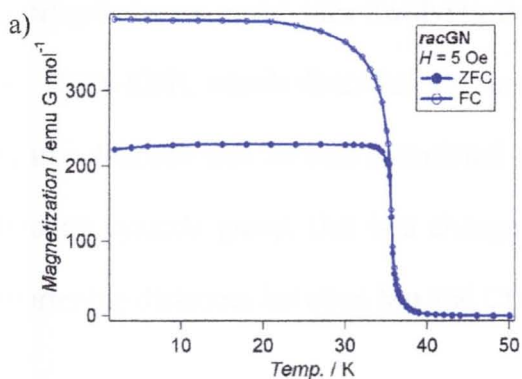
**Figure 4-8.** Temperature dependence of (a)  $\chi_M T$  and (b)  $\chi_M^{-1}$  in an applied field of 100 Oe for virgin *racGN*, dehydrated *racGN-DP*, rehydrated *racGN-HP*, and *racGN-DP* (2nd) which is dehydrated sample of *racGN-HP*.

The temperature dependence of  $\chi_M T$  for virgin *racGN*, dehydrated *racGN-DP*, rehydrated *racGN-HP*, and *racGN-DP* (2nd) in a field of 100 Oe are displayed in figure 4-8a. The  $\chi_M T$  values are 5.09, 4.86, 5.10 and 4.78 emu K mol<sup>-1</sup> at 300 K, and decrease with lowering temperature down to a minimum value of 3.69 (78 K), 3.96 (120 K), 3.72 (78 K), and 3.91 emu K mol<sup>-1</sup> (114 K), respectively. Upon further cooling, the  $\chi_M T$  values increase to maximum values of 921 (31 K), 1830 (52 K), 1212 (30 K), and 1990 (52 K) emu K mol<sup>-1</sup> before decreasing below this temperature, respectively. The  $\chi_M^{-1}$  value for each phase follows the Curie-Weiss law ( $\chi_M = C / (T - \theta)$ ) with Weiss constant  $\theta$  of -65.7, -80.3, -65.4 and -83.0 K

and Curie constant  $C$  of 6.17, 6.16, 6.20, and 6.11  $\text{emu K mol}^{-1}$ , respectively (Figure 4-8b). These Curie constants are comparable to the theoretical value (for  $\text{Mn(II)}$  and  $\text{Cr(III)}$ ):  $1/2 \times 5/2 \times 7/2 + 1/2 \times 3/2 \times 5/2 = 6.25 \text{ emu K mol}^{-1}$ ). The negative Weiss constants indicate considerable antiferromagnetic interaction between  $\text{Cr}^{\text{III}}$  ion and  $\text{Mn}^{\text{II}}$  ions through the cyanide bridge.



**Figure 4-9.** Temperature dependence of FC magnetization in an applied field of 5 Oe for *racGN*, *racGN-DP*, *racGN-HP*, and *racGN-DP (2nd)*.



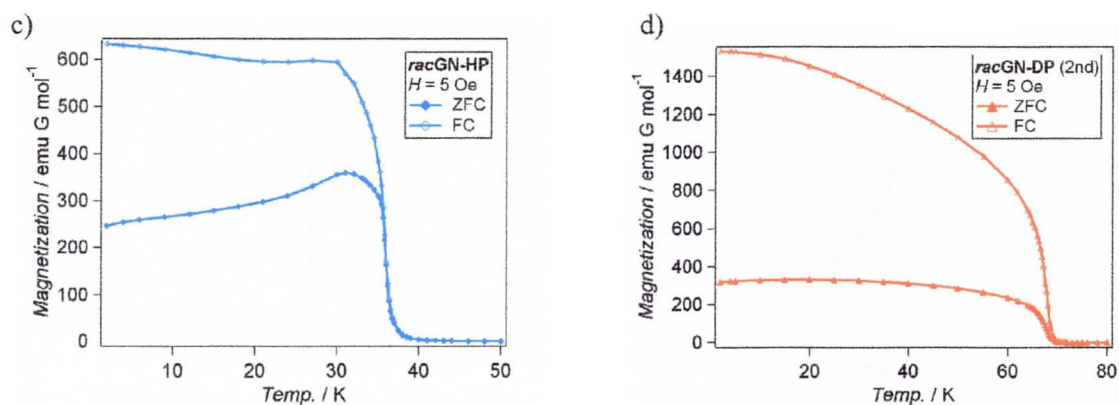


**Figure 4-10.** Temperature dependence of ZFC, FC magnetization in an applied field of 5 Oe for (a) *racGN*, (b) *racGN-DP*, (c) *racGN-HP*, and (d) *racGN-DP (2nd)*.

In the zero-field-cooled (ZFC) and field-cooled (FC) measurements, spontaneous magnetization confirming long-range magnetic orderings are observed below 36, 70, 36 and 70 K for *racGN*, *racGN-DP*, *racGN-HP*, and *racGN-DP (2nd)*, respectively (Figure 4-9, 10). The small difference of the  $T_C$  value between *racGN* and *RGN-LTP* can be explained by exchange interaction due to slight structural differences within the layer. For *RGN-LTP*, the average metal separations between Mn and Cr atom in the two-dimensional sheets for *RGN-LTP* (5.3457(16) Å) is longer than that for *racGN* (5.3729(11) Å). Therefore, molecular overlap between metal sites involving the cyanide ligand orbitals for *racGN* is less than that for *RGN-LTP*, which describes the lower  $T_C$  value for *RGN-LTP*. For *racGN-DP*  $T_C$  is nearly doubled due to two associated changes; increasing number of magnetic neighbors through cyanide group, that is a change of magnetic dimensionality from 2D to 3D, and to shortening distances between Mn and Cr atoms through cyanide group (5.323(4) Å).

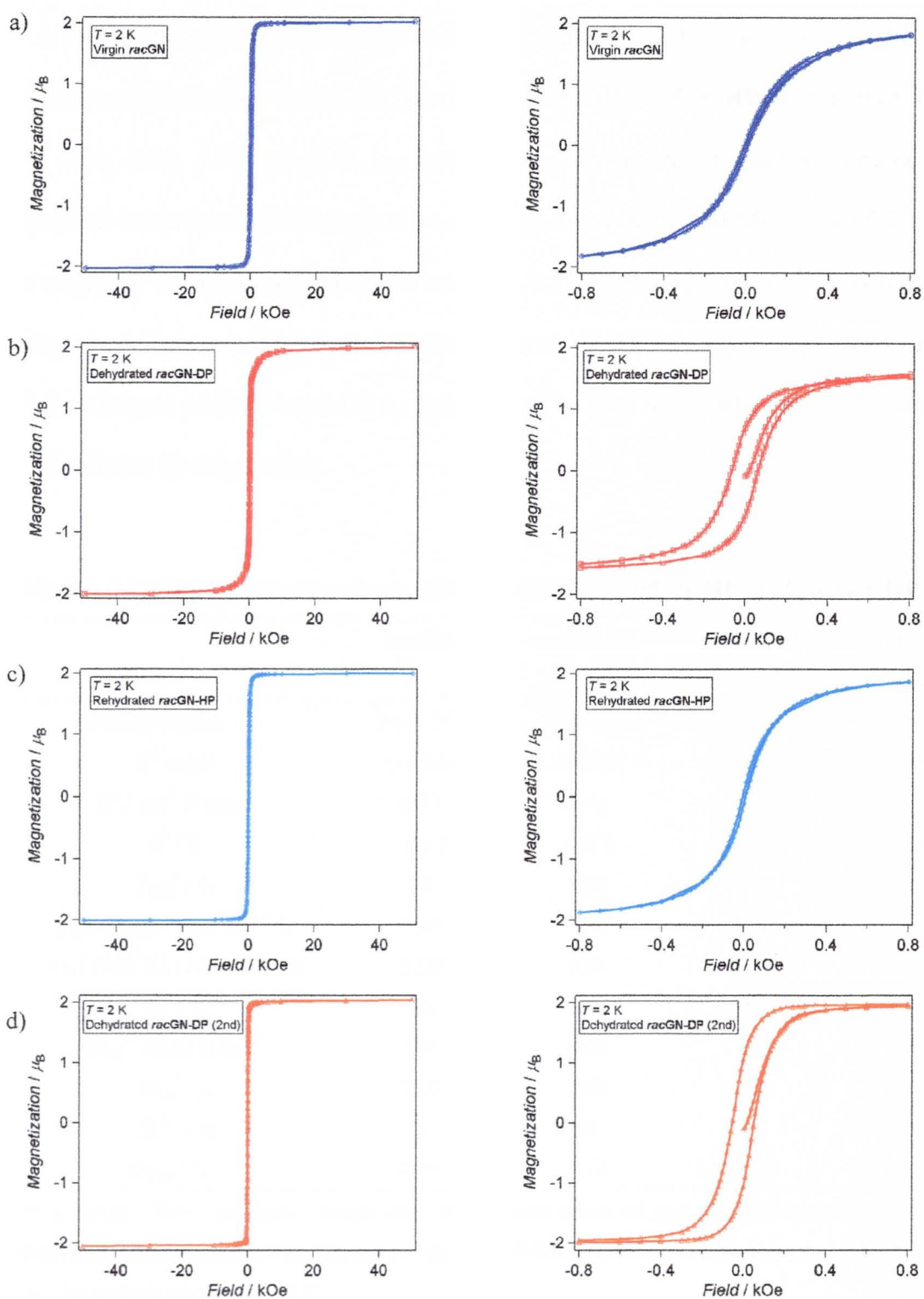


Figure 4-11. Field dependence of the magnetization at 2 K for (a) *racGN*, (b) *racGN-DP*, (c) *racGN-HP*, and (d) *racGN-DP* (2nd).

A hysteresis loop for each compound was observed at 2 K (Figure 4-11). The observed saturation magnetization values for *racGN*, *racGN-DP*, *racGN-HP*, and *racGN-DP* (2nd) were 2.03, 2.00, 1.99 and 2.05  $\mu_B$ , respectively, which are in good agreement with the theoretical value for antiferromagnetic coupling between  $Cr^{3+}$  and  $Mn^{2+}$  ions ( $5/2 - 3/2 = 1$ ). The observed remanant magnetization are 0.07, 0.71, 0.10, and 1.06  $\mu_B$  and coercive field in the hysteresis loop are 8, 63, 6, and 53 Oe, respectively. These values suggest that *racGN* is a soft ferrimagnet while it becomes a slightly hard magnet upon dehydration and recover the initial softness by rehydration.

**Table 4-4.** Magnetic parameters for *racGN*, *racGN-DP*, *racGN-HP*, and *racGN-DP* (2nd).


	<i>racGN</i>	<i>racGN-DP</i>	<i>racGN-HP</i>	<i>racGN-DP</i> (2nd)
<i>Fitting region / K</i>	300 - 114	360 - 168	300 - 114	360 - 168
<i>R</i> <sup>2</sup> <i>value</i>	0.9999	0.9999	0.9999	0.9997
<i>C</i> <sup>a</sup> / cm <sup>3</sup> K mol <sup>-1</sup>	6.17	6.16	6.20	6.11
$\theta$ <sup>b</sup> / K	- 65.7	- 80.3	- 65.4	- 83.0
<i>T</i> <sub>min</sub> <sup>c</sup> / K	78	120	78	114
$\chi_M T$ ( <i>T</i> <sub>min</sub> ) / emu mol <sup>-1</sup> K	3.69	3.96	3.72	3.91
$\chi_M T$ (300 K) / emu mol <sup>-1</sup> K	5.09	4.86	5.10	4.78
<i>T</i> <sub>C</sub> <sup>d</sup> / K	36	70	36	70
<i>M</i> <sub>2 K</sub> <sup>e</sup> / emu G mol <sup>-1</sup>	396	1550	633	1530
<i>M</i> <sub>sat</sub> <sup>f</sup> / $\mu_B$	2.03	2.00	1.99	2.05
<i>H</i> <sub>C</sub> <sup>g</sup> / Oe	8	63	6	53
<i>M</i> <sub>REM</sub> <sup>h</sup> / $\mu_B$	0.07	0.71	0.10	1.06


<sup>a</sup>Curie constants. <sup>b</sup>Weiss constants. <sup>c</sup>Temperatures at minimum values of  $\chi_M T$ . <sup>d</sup>Critical temperatures based on FC measurements. <sup>e</sup>Magnetization at 2 K in FC measurement ( $H = 5$  Oe). <sup>f</sup>Magnetization saturation value at 2 K. <sup>g</sup>Coercive field at 2 K. <sup>h</sup>Remanant magnetization at 2 K.


#### IV-4. Conclusion

In summary, the achiral two-dimensional  $[\text{Mn}(\text{rac-pnH})(\text{H}_2\text{O})][\text{Cr}(\text{CN})_6]\cdot\text{H}_2\text{O}$  (*racGN*) was successfully synthesized by the use of racemic pn. The magnetic properties of this compound correspond to those of a soft ferrimagnet below 36 K. Comparing to *RGN-LTP/SGN-LTP*, common features are seen in crystal structure, ferrimagnetic behavior in two-dimensional sheet, ferromagnetic interaction between sheets, and softness of the magnet. These results indicate that *racGN* is a good reference to the chiral magnet (*RGN-LTP/SGN-LTP*). Further physical measurements will be undertaken to elucidate the sole effect of chirality by the use of both compounds. Moreover reversible dehydration is demonstrated on *racGN*. As a result of the dehydration, crystal structure is changed to three-dimensional crystal structure with new cyanide bridging as well as  $T_C$  is doubled to 70 K, and coercive field at 2 K is increased from 8 to 63 Oe.

#### Movies of transformation processes.

Movie 4-1 : 2 Movie dehydration from *racGN* to *racGN-DH* 

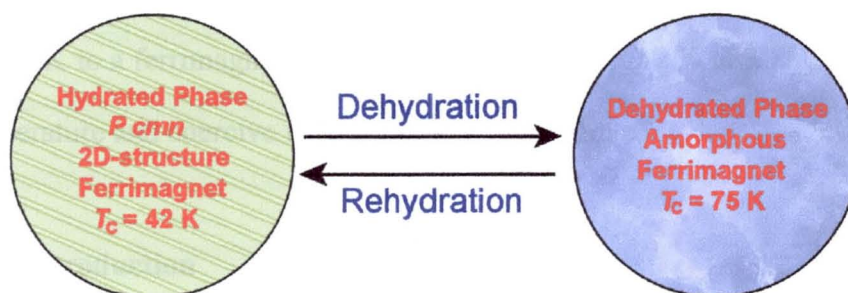
Movie 4-2 : 4 Movie rehydration from *racGN-DH* to *racGN* 

Movie 4-3 : 6 Movie debhydration from *racGN* to *racGN-DH* 



## Chapter V

### **[Mn(enH)(H<sub>2</sub>O)][Cr(CN)<sub>6</sub>]·H<sub>2</sub>O : Reversibility of Single Crystal-to-Amorphous Dehydrated Phase and Associated Increment-Decrement of Curie Temperature and Magnetic Hardness**



## Chapter V

### **[Mn(enH)(H<sub>2</sub>O)][Cr(CN)<sub>6</sub>]·H<sub>2</sub>O : Reversibility of Single Crystal-to-Amorphous Dehydrated Phase and Associated Increment-Decrement of Curie Temperature and Magnetic Hardness**

#### **V-1. Abstract**

We report the synthesis, crystal structure and magnetic properties of the two-dimensional achiral soft-ferrimagnet [Mn(enH)(H<sub>2</sub>O)][Cr(CN)<sub>6</sub>]·H<sub>2</sub>O (**enGN**) as a comparison to the well-investigated two-dimensional chiral enantiopure ferrimagnets [Mn(*R/S*-pnH)(H<sub>2</sub>O)][Cr(CN)<sub>6</sub>]·H<sub>2</sub>O (**RGN-LTP/SGN-LTP**). **enGN** crystallizes in the orthorhombic achiral *P* *cmn* space-group having a two-dimensional square-network of Mn-Cr with bridging cyanide, and behaves as a soft ferrimagnet below 42 K. **enGN** shows reversible single crystal-to-amorphous dehydrated phase, **enGN-DP**. **enGN-DP** exhibits long-range ordering at 75 K to a ferrimagnetic state and coercive field at 2 K of 100 Oe which are higher critical temperature and coercive field than the virgin sample.

#### **V-2. Introduction**

The considerable efforts that are being devoted in designing magnetic materials based on molecules or molecular assemblies using organic linkers have resulted a whole gamut of materials exhibiting long-range magnetic ordering at finite temperatures. In addition to the very wide range of Curie temperatures, based in ferromagnetism, ferrimagnetism and canted-antiferromagnetism, several improvement of other parameters such as coercivity field and remanant magnetization, have been realized. Furthermore, the introduction of other properties such as optical or electrical has been successful and responsive coupling of the two is being observed. This growing interest in exploring multifunctional magnetic organic-inorganic hybrid materials now includes the combination of magnetism and electrical

properties,<sup>9</sup> optical properties,<sup>26,27</sup> photoreactivity,<sup>7</sup> guest sensitivity,<sup>8</sup> and chirality.<sup>14-18</sup> Along this line we have been searching for chiral magnets and in particular to look for new physical phenomenon and to understand the relation between structural chirality and magnetic chirality and how they are coupled. Experimental observations of the magneto-chiral dichroism have been observed and recently<sup>11</sup> we have observed other magnetic anomalies which are related to magnetic chirality. A theoretical study of these effects points to the orbital and spin coupling via a Dzyaloshinski coupling mechanism as for weak ferromagnetism.<sup>12</sup>

In this context, chirality and porosity with magnetism is of special interest. The chiral magnet  $[\text{Mn}(\text{S-pnH})(\text{H}_2\text{O})][\text{Cr}(\text{CN})_6]\cdot\text{H}_2\text{O}$  (**SGN-LTP**) was reported by our group employing the simplest chiral diamine molecule in 2003.<sup>15</sup> This compound belongs to the orthorhombic chiral space-group  $P 2_12_12_1$  and it has two-dimensional network structure. Below the Curie temperature ( $T_C = 38$  K) the saturation magnetization is  $2 \mu_B$ , due to antiferromagnetic ordering of  $\text{Cr}^{3+}$  ( $S = 3/2$ ) and  $\text{Mn}^{2+}$  ( $S = 5/2$ ) ions. Although, these measurements have been done only with chiral compound **RGN-LTP/SGN-LTP**, a test of this conclusion is crucial. We therefore have explored the use of ethylenediamine in the place of diaminopropane to produce an achiral system for comparison.

Here, we report the synthesis, single-crystal structure determinations of different forms, thermogravimetric analyses, optical spectroscopy and the magnetic properties of an achiral magnet  $[\text{Mn}(\text{enH})(\text{H}_2\text{O})][\text{Cr}(\text{CN})_6]\cdot\text{H}_2\text{O}$  as a reference of chiral magnet **RGN-LTP/SGN-LTP** and demonstrate the reversible dehydration as well as the associated changes in the magnetic properties.

### V-3. Results and discussion

#### V-3.1. Crystal structures

We recently observed reversible single crystal-to-single crystal transformation associated with a structural phase transition and dehydration of  $[\text{Mn}(\text{R-pnH})(\text{H}_2\text{O})][\text{Cr}(\text{CN})_6]\cdot\text{H}_2\text{O}$  (**RGN-LTP**). These results motivated us to investigate other stable ground states as a function of the temperature. A similar in-situ crystal structure study was undertaken starting from a virgin crystal for **enGN**. When the crystal was heated to 360 K, the diffraction spots disappeared (see movie 5-1), indicating dehydration results in an amorphous phase. However, when the crystal was exposed to the air, after the trial of the structural analysis of the dehydrated phase, the diffraction spots were recovered (see movie 5-2) enough to realize the same crystal structure as the virgin sample.

**Table 5-1.** Crystallographic data for virgin enGN and rehydrated enGN-HP.

Compound	Virgin enGN	Rehydrated enGN-HP <sup>a</sup>
formula	C9H13CrMnN8O2	C9H13CrMnN8O2
fw	360.20	360.20
<i>T</i> , K	298	298
atmosphere	Air	Air
exposure time, sec	10	20
no. of frames	830	830
crystal system	Orthorhombic	Orthorhombic
space-group	<i>P</i> cmn <sup>c</sup>	<i>P</i> cmn <sup>c</sup>
<i>a</i> , Å	7.5177(8)	7.5298(9)
<i>b</i> , Å	14.6493(15)	14.6804(19)
<i>c</i> , Å	14.9539(15)	14.9760(19)
<i>V</i> , Å <sup>3</sup>	1646.9(3)	1655.5(4)
<i>Z</i>	4	4
<i>D</i> <sub>C</sub> , g/cm <sup>3</sup>	1.453	1.445
$\mu$ (Mo K $\alpha$ ), mm <sup>-1</sup>	1.438	1.431
crystal size, mm <sup>3</sup>	0.6 x 0.2 x 0.1	0.6 x 0.2 x 0.1
<i>T</i> <sub>min</sub> and <i>T</i> <sub>max</sub>	0.5316, 1.0000	0.7784, 1.0000
$\theta$ <sub>min</sub> and $\theta$ <sub>max</sub> , deg	2.710, 27.839	3.028, 27.96
total no. of reflections	6353	6009
no. of unique reflections ( <i>R</i> <sub>int</sub> )	1950	1913
no. of observed [ <i>I</i> ≥ 2σ( <i>I</i> )]	1617	1336
no. of parameters	117	116
R1 / wR2 [ <i>I</i> ≥ 2σ( <i>I</i> )]	0.0395, 0.1263	0.0414, 0.1182
R1 / wR2 (all data)	0.0458, 0.1322	0.0605, 0.1297
GOF	1.075	1.001
$\Delta\rho^b$ e/Å <sup>3</sup>	-0.525, 0.573	-0.289, 1.166

<sup>a</sup>Diffraction data were collected after virgin enGN was heated to 360 K at a rate of 2 K/min and cooled down to 298 K at a rate of -10 K/min, then intensity data for the amorphous phase were collected, followed by the exposure of the crystal to air for 1.5 hour. <sup>b</sup>Maximum and minimum residual electron densities. <sup>c</sup> This space-group is the same symmetry as *P* nma (No. 62) which is employed for uniform definition of the axes for the RGN series.

**Table 5-2.** Selected bond distances, angles and metal separations for virgin enGN.

## Selected bond distances (Å) for octahedral geometries for Mn and Cr.

Mn(1)-N(1)	2.198(2)	Cr(1)-C(1)	2.063(2)
Mn(1)-N(2)	2.212(2)	Cr(1)-C(2)	2.066(2)
Mn(1)-N(4)	2.303(3)	Cr(1)-C(3)	2.062(3)
Mn(1)-O(1)	2.227(2)		

## Selected Bond angles (°) for octahedral geometries for Mn and Cr.

N(1)-Mn(1)-N(1) <sup>#1</sup>	90.06(13)	C(1)-Cr(1)-C(2)	88.59(10)
N(1)-Mn(1)-N(2)	90.68(10)	C(1)-Cr(1)-C(3)	89.14(10)
N(1)-Mn(1)-N(4)	92.75(8)	C(1)-Cr(1)-C(2) <sup>#2</sup>	91.41(10)
N(1)-Mn(1)-O(1)	85.04(7)	C(1)-Cr(1)-C(3) <sup>#2</sup>	90.86(10)
N(2)-Mn(1)-N(2) <sup>#1</sup>	88.56(12)	C(2)-Cr(1)-C(3)	88.36(10)
N(2)-Mn(1)-N(4)	88.23(8)	C(2)-Cr(1)-C(3) <sup>#2</sup>	91.64(10)
N(2)-Mn(1)-O(1)	94.01(8)		
N(1)-Mn(1)-N(2) <sup>#1</sup>	178.74(8)		
N(4)-Mn(1)-O(1)	176.87(11)		

Symmetry codes: #1 x, y - 1/2, z; #2 - x, -y, -z.

## Selected bond angles (°) for two dimensional sheet.

C(1)-N(1)-Mn(1)	170.9(2)	N(1)-C(1)-Cr(1)	177.1(2)
C(2) <sup>#1</sup> -N(2)-Mn(1)	156.0(2)	N(2) <sup>#2</sup> -C(2)-Cr(1)	175.7(2)

Symmetry codes: #1 x+1, y, z; #2 x-1, y, z.

## Distances for hydrogen bonds (Å).

N(5)⋯O(1) <sup>#1</sup>	2.937(4)	N(3)⋯O(1) <sup>#2</sup>	2.752(4)
N(5)⋯O(2)	2.831(9)	N(3)⋯O(1) <sup>#3</sup>	2.752(4)

Symmetry codes: #1 - x+1/2, y, z+1/2; #2 -x+1/2, y, z-1/2; #3 -x+1/2, -y+1/2, z-1/2.

## Selected intra-network metal separations (Å) through one cyanide group.

Mn(1)⋯Cr(1) <sup>a</sup>	5.3802(5)
Mn(1)⋯Cr(1) <sup>#1, b</sup>	5.2813(5)
Mn(1)⋯Cr(1) (Ave.)	5.3308(7)

Metal separation through <sup>a</sup>C(1)-N(1), <sup>b</sup>C(2)-N(2). Symmetry codes: #1 x+1, y, z.

Selected intra-network metal separations (Å) through two cyanide groups.

Mn(1)⋯Mn(1) <sup>#1, c</sup>	7.5177(10)	Cr(1)⋯Cr(1) <sup>#1, c</sup>	7.5177(8)
Mn(1)⋯Mn(1) <sup>#2, d</sup>	7.5605(7)	Cr(1)⋯Cr(1) <sup>#3, d</sup>	7.3246(8)

Metal separation along to <sup>c</sup>// *a*-axis and <sup>d</sup>// *b*-axis Symmetry codes: #1 *x*+1, *y*, *z*; #2 -*x*+1, -*y*+1, -*z*; #3 - *x*, *y*+1/2, -*z*.

Selected inter-network metal separations (Å).

Mn(1)⋯Cr(1) <sup>#1</sup>	7.4984(7)	Mn(1)⋯Mn(1) <sup>#3</sup>	8.3066(9)
Cr(1)⋯Cr(1) <sup>#2</sup>	8.3686(7)	Mn(1)⋯Mn(1) <sup>#4</sup>	8.4326(9)

Symmetry codes: #1 *x*+1/2, -*y*, *z*-1/2; #2 *x*+1/2, -*y*, -*z*+1/2; #3 -*x*+3/2, *y*, +1/2; #4 - *x*+1/2, *y*, *z*+1/2.

### V-3.1.1. Crystal structure for enGN and its rehydrated form

Details of the crystal data are given in table 5-1 and a list of the bond distances and angles is given in table 5-2. X-ray structural analyses of the diffraction data on a single crystal of **enGN** suggest an achiral orthorhombic *P* *cmn* space-group, compared to a chiral orthorhombic *P* 2<sub>1</sub>2<sub>1</sub>2<sub>1</sub> for **RGN-LTP** containing only the *R*-enantiomer of propanediamine and an achiral monoclinic *P* 2<sub>1</sub>/*m* for **racGN** containing both the *S*- and *R*-enantiomers of propanediamine. The key feature of all the crystal structures is the 2D-square grid of Mn and Cr(CN)<sub>4</sub> where the Mn and Cr alternate in the *ab*-plane and bridged by cyanide. However, the layers are not planar but are corrugated and propagated along the *b*-axis and are in-phase with the neighboring layers. Viewing along the *c*-axis, that is perpendicular to the layers, we find that adjacent layers are staggered. The remaining two cyanide groups complete the octahedral coordination of the Cr atom and pointing out of the layers while the amine and one water molecule are coordinated *trans*- to each other to the Mn atom. (Figure 5-1)

As can be seen in table 5-2, Mn(1)-N/O distances range from 2.198(2) to 2.303(3) Å and N-Mn-N/O angles are in the range of 85.04(7) - 92.75(8)° and 176.87(11) - 178.74(8)° for *cis* and *trans* positions. While Cr(1)-C distances range from 2.062(3) to 2.066(2) Å and C-Cr-C angles are in the range of 88.36(10) - 91.64(10)° for *cis* positions.

The space-group for **RGN-LTP** is *P* 2<sub>1</sub>2<sub>1</sub>2<sub>1</sub>, and it is changed to *P* *cmn* by use of achiral en, which introduces a mirror plane perpendicular to *b*-axis, *n* glide symmetry and inversion

center. The Mn, both nitrogen atoms of en are on the mirror plane and the Cr atom locates on as inversion center.

In the two-dimensional sheet, the average separation between the Mn and Cr atoms through the cyanide bridge is 5.3308(7) Å for **enGN**, which is slightly shorter than that for **RGN-LTP** (5.3457(16) Å). The shortest intersheet metal-metal separation for **enGN** is observed between the Mn and Cr atoms (7.4984(7) Å), while the shortest intersheet homometallic contacts are longer than 8.3066(9) Å. From the viewpoint of the magnetic dipole interaction, a distance of less than 10 Å describes a ferromagnetic interaction between two-dimensional sheets, which is the same situation as for the **RGN-LTP** compound.

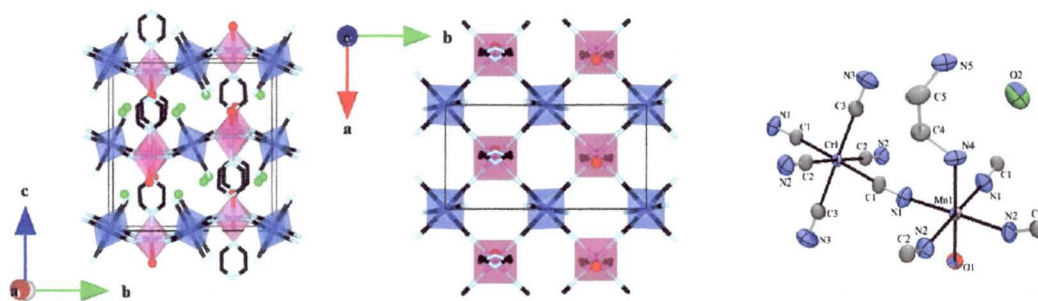


**Figure 5-1.** Projections of the structures along the *a*-axis (left), a view of the square grid layer of Mn (pink) and Cr (blue) atoms connected through cyanide (middle), and ORTEP drawing (right) for **enGN**. The two water molecules (red and green) are differentiated by the use of different colors.

Between the two-dimensional sheets, the nitrogen atom N(5) in the non-coordinating amine and found to have two hydrogen bond with the oxygen atoms of the non-coordinated water molecules, (N(5)⋯O(2), 2.831(9) Å), and with the oxygen atom of coordinating water (N(5)⋯O(1'), 2.937(4) Å). Furthermore, the oxygen atom O(1) of the coordinating water is found to have two hydrogen bonds between nitrogen of cyanide group in neighboring layer



(O(1)···N(3'), 2.752(4) Å). One hydrogen bond is generated by mirror symmetry from the other.

### V-3.1.2. Crystal structure for dehydrated structure of enGN-DP

Attempts to collect diffraction data for the dehydrated crystal failed as practically all the Bragg diffractions disappeared upon dehydration. However magnetic measurement showed an increase of about 30 K in the Curie temperature (see below) suggesting for the formation of a 3-D structure, comparable to those observed for *RGN-DP* and *racGN-DP*. The dehydration for the latter two compounds changes the crystal system from a 2D magnetic dimensionality to one of 3D and is accompanied by a giant leap of the Curie temperature from  $38\pm 2$  to  $73\pm 2$  K. Interestingly the Bragg diffraction is recovered with almost the same quality after exposure of the same crystal to air suggesting reversibility. Compared to propanediamine where the two nitrogen atoms are different to one another, in ethylenediamine they are equivalent. This equivalence results in a higher symmetry space-group and a disorder of the ethylenediamine where the two nitrogen atoms have fully occupied positions and common to the disordered pair. This also results in the two nearest cyanide groups from the Cr atoms of adjacent layers to be equidistant from the coordinating oxygen atom of the water molecule. Therefore, we propose that upon dehydration there is equal probability for either cyanide to occupy the position of the leaving water molecule and consequently, causes severe disorder and loss of the crystallinity. On the other hand, rehydration repairs the faults and brings about complete recovery of order within the structure.

### V-3.2. Thermogravimetric analyses

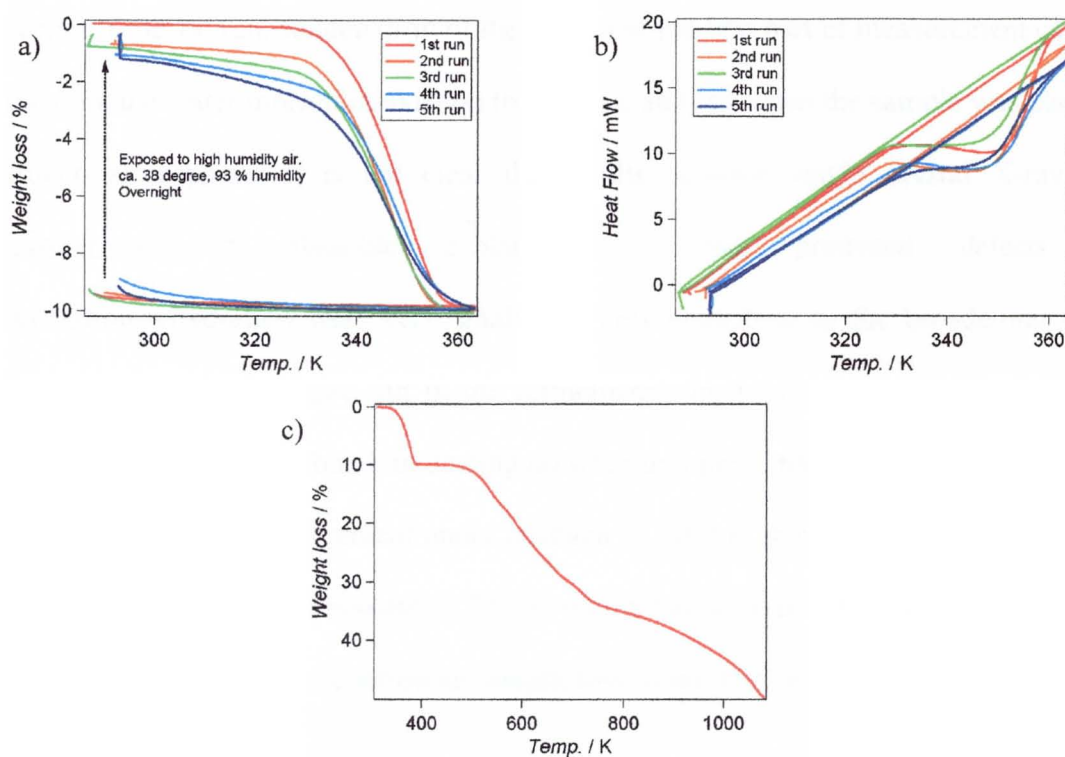


**Figure 5-2.** (a) Thermogravimetric, (b) DTA curves for **enGN** for several cycles of in the low temperature region, (c) TGA measurement for the high temperature region.

The TG measurements were performed on several samples consisting of powdered crystals of **enGN** under nitrogen atmosphere. In each case the sample shows a first weight loss starting at 340 K and attains a plateau at 360 K, which is stable up to 480 K where it decomposes (Figure 5-2). The observed percentage weight loss (9.8%) is close to the value for the departure of two water molecules per formula unit (10.0%). On lowering the temperature of the samples having been heated only to 363 K under nitrogen the sample weight is slightly increased. Upon exposure of the samples to high humidity air (humidity  $\approx$  93%, temperature  $\approx$  310 K) for overnight, they re-absorb water and recover 93% of water molecules. This recovery was labeled as dehydrated **enGN-DP** to rehydrated **enGN-HP**. Dehydration-rehydration processes are not perfectly reversible and the iteratively measurement showed slightly less and less rehydration ratio (92%, 90%, 88%, and 88%, for

after 2nd, 3rd, 4th, and 5th run), describing more and more fragments were introduced. Except for the 1st run, sudden drop of the weight at the first part of measurement can be seen, indicating the water molecules exist on the surface and left when the sample was placed under nitrogen atmosphere. It is not clear the results between single crystal X-ray and TG measurements. A plausible explanation is that produced defects through dehydration-rehydration were very small and only contribute to the broadening the Bragg reflections and are averaged out in the refinements. In the DTA curve (Figure 5-2b), only endothermic peaks were found, indicating no structural phase transition in **enGN**.

An independent measurement under nitrogen to 1100 K shows a gradual weight loss from 470 K to a metastable compound at 750 K which has a mass corresponding to  $\text{MnCr}(\text{CN})_5$  and is followed by another continuous weight loss to the 1100 K (Figure 5-2c).

### **V-3.3. Powder X-ray diffraction**

To verify the structural changes taking place during dehydration and rehydration, powder X-ray diffraction for each phase was collected by in-situ measurement. Diffraction data for virgin sample of **enGN** on a glass plate were collected. The same experiment for **enGN-DP** was performed after the sample had been dehydrated for 10 min at 360 K. Then, the data for the rehydrated sample of **enGN-HP** were collected after exposing the same sample to air for 1 hour. The results are shown in figure 5-3 together with the diffraction pattern calculated from the single-crystal data. It is clear that the pattern for virgin **enGN**, and hydrated **enGN-HP** show almost same pattern, indicating dehydration is reversible. However, the loss of crystallinity was always observed for the dehydrated samples.

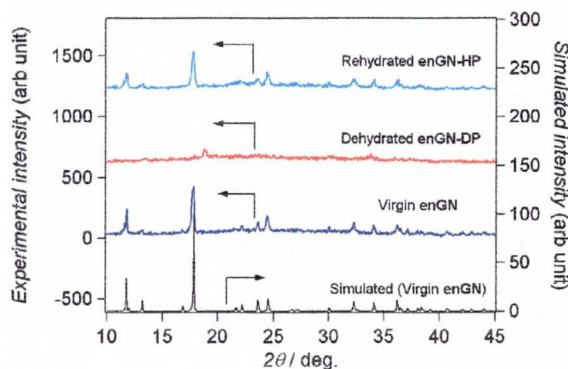


**Figure 5-3** Experimental and simulated XRPD (Cu K $\alpha$ ) patterns for virgin **enGN**, dehydrated **enGN-DP**, and rehydrated **enGN-HP**.

### V-3.4. Infrared spectroscopy

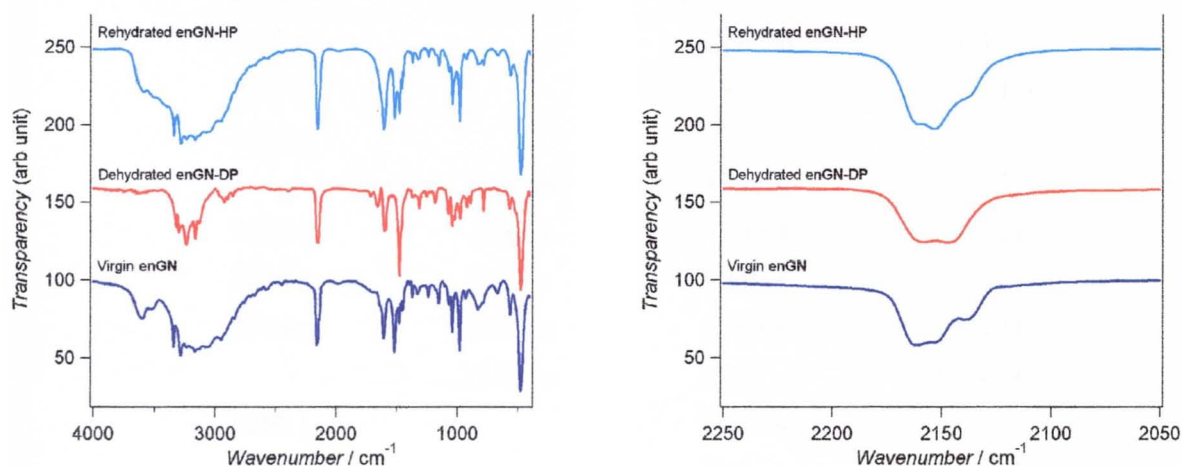


**Figure 5-4.** Infrared transmission spectra of **enGN**, dehydrated **enGN-DP**, and rehydrated **enGN-HP**.

The infrared spectra of the virgin, dehydrated, and rehydrated phases are shown in figure 5-4. The bands can be assigned using group frequencies as follows (Table 5-3). The asymmetric and symmetric stretching modes of the water molecules are observed at the highest energy peaks at 3600 and 3523  $\text{cm}^{-1}$ , respectively. Its bending mode is observed at 1701  $\text{cm}^{-1}$ . All three bands are absent from the spectrum of the **enGN-DP** and emerged in **enGN-HP** confirming the dehydration and rehydration process. The corresponding NH stretching modes and those of CH are observed at lower energies. We note that some sharpening of these bands are observed in the spectrum of the **enGN-DP** compared to **enGN**

and **enGN-HP** which may be associated with the presence of hydrogen bonds. Three sharp bands of stretching modes of the cyanide are observed in the spectra of **enGN** and **enGN-HP**, where the intensities are 2:2:1 which may suggest that the weaker may be the non-coordinating cyanide. However, for **enGN-DP** there are only two peaks, which may be due to all the cyanide groups are now bridging. A very strong peak at  $474\text{ cm}^{-1}$  is seen in all spectra which may be due to Cr-C mode.

**Table 5-3.** Frequencies and assignments of the bands in the spectra of the **enGN**, dehydrated **enGN-DP**, and **enGN-HP**.

<b>enGN</b>	<b>enGN-DP</b>	<b>enGN-HP</b>	
3600 m		3590 m	$\nu(\text{O-H})$
3523 m		3502 m	$\nu(\text{O-H})$
3342 s		3340 s	$\nu(\text{N-H})$
	3323 m	3322 s	$\nu(\text{N-H})$
3284 s	3298 s	3284 s	$\nu(\text{N-H})$
3236 s	3238 s	3240 s	$\nu(\text{N-H})$
3164 s	3165 s	3166 s	$\nu(\text{N-H})$
	3130 m	3132 s	$\nu(\text{N-H})$
3066 s		3056 s	
2966 s		2964 s	$\nu(\text{C-H})$
2947 s	2924 m	2947 s	$\nu(\text{C-H})$
2839 m	2897 w	2841 m	$\nu(\text{C-H})$
	2852 w		$\nu(\text{C-H})$
	2831 vw		$\nu(\text{C-H})$
2162 s	2158 s	2161 s	$\nu(\text{C-N})$
2152 s	2146 s	2154 s	$\nu(\text{C-N})$
2139 m		2139 m	$\nu(\text{C-N})$
1990 vw			
	1714 w		
	1658 m		
1606 s	1600 s	1606 s	$\delta(\text{N-H})$
	1593 s		$\delta(\text{N-H})$
1519 s		1520 s	$\delta(\text{C-H})$
1477 m	1475 vs	1477 s	$\delta(\text{C-H})$

1462 m		1460 m	$\delta(\text{C-H})$
1446 m		1448 m	$\delta(\text{C-H})$
1371 w	1369 w	1371 w	
1329 w	1315 m	1327 w	
1240 w	1254 w	1240 w	
1184 m	1184 m	1182 w	$\nu(\text{C-N})$
		1153 w	$\nu(\text{C-N})$
1103 vw	1074 m	1103 w	$\nu(\text{C-N})$
1068 m	1043 m	1066 m	$\nu(\text{C-N})$
1041 s	1026 m	1041 m	$\nu(\text{C-N})$
982 s	980 m	981 s	$\nu(\text{C-N})$
931 w	922 m	930 w	$\delta(\text{N-H})$
	891 m		$\delta(\text{N-H})$
833 m		833 w	$\delta(\text{N-H})$
785 m	785 m	784 w	$\delta(\text{N-H})$
669 w		669 w	
565 w	570 m	565 m	
476 vs	474 vs	476 vs	$\nu(\text{Cr-C})$

### V-3.5. Magnetic properties

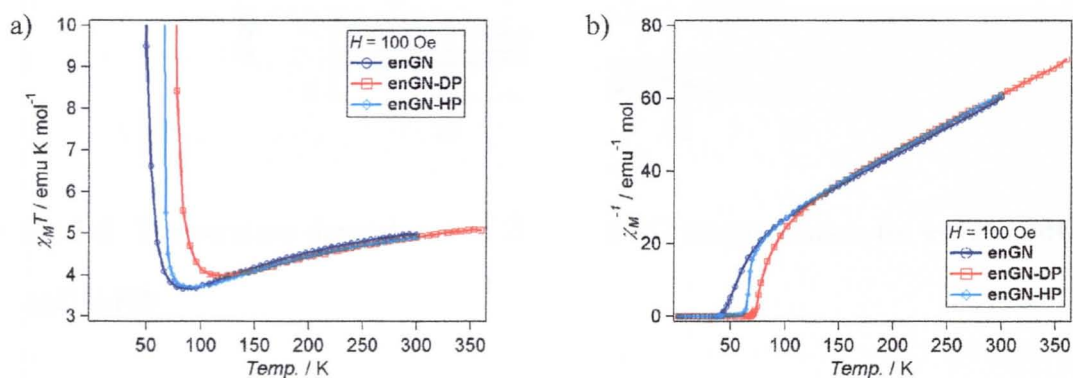


**Figure 5-5.** Temperature dependence of (a)  $\chi_M T$  and (b)  $\chi_M^{-1}$  for virgin **enGN**, dehydrated **enGN-DP**, and rehydrated **enGN-HP**.

The temperature dependence of  $\chi_M T$  for **enGN**, **enGN-DP**, and rehydrated **enGN-HP** measured in a field of 100 Oe are displayed in figure 5-5a. The  $\chi_M T$  values are 4.96, 4.90, and 4.90  $\text{emu K mol}^{-1}$  at 300 K, and decrease with lowering temperature down to a minimum value of 3.67 (90 K), 3.99 (120 K), and 3.70 (90 K)  $\text{emu K mol}^{-1}$ , respectively. Upon further

cooling, the  $\chi_M T$  values increase to maximum values of 951 (32 K), 2005 (55 K), and 1104 emu K mol<sup>-1</sup> (32 K) before decreasing below these temperatures, respectively. The  $\chi_M^{-1}$  value for each phase follows the Curie-Weiss law ( $\chi_M = C / (T - \theta)$ ) with Weiss constant  $\theta$  of -72.5, -83.7, and -73.2 K and Curie constant  $C$  of 6.20, 6.28, and 6.09 emu K mol<sup>-1</sup>, respectively (figure 5-5b). These Curie constants are comparable to the theoretical value (for Mn(II) and Cr(III) :  $1/2 \times 5/2 \times 7/2 + 1/2 \times 3/2 \times 5/2 = 6.25$  emu K mol<sup>-1</sup>). The negative Weiss constants indicate considerable antiferromagnetic interaction between Cr<sup>III</sup> ion and Mn<sup>II</sup> ions through the cyanide bridge.

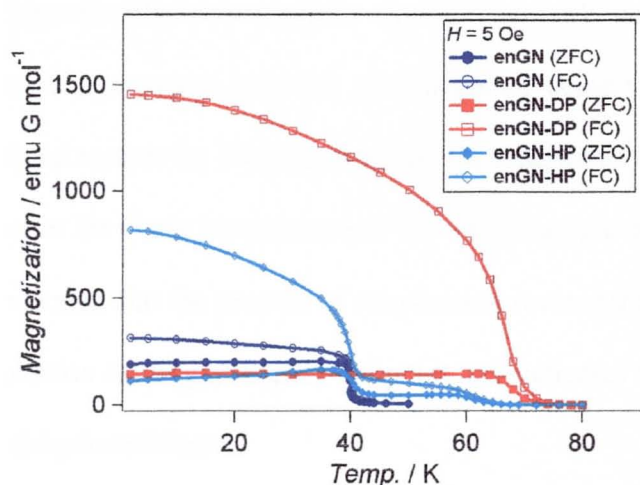


**Figure 5-6.** Temperature dependence of ZFC and FC magnetization for **enGN**, **enGN-DP**, and **enGN-HP**.

In the zero-field-cooled (ZFC) and field-cooled (FC) measurements in an applied field of 5 Oe, spontaneous magnetization confirming long-range magnetic orderings are observed below 42, 75 and 42 (+65) K for **enGN**, **enGN-DP** and **enGN-HP**, respectively (Figure 5-6). The small difference of the  $T_C$  value between **enGN** and **RGN-LTP** can be explained by exchange interaction due to slight structural differences within the layer. For **RGN-LTP**, the average metal separations between Mn and Cr atom in the two-dimensional sheets for

**RGN-LTP** (5.3457(16) Å) is longer than that for **enGN** (5.3307(7) Å). Therefore, molecular overlap between metal sites involving the cyanide ligand orbitals for **enGN** is more than that for **RGN-LTP**, which describes the higher  $T_C$  value than **RGN-LTP**. For **enGN-DP**  $T_C$  is significantly higher than the virgin sample. In the previous papers, the relationship between magnetic properties and crystal structure for the similar compound (**RGN-LTP**) was discussed. The Curie temperature of **RGN-LTP** increases from 38 to 73 K, accompanying crystal dimensionality change from 2-D to 3-D upon dehydration. It is understood as a consequence of the increase neighbors through the cyanide network and appearance of relatively shorter Mn···Cr distance. For the case of **enGN**, all of the water molecules have been released. Consequently, new random cyanide network between adjacent layers are formed, giving more connection between paramagnetic centers. Upon rehydration of the previously dehydrated sample by soaking in water, the magnetization in a field of 5 Oe shows two anomalies; one at the Curie temperature of the virgin sample and the other at 65 K. While the one at 42 K indicates that the process of rehydration reverse the sample to the virgin state, the small magnetization trailing at higher temperatures indicates that some fragments of the sample retain the dehydrated form.

A hysteresis loop for each compound was observed at 2 K (Figure 5-7). The observed saturation magnetization values for virgin **enGN**, dehydrated **enGN-DP**, and rehydrated **enGN-HP** were 2.02, 2.05 and 2.04  $\mu_B$ , respectively, which are in good agreement with the theoretical value for antiferromagnetic coupling between  $\text{Cr}^{3+}$  and  $\text{Mn}^{2+}$  ions ( $5/2 - 3/2 = 1$ ). The observed remanant magnetization are 0.36, 0.67, and 0.51  $\mu_B$  and coercive field in the hysteresis loop are 62, 101, and 62 Oe, respectively. These values suggest that **enGN** is a soft ferrimagnet while it slightly hardens upon dehydration and recover the initial softness by rehydration. A similar effect is observed for the propanediamine compounds.



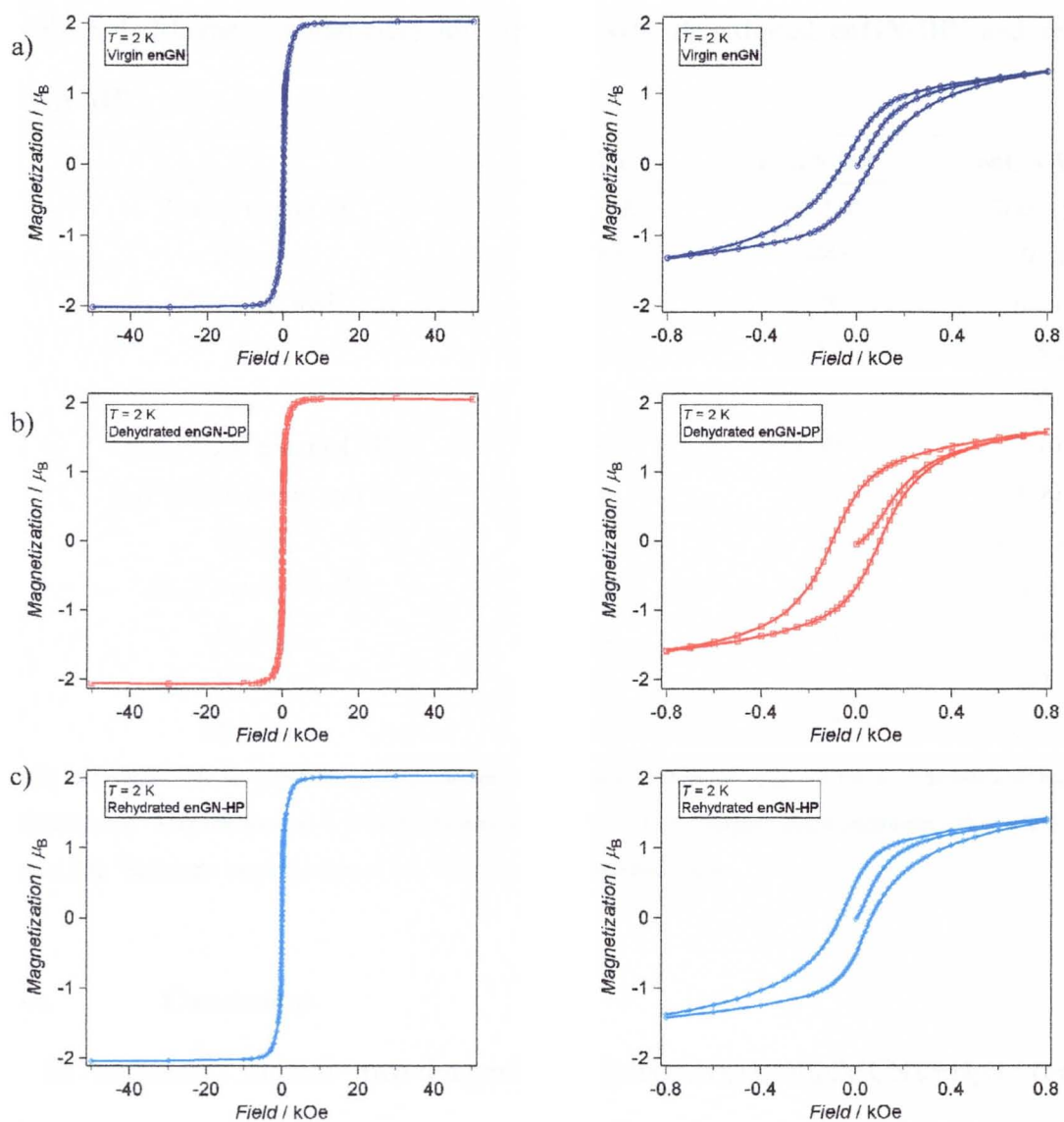


**Figure 5-7.** Field dependence of the magnetization at 2 K for (a) enGN, (b) enGN-DP, and (c) enGN-HP.

**Table 5-4.** Magnetic parameters for virgin **enGN**, dehydrated **enGN-DP**, and rehydrated **enGN-HP**.


	<b>enGN</b>	<b>enGN-DP</b>	<b>enGN-HP<sup>i</sup></b>
<i>Fitting region / K</i>	300 - 120	360-160	300-120
<i>R<sup>2</sup> value</i>	0.9998	0.9998	0.9998
<i>C<sup>a</sup> / cm<sup>3</sup> K mol<sup>-1</sup></i>	6.20	6.28	6.09
<i>θ<sup>b</sup> / K</i>	- 72.5	- 83.7	- 73.2
<i>T<sub>min</sub><sup>c</sup> / K</i>	90	120	90
<i>χ<sub>M</sub>T (T<sub>min</sub>)/ emu mol<sup>-1</sup> K</i>	3.67	3.99	3.70
<i>χ<sub>M</sub>T (300 K)/ emu mol<sup>-1</sup> K</i>	4.96	4.90	4.90
<i>T<sub>C</sub><sup>d</sup> / K</i>	42	75	42 (+65)
<i>M<sub>2K</sub><sup>e</sup> / emu G mol<sup>-1</sup></i>	480	1597	814
<i>M<sub>sat</sub><sup>f</sup> / μ<sub>B</sub></i>	2.02	2.05	2.04
<i>H<sub>C</sub><sup>g</sup> / Oe</i>	62	101	62
<i>M<sub>REM</sub><sup>h</sup> / μ<sub>B</sub></i>	0.36	0.67	0.51


<sup>a</sup>Curie constants. <sup>b</sup>Weiss constants. <sup>c</sup>Temperatures at minimum values of  $\chi_M T$ . <sup>d</sup>Critical temperatures based on FC measurements. <sup>e</sup>Magnetization at 2 K in FC measurement ( $H = 5$  Oe). <sup>f</sup>Magnetization saturation value at 2 K. <sup>g</sup>Coercive field at 2 K. <sup>h</sup>Remanant magnetization at 2 K. <sup>i</sup>After soaked in distilled water.

#### V-4. Conclusion

In summary, achiral two-dimensional  $[\text{Mn}(\text{enH})(\text{H}_2\text{O})][\text{Cr}(\text{CN})_6] \cdot \text{H}_2\text{O}$  (**enGN**) is successfully synthesized by the use of ethylenediamine having similar layered structure as  $[\text{Mn}(R/S\text{-pnH})(\text{H}_2\text{O})][\text{Cr}(\text{CN})_6] \cdot \text{H}_2\text{O}$  (**RGN-LTP/SGN-LTP**). It is a soft ferrimagnet with comparable  $T_{\text{Curie}}$  42 K as those of **RGN-LTP/SGN-LTP** and the coercivity and  $T_{\text{Curie}}$  are increased reversibly upon dehydration. These results indicate that **enGN** is a good reference to the chiral magnet (**RGN-LTP/SGN-LTP**). Further physical measurements will be undertaken to elucidate the effect of chirality by the use of both compounds. In contrast, reversible single crystal-to-amorphous dehydrated phase is found for **enGN** as a consequence of the high symmetry causing severe disorder due to equal statistical probability.

**Movies of transformation processes.**

Movie 5-1 : 2 Movie dehydration from **enGN** to **enGN-DH** 

Movie 5-2 : 4 Movie rehydration from **enGN-DH** to **enGN** 

## **Chapter VI**

### **Concluding Remarks**

## Chapter VI

### Concluding Remarks

The principal essence of the proposed project of the thesis has been achieved for the physics part (the study of the ac-susceptibilities and the magnetic structures from neutron diffraction) and the chemistry part (the present thesis) of it has been more than successful with the additional unexpected phase transitions that took a major part of the time to comprehend. Within the aim of the project, we have successfully synthesized three novel compounds, a chiral one  $[\text{Mn}(\text{R-pnH})(\text{H}_2\text{O})][\text{Cr}(\text{CN})_6]\cdot\text{H}_2\text{O}$  and two achiral congeners,  $[\text{Mn}(\text{rac-pnH})(\text{H}_2\text{O})][\text{Cr}(\text{CN})_6]\cdot\text{H}_2\text{O}$  and  $[\text{Mn}(\text{enH})(\text{H}_2\text{O})][\text{Cr}(\text{CN})_6]\cdot\text{H}_2\text{O}$ . Although the main structural, thermal, optical and magnetic properties have some similarities, there are several differences which turn out to be related to the symmetry or subtle difference in the packing arrangements. These are highlighted in the corresponding chapters.

$[\text{Mn}(\text{R-pnH})(\text{H}_2\text{O})][\text{Cr}(\text{CN})_6]\cdot\text{H}_2\text{O}$  proves to be the compound with the highest number of functionalities which include heterometallic mixed-valency, chirality, ferrimagnetism and proton-transfer, as well as surviving two single crystal-to-single crystal phase transitions reversibly without great loss of crystallinity. One of the phase transitions, which is of first-order, is promoted by a rare proton-transfer between amine/ammonium and water/hydroxonium couples which brings changes in the coordination of the amine and water and requires a concerted change of curvature of the corrugation of the Mn-CN-Cr layers as is commonly observed in muscles. Dehydration of the crystals introduces bridges between the layers resulting to an increase in magnetic dimensionality which in-turn enhances the Curie temperature from 38 to 73 K and adds a small amount of magnetic hardness and changes to the magnetic anisotropy. All these are absolutely reversible.

The achiral two-dimensional  $[\text{Mn}(\text{rac-pnH})(\text{H}_2\text{O})][\text{Cr}(\text{CN})_6]\cdot\text{H}_2\text{O}$  (**racGN**) provided a good test to elucidate the association between structural chirality and magnetic chirality. It is a soft ferrimagnet below 36 K. Comparing to **RGN-LTP/SGN-LTP**, common features are seen in the crystal structures, ferrimagnetic behavior which is dominated by the two-dimensional sheet organization and the ferromagnetic interaction between sheets, and softness of the magnet. Moreover, reversible dehydration is demonstrated on **racGN**. As a result of dehydration, the crystal structure is changed to three-dimensional accompanied by doubling of  $T_C$  to 70 K, and coercive field at 2 K increasing from 8 to 63 Oe.

The second achiral compound,  $[\text{Mn}(\text{enH})(\text{H}_2\text{O})][\text{Cr}(\text{CN})_6]\cdot\text{H}_2\text{O}$  (**enGN**), crystallizes in the achiral orthorhombic  $P\text{ cmn}$  space-group with similar structure and is a ferrimagnet ( $T_C = 42\text{ K}$ ). **enGN** shows reversible single crystal-to-an amorphous dehydrated phase, **enGN-DP** is ferrimagnetic ( $T_C = 75\text{ K}$ ).

TGA, DSC, IR and UV-vis spectroscopy provide additional evidences of the reversibility and reproducibility of the transitions as well as the thermodynamic order parameter of the transition and the mixed-valency character.

While major advances have been made in the last three years on the chemistry and physics of chiral magnets, which are accompanied by solid theoretical calculations, this work can be extended in using the acquired knowledge in the development of devices. On the academic aspects of chiral magnets further efforts can be made to create new materials having different space groups where the symmetry requirements for the coupling of structural chirality and magnetic chirality may be different and thus will provide food for thoughts. On the application aspect further work on using chiral magnets as optical filters may be a source of controlling optical information technology.

## References

- (1) (a) Blundell, S. J. *Magnetism in Condensed Matter*, Oxford University Press, **2001**. (b) Schieber, M. M. *Selected Topics in Solid State Physics, Experimental Magnetochemistry*, vol. VIII, Wohlfarth, E. P. (ed.), North-Holland, Amsterdam, **1967**.
- (2) (a) Chikazumi, S. *Physics of Ferromagnetism*; Oxford University Press: Oxford, **1992**. (b) Bertotti, G. *Hysteresis in Magnetism*; Academic Press: London, **1998**.
- (3) Herpin, A. *Theorie du Magnetisme*; Presse Universitaire de France: Paris, **1968**.
- (4) (a) Kurmoo, M.; Kepert, C. *J. New J. Chem.* **1998**, *22*, 1515. (b) Lappas, A.; Wills, A. S.; Green, M. A.; Prassides, K.; Kurmoo, M. *Phys. Rev. B* **2003**, *67*, 144406 (1-8).
- (5) (a) Gatteschi, D.; Sessoli, R. *Angew. Chem. Int. Ed.* **2003**, *42*, 268. (b) Tasiopoulos, A. J.; Vinslava, A.; Wernsdorfer, W.; Abboud, A.; Christou, G. *Angew. Chem. Int. Ed.* **2004**, *43*, 2117. (c) Wernsdorfer, W.; Aliaga-Alcaide, N.; Hendrickson, D. N.; Christou, G. *Nature* **2002**, *416*, 406. d) Ritter, S. K. *Chem. Eng. News* **2004**, *82*, 29.
- (6) (a) Caneschi, A.; Gatteschi, D.; Lalioti, N.; Sangregorio, C.; Sessoli, R.; Venturi, G.; Vindigni, A.; Rettori, A.; Pini, M. G.; Novak, M. A. *Angew. Chem. Int. Ed.* **2001**, *40*, 1760. (b) Clérac, R.; Miyasaka, H.; Yamashita, M.; Coulon, C. *J. Am. Chem. Soc.* **2002**, *124*, 12837. (c) Liu, T. F.; Fu, D.; Gao, S.; Zhang, Y. Z.; Sun, H. L.; Su, G.; Liu, Y. J. *J. Am. Chem. Soc.* **2003**, *125*, 13 976. (d) Ferbinteanu, M.; Miyasaka, H.; Wernsdorfer, W.; Nakata, K.; Sugiura, K.; Yamashita, M.; Coulon, C.; Clérac, R. *J. Am. Chem. Soc.* **2005**, *127*, 3090.
- (7) (a) Li, D.; Clérac, R.; Roubeau, O.; Harté, E.; Mathonière, C.; Bris, R. L.; Holmes, S. M. *J. Am. Chem. Soc.* **2007**, *129*, ASAP. (b) Ohkoshi, S.; Ikeda, S.; Hozumi, T.; Kashiwagi, T.; Hashimoto, K. *J. Am. Chem. Soc.* **2006**, *128*, 5320. (c) Bonhommeau, S.; Molnár, G.; Galet, A.; Zwick, A.; Real, J.-A.; McGarvey, J. J.; Bousseksou, A. *Angew. Chem. Int. Ed.* **2005**, *44*, 4069. (d) Hayami, S.; Motokawa, N.; Shuto, S.; Masuhara, N.; Someya, T.; Ogawa, Y.; Inoue, K.; Maeda, Y. *Inorg. Chem.* **2007**, *46*, 1789. (e) Herrera, J. M.; Marvaud, V.; Verdager, M.; Marrot, J.; Kalisz, M.; Mathonière, C.; *Angew. Chem. Int. Ed.* **2004**, *43*, 5468. (f) Sato, O. *Acc. Chem. Res.* **2003**, *36*, 692. (g) Sato, O.; Iyoda, T.; Fujishima, A.; Hashimoto, K. *Science* **1996**, *272*, 704.
- (8) (a) Kaneko, W.; Ohba, M.; Kitagawa, S. *J. Am. Chem. Soc.* **2007**, *129*, 13706. (b) Ohkoshi, S.; Tsunobuchi, Y.; Takahashi, H.; Hozumi, T.; Shiro, M.; Hashimoto, K. *J. Am. Chem. Soc.* **2007**, *129*, 3084. (c) Yanai, N.; Kaneko, W.; Yoneda, K.; Ohba, M.; Kitagawa, S. *J. Am. Chem. Soc.* **2007**, *129*, 3496. (d) Nihei, M.; Han, L.; Oshio, H. *J. Am. Chem. Soc.* **2007**, *129*, 5312. (e) Kurmoo, M.; Kumagai, H.; Akita-Tanaka, M.;

- Inoue, K.; Takagi, S. *Inorg. Chem.* **2006**, *45*, 1627. (f) Galet, A.; Muñoz, M.C.; Real, J. A. *Chem. Commun.* **2006**, 4321. (g) Zeng, M.-H.; Feng, Z.-L.; Zhang, W.-X.; Chen, Z.-M. *Dalton Trans.* **2006**, 5294. (h) Kurmoo, M.; Kumagai, H.; Chapman, K. W.; Kepert, C. J. *Chem. Commun.* **2005**, 3012. (i) Ohkoshi, S.; Arai, K.; Sato, Y.; Hashimoto, K. *Nature Mat.* **2004**, *3*, 857. (j) Wang, Z.; Zhang, B.; Fujiwara, H.; Kobayashi, H.; Kurmoo, M. *Chem. Commun.* **2004**, 416. (k) MasPOCH, D.; Ruiz-Molina, D.; Wurst, K.; Domingo, N.; Gavallini, M.; Biscarini, F.; Tajada, J.; Rovira, C.; Veciana, J. *Nat. Mater.* **2003**, *2*, 190. (l) Niel, V.; Thompson, A. L.; Munoz, M. C.; A. Galet; Goeta, A. E.; Real, J. A. *Angew. Chem. Int. Ed.* **2003**, *42*, 3759. (m) Halder, G. J.; Kepert, C. J.; Moubaraki, B.; Murray, K. S.; Cashion, J. D. *Science* **2002**, *298*, 1762.
- (9) (a) Cororado, E.; Galán-Mascarós, J. R.; Gómez-García, C. J.; Laukhin, V. *Nature* **2000**, *408*, 447. (b) Kurmoo, M.; Graham, A. W.; Day, P.; Coles, S. J.; Hursthouse, M. B.; Caulfield, J. L.; Singleton, J.; Pratt, F. L.; Hayes, W.; Ducasse, L.; Guionneau, P. *J. Am. Chem. Soc.* **1995**, *117*, 12209. (c) Cororado, E.; Day, P. *Chem. Rev.* **2004**, *104*, 5419. (d) Uji, S.; Shinagawa, H.; Terashima, T.; Yakabe, T.; Terai, Y.; Tokumoto, M.; Kobayashi, A.; Tanaka, H.; Kobayashi, H. *Nature* **2001**, *410*, 908. (e) Kobayashi, H.; Cui, H. -B.; Kobayashi, A. *Chem. Rev.* **2004**, *104*, 5265. (f) Ohkoshi, S.; Tokoro, H.; Matsuda, T.; Takahashi, H.; Irie, H.; Hashimoto, K. *Angew. Chem. Int. Ed.* **2007**, *46*, 3238. (g) Cui, H.B.; Wang, Z.; Takahashi, K.; Okano, Y.; Kobayashi, H.; Kobayashi, A. *J. Am. Chem. Soc.* **2006**, *128*, 15074.
- (10) Lacroix, P. G.; Malfant, I.; Bénard, S.; Yu, P.; Rivière, E.; Nakatani, K.; *Chem. Mater.* **2001**, *13*, 441.
- (11) Rikken, G. L. J. A.; Raupach, E. *Nature.* **1997**, *390*, 493.
- (12) (a) Dzyaloshinski, I. *J. Phys. Chem. Solids* **1958**, *4*, 241. (b) Moriya, T. *Phys. Rev.* **1960**, *120*, 91.
- (13) (a) Wang, Z.; Zhang, B.; Inoue, K.; Fujiwara, H.; Otsuka, T.; Kobayashi, H.; Kurmoo, M. *Inorg. Chem.* **2007**, *46*, 437. (b) Gao, E. Q.; Yue, Y. F.; Bai, S. Q.; He, Z.; Yan, C. -H. *J. Am. Chem. Soc.* **2004**, *126*, 1419. (c) Clemente-León, M.; Coronado, E.; Gómez-García, C. J.; Soriano-Portillo, A. *Inorg. Chem.* **2006**, *45*, 5653. (d) Andrés, R.; Brissard, M.; Gruselle, M.; Train, C.; Vaissermann, J.; Malézieux, B.; Jamet, J. P.; Verdaguer M., *Inorg. Chem.* **2001**, *40*, 4633.
- (14) (a) Milon, J.; Daniel, M.-C.; Kaiba, A.; Guionneau, P.; Brandès, S.; Sutter, J.-P. *J. Am. Chem. Soc.* **2007**, *129*, 13872. (b) Kaneko, W.; Ohba, M.; Kitagawa, S. *J. Am. Chem. Soc.* **2007**, *129*, 248. (c) Higashikawa, H.; Okuda, K.; Kishine, J.; Masuhara, N.; Inoue, K. *Chem. Lett.* **2007**, *36*, 1022. (d) Imai, H.; Inoue, K.; Kikuchi, K.; Yoshida, Y.; Ito,



- M.; Sunahara, T.; Onaka, S. *Angew. Chem. Int. Ed.* **2004**, *43*, 5618. (e) Coronado, E.; Gómez-García, C. J.; Nuez, A.; Romeo, F. M.; Rusanov, E.; Stoeckli-Evans, H. *Inorg. Chem.* **2002**, *41*, 4615. (f) Inoue, K.; Imai, H.; Ghalsasi, P. S.; Kikuchi, K.; Ohba, M.; Okawa, H.; Yakhmi, J. V. *Angew. Chem. Int. Ed.* **2001**, *40*, 4242.
- (15) Inoue, K.; Kikuchi, K.; Ohba, M.; Okawa, H. *Angew. Chem. Int. Ed.* **2003**, *42*, 4810.
- (16) (a) Akita-Tanaka, M.; Kumagai, H.; Markosyan, A.; Inoue, K. *Bull. Chem. Soc. Jpn.* **2007**, *80*, 204. (b) Numata, Y.; Inoue, K.; Baranov, N.; Kurmoo, M.; Kikuchi, K. *J. Am. Chem. Soc.* **2007**, *129*, 9902. (c) Munguet, M.; Luneau, D.; Lhotel, E.; Villar, V.; Paulsen, C.; Amabilino, D. B.; Veciana, J. *Angew. Chem. Int. Ed.* **2002**, *41*, 586. (d) Kumagai, H.; Inoue, K. *Angew. Chem. Int. Ed.* **1999**, *38*, 1601.
- (17) (a) Coronado, E.; Galán-Mascarós, J. R.; Gómez-García, C. J.; Mursia-Martínez, A. *Chem. Eur. J.* **2006**, *12*, 3484. (b) Zeng, M.-H.; Wang, B.; Wang, X.-Y.; Zhang, W.-X.; Chen, X.-M.; Gao, S. *Inorg. Chem.* **2006**, *45*, 7069.
- (18) Zhang, B.; Wang, Z.; Kurmoo, M.; Gao, S.; Inoue, K.; Kobayashi, H. *Adv. Funct. Mater.* **2007**, *17*, 577.
- (19) Kishine, J.; Inoue, K.; Yoshida, Y. *Prog. Theor. Phys. Suppl.* **2005**, *82*. (b) Blokhin, I. V.; Markosyan, A. S.; Morgunov, R. B.; Inoue, K.; Tanimoto, Y.; Yoshida, Y. *Physics of the Solid State* **2005**, *47*, 2106. (c) Hoshikawa, A.; Kamiyama, T.; Purwanto, A.; Ohishi, K.; Higemoto, W.; Ishigaki, T.; Imai, H.; Inoue, K. *J. Phys. Soc. Jpn* **2004**, *73*, 2597. (d) Ohishi, K.; Higemoto, W.; Koda, A.; Saha, S. R.; Kadono, R.; Inoue, K.; Imai, H.; Higasikawa, H. *J. Phys. Soc. Jpn* **2006**, *75*, 063705. (e) Inoue, K.; Ohkoshi, S.; Imai, H. *Magnetism : Molecules to Materials V*; Miller, J. S.; Drillon, M. Ed.; Wiley-VCH; Weinheim, 2005, 41.
- (20) (a) Supriya, A.; Das, S. K. *J. Am. Chem. Soc.* **2007**, *129*, 3464 (b) Kobatake, S.; Takami, S.; Muto, H.; Ishikawa, T.; Irie, M.; *Nature* **2007**, *446*, 778 (c) Horie, M.; Sassa, T.; Hashizume, D.; Suzaki, Y.; Osakada, K.; Wada, T. *Angew. Chem.* **2007**, *46*, 4983 (d) Suh, M. P.; Cheon, Y. E.; Lee, E. Y. *Chem. Eur. J.* **2007**, *13*, 4208 (e) Le, E. Y.; Suh, M. P. *Angew. Chem. Int. Ed.* **2004**, *43*, 2798 (f) Takaoka, K.; Kawano, M.; Tominaga, M.; Fujita, M. *Angew. Chem. Int. Ed.* **2005**, *44*, 2151.
- (21) (a) Uehara, A.; Kaizaki, S. *4th Edition Jikken kagaku kouza 17 : Muki sakutai · Kire-to sakutai* (In Japanese); Nihon kagaku kai Ed.; Tokyo, **1991**, 60. (b) B.Schaap, W.; Krishnamurthy, R.; Wakefield, D. K.; Coleman, W. F. *Coordination Chemistry*; Kirschner, S. Ed.; Plenum, **1969**, 177.
- (22) (a) Hidaka, J.; Fujita, J.; Yasui, T. *4th Edition Jikken kagaku kouza 17 : Muki sakutai · Kire-to sakutai* (In Japanese); Nihon kagaku kai Ed.; Tokyo, 1991, 98. (b) Dwyer, F. P.; Garvan, F. L.; Shulman, A. *J. Am. Chem. Soc.* **1959**, *81*, 290.

- (23) Kahn, O. *Molecular Magnetism*; WILEY-VCH; New York, **1993**, 3.
- (24) Diamagnetic corrections:  $-1.891 \times 10^{-4}$ ,  $-1.891 \times 10^{-4}$ , and  $-1.631 \times 10^{-4} \text{ cm}^3 \text{ mol}^{-1}$  for **RGN-LTP**, **RGN-HTP** and **RGN-DP**;  $-1.891 \times 10^{-4}$ ,  $-1.631 \times 10^{-4}$ , and  $-1.891 \times 10^{-4} \text{ cm}^3 \text{ mol}^{-1}$  for virgin **racGN**, dehydrated **racGN-DP**, and rehydrated **racGN-HP**;  $-1.783 \times 10^{-4}$ ,  $-1.523 \times 10^{-4}$ , and  $-1.783 \times 10^{-4} \text{ cm}^3 \text{ mol}^{-1}$  for virgin **enGN-DP**, dehydrated **enGN-DP**, and rehydrated **enGN-HP**.
- (25) Armentano, D.; De Munno, G.; Mastropietro T. F.; Julve, M.; Lloret F. *J. Am. Chem. Soc.* **2005**, *127*, 10778.
- (26) Ti, T; Tancrez, N; Clement, R; Ledoux-Rax, I; Zyss, J. *J. Luminescence*, **2004**, *110(4)*, 389.
- (27) Murayama, A.; Sakuma, M. *Applied Physics Letters* **2006**, *88*, 122504.
- (28) Verdaguer, M.; Girolami, G. S. *Magnetism : Molecules to Materials V*; Miller, J. S.; Drillon, M. Ed.; Wiley-VCH; Weinheim, **2005**, 303.
- (29) Izumi, F.; Ikeda, T. *Mater. Sci. Forum* **2000**, *321-324*, 198.

## **APPENDIX**

**Full Paper Submitted to Inorganica Chimica Acta**

**Syntheses, Structures and Magnetic Properties of One-  
Dimensional Chains of Transition Metals with O-P-O Bridges**

**Yusuke Yoshida, Katsuya Inoue, Natalie Kyritsakas  
and Mohamedally Kurmoo**

## Syntheses, Structures and Magnetic Properties of One-Dimensional Chains of Transition Metals with O-P-O Bridges

Yusuke Yoshida,<sup>a,b</sup> Katsuya Inoue,<sup>b</sup> Natalie Kyritsakas<sup>a</sup> and Mohamedally Kurmoo\*<sup>a</sup>

<sup>a</sup> Laboratoire de Chimie de Coordination Organique, CNRS-UMR7140, Université Louis Pasteur, Institut Le Bel, 4 rue Blaise Pascal, 67000 Strasbourg Cedex 01, France.

<sup>b</sup> Department of Chemistry and Institute for Advanced Materials Research, Hiroshima University, Kagamiyama, Higashi-Hiroshima, 739-8526, Japan.

**Keywords:** Pyrophosphite / Magnetic properties / One-dimensional chain /

Supporting information for this article is available at <http://www.rsc.org> or from the corresponding author.

*Corresponding author:*

Dr Mohamedally Kurmoo

Laboratoire de Chimie de Coordination Organique, CNRS-UMR7140, Université Louis Pasteur, Institut Le Bel, 4 rue Blaise Pascal, 67000 Strasbourg Cedex 01, France.

E-mail: [kurmoo@chimie.u-strasbg.fr](mailto:kurmoo@chimie.u-strasbg.fr)

---

A novel series of linear chain coordination polymers,  $[\text{NH}_4][\text{M}^{\text{II}}(\text{H}_2\text{PO}_2)_3(\text{H}_2\text{O})]$  where M = Mn, Co, Ni, has been obtained by the reaction of divalent metals salts with ammonium pyrophosphite,  $[\text{NH}_4][\text{H}_2\text{PO}_2]$ , in a methanol-water mixture. They crystallise in the monoclinic  $P 2_1/n$  cell which contain polar chains aligned with opposing polarity. Both bridging and terminal monodentate coordination modes are exhibited by the  $\text{H}_2\text{PO}_2^-$ . Two types of hydrogen-bond between a coordinated water and a monodentate  $\text{H}_2\text{PO}_2^-$  connect the chains into a 3D-network. The compounds have been further characterised by IR and UV-vis spectroscopies, TGA, and their magnetic properties measured. All three compounds exhibit weak antiferromagnetic nearest neighbour interaction. A similar study on the known  $\text{Fe}^{\text{III}}(\text{H}_2\text{PO}_2)_3$  is also reported. Its magnetic susceptibility fits a model for a 1D-antiferromagnet with  $2J/k$  of 1.20(1) K and  $g$  of 2.019(2).

---

## Introduction

In developing magnetic materials, chemists have for a number of years been interested in coordination polymers of transition metals.<sup>1,2</sup> Among the criteria for obtaining long-range magnetic ordering, the number of bridging atoms between the moment carriers is an important factor as it defines the strength of the magnetic exchange interaction between the nearest-neighbour moment carriers.<sup>3</sup> The strength decreases with the number of bridging atoms in the connector; for example the critical transition temperature, being dependent of the exchange interaction, is above 800 K for the oxides (one-atom bridge) and decreases to nearly 200 K for the Prussian blue family having two-atom cyanide bridges while for those containing three-atom  $T_C$  are less than 30 K.<sup>4</sup> There is considerable interest by magneto-chemists in using three-atom bridges due to the wider range of chemicals available but only few systems are known where every metal centre is bridged uniformly.<sup>5</sup> Amongst them are those containing azide,<sup>6</sup> imidazole,<sup>7</sup> dicyanamide,<sup>8</sup> carbonate,<sup>9</sup> oxalate<sup>10</sup> and formate<sup>11</sup>. The latter has been of much importance to us in the development of materials exhibiting dual property, such as porosity and magnetism.<sup>11</sup> Following this line of work, we are searching for other ligands to mimic the formate ion and therefore, we have started a study of the structural and magnetic properties of hypophosphite,  $H_2PO_2^-$ .

Hypophosphite salts are known for metals of the alkali,<sup>12</sup> alkaline earth,<sup>13</sup> transition,<sup>14-18</sup> lanthanide,<sup>19</sup> and group 14<sup>20</sup>. Several examples of organic cations are also known to form stable salts. Coordination complexes with a third component, a coordinating organic ligand such as urea, phenanthroline or bipyridine, are known for copper and manganese.<sup>21</sup> Among them, several coordination complexes have been isolated with paramagnetic cations of the first row transition metals. Only few studies of their magnetic properties have been performed and the results show that only two of them exhibit long-range magnetic ordering;  $CoCl(H_2PO_2).H_2O$  is a weak ferromagnet below 8.4 K while  $NiCl(H_2PO_2).H_2O$  is a Curie-Weiss paramagnet above 4.5 K and  $Mn(H_2PO_2)_2.H_2O$  is an antiferromagnet below 6.5 K.<sup>14,16</sup>

Interestingly, the copper(II) complex,  $Cu(H_2PO_2)_2$ , is not very stable and it displays two consecutive phase transitions transforming it between the three ground states.<sup>17</sup> Also of current interest is the variable water content of the cobalt complex,  $Co(H_2PO_2).xH_2O$ ,  $x = 0-0.69$ , which is obtained from cobalt sulfate and it adopts a layered structure where the amount of water residing in the gallery can be altered or replaced by a mixture of pyridine and water (1.86 py and 0.31  $H_2O$ ).<sup>14</sup>

Here, we report the syntheses, single-crystal structure determinations, thermogravimetric analyses, optical spectroscopy and the magnetic properties of an isostructural series,  $[\text{NH}_4][\text{M}^{\text{II}}(\text{H}_2\text{PO}_2)_3(\text{H}_2\text{O})]$ , where  $\text{M} = \text{Mn}, \text{Co}$  and  $\text{Ni}$  as well as the magnetic properties of the structurally characterised  $[\text{Fe}^{\text{III}}(\text{H}_2\text{PO}_2)_3]$ .<sup>18</sup>

## Experimental

### Synthesis

**$[\text{NH}_4][\text{H}_2\text{PO}_2]$** : 158 mL of 50 %  $\text{H}_3\text{PO}_2$  ( $d \sim 1.274 \text{ g/cm}^3$ , 1.58 mol) was mixed slowly with 130 mL of 26 % aqueous ammonia solution ( $d \sim 0.90 \text{ g/cm}^3$ , 1.72 mol) and the mixture was evaporated to yield a white powder. It was dissolved into 150 mL of hot methanol and the solution was cooled before 300 mL of ether was added while stirring. A white crystalline precipitation was obtained after a few hours followed by filtering and washing with ether and finally dried in vacuum. Yield 104.4 g, 82.3 %.

**$[\text{NH}_4][\text{Mn}(\text{H}_2\text{PO}_2)_3(\text{H}_2\text{O})]$**  : A mixture of 2.6 mL of 1.0 M  $[\text{NH}_4][\text{H}_2\text{PO}_2]$  in  $\text{CH}_3\text{OH}$ , 0.3 ml of 1.0 M  $\text{MnCl}_2 \cdot 4\text{H}_2\text{O}$  in  $\text{CH}_3\text{OH}$  and 1.1 ml of water was placed at the bottom of a glass tube. The mixture was then layered with 8 mL of acetone, capped and left to stand. After 1 week pale pink needle crystals of  $[\text{NH}_4][\text{Mn}^{\text{II}}(\text{H}_2\text{PO}_2)_3(\text{H}_2\text{O})]$  and few clear pink blocks of  $[\text{Mn}^{\text{II}}(\text{H}_2\text{PO}_2)_2(\text{H}_2\text{O})]$  were harvested. The crystals were separated manually under an optical microscope for further measurements. Yield 63.7 mg, 74.3 %; Anal. Calcd: H, 4.23; N, 4.90. Found: H, 3.83; N, 4.90 for  $[\text{NH}_4][\text{Mn}(\text{H}_2\text{PO}_2)_3(\text{H}_2\text{O})]$ .

**$[\text{NH}_4][\text{Co}(\text{H}_2\text{PO}_2)_3(\text{H}_2\text{O})]$**  : A mixture of 0.3 mL of 0.4 M  $\text{CoCl}_2 \cdot 6\text{H}_2\text{O}$  in  $\text{CH}_3\text{OH}$ , 2.4 mL of 1.0 M  $[\text{NH}_4][\text{H}_2\text{PO}_2]$  in  $\text{CH}_3\text{OH}$ , 1.2 mL of water was placed in a glass tube and left open to air. After 1 week the mixed solution had concentrated and hexagonal purple-red plate crystals were harvested. Yield 71.0 mg, 61.2 %; Anal. Calcd: H, 4.17; N, 4.83. Found: H, 3.93; N, 4.98.  **$[\text{NH}_4][\text{Ni}(\text{H}_2\text{PO}_2)_3(\text{H}_2\text{O})]$**  : A mixture of 1.0 mL of 1.0 M  $\text{NiCl}_2 \cdot 6\text{H}_2\text{O}$  in  $\text{CH}_3\text{OH}$  and 5.0 mL of 1.0 M  $[\text{NH}_4][\text{H}_2\text{PO}_2]$  in  $\text{CH}_3\text{OH}$  was placed in a glass tube and left open to air. The crystals are formed in two steps; first green blocks are formed which over a period of one week turned into hexagonal yellow-green plate crystals of the desired compound. The crystals were harvested and washed with ethanol and acetone. Yield 227 mg, 78.2 %; Anal. Calcd: H, 4.18; N, 4.84. Found: H, 3.64; N, 4.78.

**$[\text{Fe}(\text{H}_2\text{PO}_2)_3]$**  : 270 mg (4.83 mmol) of Fe powder in a small glass tube ( $\phi$  5 mm, 35 mm height) was placed at the bottom of a large glass tube ( $\phi$  14 mm). 10 mL of 50 %  $\text{H}_3\text{PO}_2$  ( $d \sim 1.274 \text{ g/cm}^3$ , 96.5 mmol) was then added to cover the small tube. After 2 month, colourless

crystals were harvested. The small tube with the remaining Fe powder was taken out and the products in the large glass tube were collected. Yield 1.743 g, 48.1 %

$[\text{Co}(\text{H}_2\text{O})_6](\text{H}_2\text{PO}_2)_2$  : 2 mL of an aqueous solution containing 4.0 M  $[\text{NH}_4][\text{H}_2\text{PO}_2]$  and 1.0 M  $\text{CoCl}_2 \cdot 6\text{H}_2\text{O}$  was placed at the bottom of a glass tube. The solution was layered with 8 mL of acetone and left. After 5 days, the red crystals formed were collected. Yield 0.432 g, 72.5 %. The crystals were distinctly different in shape and colour from those of  $[\text{NH}_4][\text{Co}(\text{H}_2\text{PO}_2)_3(\text{H}_2\text{O})]$ . This phase was checked by determination of the unit cell on single crystal.<sup>14</sup>

### Characterization

Powder X-ray diffraction patterns were recorded using either a Rigaku Rint 2000 system equipped with Cu-K $\alpha$  radiation or a Siemens D500 equipped with Co-K $\alpha$  radiation and employing a scan rate of 4°/min and scan step of 0.02°. The simulated patterns were calculated from single crystal X-ray data using RIETAN-2000 program.<sup>22</sup>

For the single-crystal X-ray structure determinations, diffraction intensity data at 173 K were collected for selected crystals mounted on glass fibers using a Bruker SMART Apex CCD diffractometer equipped with Mo-K $\alpha$ 1 radiation. Absorption corrections were applied using the multiscan program SADABS.<sup>23</sup> The structures were solved by direct methods, and the non-hydrogen atoms were refined anisotropically by the least-squares method on  $F^2$  using the SHELXTL program.<sup>24</sup> The hydrogen atoms were either found by difference Fourier maps or were generated geometrically at theoretical positions using the riding model (C-H, 0.96 Å, N-H, 0.90 Å). Crystal data, as well as details of the data collection and refinement, for the complexes are summarized in Table 1. CCDC- XXX-XXX contain the supplementary crystallographic data for this paper. These data can be obtained free of charge from The Cambridge Crystallographic Data Centre via [www.ccdc.cam.ac.uk/data\\_request/cif](http://www.ccdc.cam.ac.uk/data_request/cif).

Infrared spectra were recorded by transmission through KBr pellets containing ca. 1% of the compounds using a Perkin-Elmer FTIR Spectrum RX1.

UV-Vis absorption spectra were recorded by transmission through glycerol mulls of the grounded crystals held between two microscope slides by use of a UVIKON-XL of BIOTEK Instruments. For the cobalt compound a single crystal transmission spectrum was also measured. The crystal was mounted on cut slots between two aluminium sheets.

Thermogravimetric analyses were performed on approximately 40 mg of each sample using a Perkin-Elmer Pyris 6 TGA operating under dry nitrogen at a heating rate of 5°C per minute.

Magnetic susceptibility measurements were performed in an applied field of 100 Oe on cooling from 300 to 2 K using a Quantum Design MPMS-5S SQUID magnetometer. Isothermal magnetizations at 2 K were measured for each compound from 0 to 50 kOe.

## Results and Discussion

### Synthesis

The syntheses of crystals of  $[\text{NH}_4][\text{M}^{\text{II}}(\text{H}_2\text{O})(\text{H}_2\text{PO}_2)_3]$  for the three metals are quite dependent on the solvents, concentrations and other conditions as presented above. While acetone diffusion works well for manganese, it does not work for cobalt and nickel. Furthermore, the quality of crystals for cobalt is improved by addition of a bit of water while this procedure is not suitable for nickel. A wide range of conditions was tried and the optimised one for each metal is described above. We should note that using ethanol instead of methanol gives no crystals and using diffusion of acetone in pure aqueous solutions of the metal ions and  $[\text{NH}_4][\text{H}_2\text{PO}_2]$  results in powders or crystals of another phase,  $[\text{M}(\text{H}_2\text{O})_6](\text{H}_2\text{PO}_2)_2$ . It appears that different mixtures of methanol-water is required for every metals and the amount of water should be lower for the smaller cations, suggesting a subtle balance between solvation and complexation.

### Structural Characterization

**Table 1.** Crystallographic data for  $[\text{NH}_4][\text{M}^{\text{II}}(\text{H}_2\text{O})(\text{H}_2\text{PO}_2)_3]$ .

Compound	$[\text{NH}_4][\text{Mn}(\text{H}_2\text{O})(\text{H}_2\text{PO}_2)_3]$	$[\text{NH}_4][\text{Co}(\text{H}_2\text{O})(\text{H}_2\text{PO}_2)_3]$	$[\text{NH}_4][\text{Ni}(\text{H}_2\text{O})(\text{H}_2\text{PO}_2)_3]$
formula	H12 Mn N O7 P3	H12 Co N O7 P3	H12 Ni N O7 P3
fw	285.96	289.95	289.73
$T$ , K	173 K	173 K	173 K
Atmosphere	Nitrogen	Nitrogen	Nitrogen
Crystal System	Monoclinic	Monoclinic	Monoclinic
Space Group	$P 2_1/n$	$P 2_1/n$	$P 2_1/n$
$a$ , Å	7.4412(6)	7.3669(15)	7.3202(2)
$b$ , Å	15.1467(12)	14.914(3)	14.7961(4)
$c$ , Å	9.3051(5)	9.2048(18)	9.1762(2)
$\beta$ , deg	108.230(2)	108.38(3)	108.8140(10)
$V$ , Å <sup>3</sup>	996.13(12)	959.7(4)	940.78(4)
$Z$	4	4	4
$D_C$ , g/cm <sup>3</sup>	1.907	2.007	2.046
$\mu$ (Mo K $\alpha$ ), mm <sup>-1</sup>	1.809	2.290	2.574
$T_{\min}$ and $T_{\max}$	0.7137, 0.7137	0.6573, 0.6573	0.7828, 0.6687
$\theta_{\min}$ and $\theta_{\max}$ , deg	3.08, 28.32	3.22, 29.37	2.75, 29.44
no. of total reflections	6149	8020	5878



no. of unique reflections ( $R_{\text{int}}$ )	2414	2646	2750
no. of observed [ $I \geq 2\sigma(I)$ ]	1876	2155	2236
no. of parameters	151	145	145
R1 / wR2 [ $I \geq 2\sigma(I)$ ]	0.0274, 0.0678	0.0267, 0.0705	0.0243, 0.0625
??			
R1 / wR2 (all data)	0.0410, 0.0716	0.0370, 0.0678	0.0356, 0.0651
GOF	1.040	1.102	1.109
$\Delta\rho^h$ , e/Å <sup>3</sup>	-0.369, 0.381	-0.355, 0.668	-0.407, 0.477

The single-crystal structure of  $[\text{Mn}^{\text{II}}(\text{H}_2\text{PO}_2)_2(\text{H}_2\text{O})]$  was also determined and found to correspond to that reported ( $P 2_1/c$ ,  $a = 7.8338(2)$ ,  $b = 7.3864(2)$ ,  $c = 10.7552(2)$  Å,  $\beta = 102.826(1)^\circ$ ,  $Z = 2$ ,  $V = 606.81(3)$  Å<sup>3</sup>).<sup>16</sup>

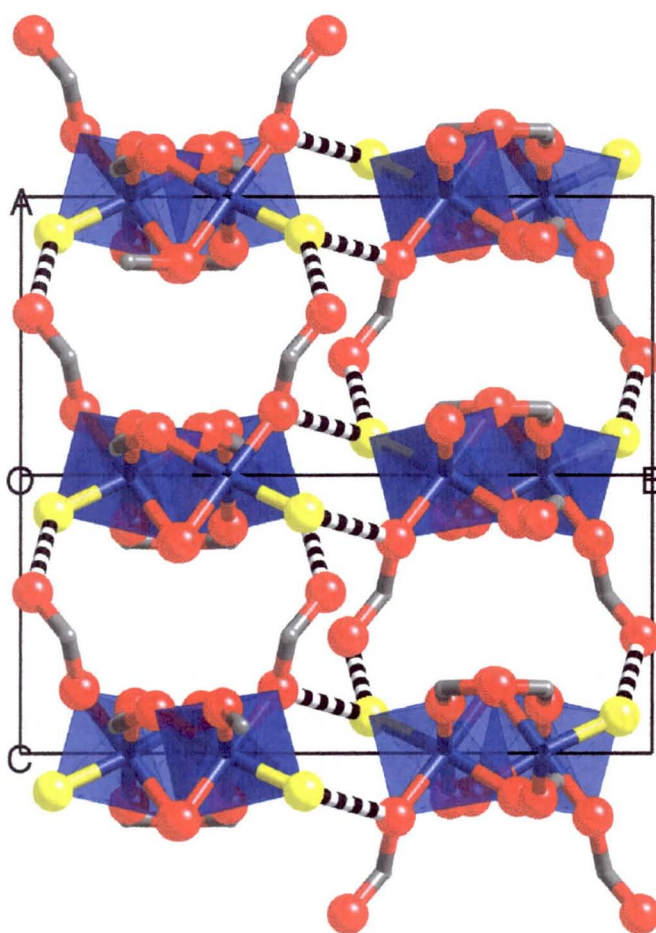


**Figure 1.** Projection of the structure along the 101 direction showing the chains with the terminal O-PH<sub>2</sub>-O pointing in opposite directions, and the hydrogen-bonds (black-white stripped) between the water (yellow) and the oxygen atoms of the terminal O-PH<sub>2</sub>-O.

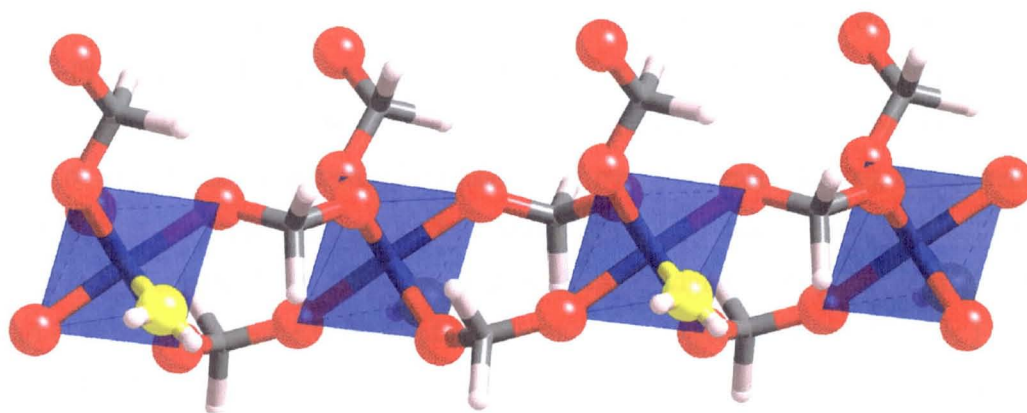


**Figure 2.** Structure of a single chain showing the two bridging O-PH<sub>2</sub>-O, the terminal O-PH<sub>2</sub>-O and the water molecule (yellow).

**Table 2:** Bond lengths (Å) and Angles (°).

Distance		Distance		Distance	
Mn(1)-O(5)	2.134(3)	Co(1)-O(5)	2.0739(16)	Ni(1)-O(5)	2.0527(14)
Mn(1)-O(4)	2.157(2)	Co(1)-O(4)	2.0914(15)	Ni(1)-O(4)	2.0546(13)
Mn(1)-O(3)	2.167(2)	Co(1)-O(3)	2.0929(14)	Ni(1)-O(3)	2.0585(13)
Mn(1)-O(6)	2.185(2)	Co(1)-O(6)	2.1102(15)	Ni(1)-O(6)	2.0738(13)
Mn(1)-O(7)	2.194(2)	Co(1)-O(7)	2.0993(15)	Ni(1)-O(7)	2.0603(13)
Mn(1)-O(1)	2.202(2)	Co(1)-O(1)	2.1244(14)	Ni(1)-O(1)	2.0786(12)
Angle		Angle		Angle	
O(5)-Mn(1)-O(4)	93.08(9)	O(5)-Co(1)-O(4)	92.35(6)	O(5)-Ni(1)-O(4)	92.36(5)
O(5)-Mn(1)-O(3)	176.84(10)	O(5)-Co(1)-O(3)	176.54(6)	O(5)-Ni(1)-O(3)	176.40(6)
O(4)-Mn(1)-O(3)	86.60(8)	O(4)-Co(1)-O(3)	86.48(6)	O(4)-Ni(1)-O(3)	86.54(5)
O(5)-Mn(1)-O(6)	88.17(10)	O(5)-Co(1)-O(6)	87.99(7)	O(5)-Ni(1)-O(6)	87.38(6)
O(4)-Mn(1)-O(6)	93.68(9)	O(4)-Co(1)-O(6)	94.05(6)	O(4)-Ni(1)-O(6)	93.68(5)
O(3)-Mn(1)-O(6)	88.71(8)	O(3)-Co(1)-O(6)	88.84(6)	O(3)-Ni(1)-O(6)	89.27(5)
O(5)-Mn(1)-O(7)	91.69(10)	O(5)-Co(1)-O(7)	91.61(6)	O(5)-Ni(1)-O(7)	91.53(6)
O(4)-Mn(1)-O(7)	173.55(9)	O(4)-Co(1)-O(7)	173.71(6)	O(4)-Ni(1)-O(7)	173.76(6)
O(3)-Mn(1)-O(7)	88.88(9)	O(3)-Co(1)-O(7)	89.83(6)	O(3)-Ni(1)-O(7)	89.87(5)
O(6)-Mn(1)-O(7)	90.81(9)	O(6)-Co(1)-O(7)	90.97(6)	O(6)-Ni(1)-O(7)	91.38(5)
O(5)-Mn(1)-O(1)	95.12(10)	O(5)-Co(1)-O(1)	93.81(7)	O(5)-Ni(1)-O(1)	93.60(6)
O(4)-Mn(1)-O(1)	88.65(9)	O(4)-Co(1)-O(1)	88.56(6)	O(4)-Ni(1)-O(1)	88.93(5)
O(3)-Mn(1)-O(1)	88.02(8)	O(3)-Co(1)-O(1)	89.42(6)	O(3)-Ni(1)-O(1)	89.81(5)
O(7)-Mn(1)-O(1)	86.60(9)	O(7)-Co(1)-O(1)	86.30(6)	O(7)-Ni(1)-O(1)	85.95(5)
O(6)-Mn(1)-O(1)	175.87(9)	O(6)-Co(1)-O(1)	176.77(6)	O(6)-Ni(1)-O(1)	177.18(5)

The crystal structures of the three compounds, as determined from single crystals X-ray diffraction (Table 1), were found to be identical except for the bond distances and angles which vary in relation to the ionic radii of the metal cations (Table 2). The asymmetric unit (Figure S1) contains one transition metal, three pyrophosphite ( $\text{H}_2\text{PO}_2$ ), one water molecule and one ammonium cation. The key feature of the structures is the presence of one-dimensional chains of the transition metals with two bridging O-PH<sub>2</sub>-O and terminal O-PH<sub>2</sub>-O and H<sub>2</sub>O to complete the octahedral coordination of the central metal (Figures 1 and 2). One of the bridging O-PH<sub>2</sub>-O coordinates adopts an anti-anti mode while the other adopts a syn-anti mode and the terminal O-PH<sub>2</sub>-O is in an anti-coordination to the metals. A motif not observed in the chemistry of pyrophosphite coordination. The chains are parallel to one another and point along the 101 direction. Each chain is dipolar with the terminal O-PH<sub>2</sub>-O groups pointing perpendicular to the chain axis and the water molecules point in the opposite direction. However, the chains are related by a 2<sub>1</sub> screw-axis so that neighbouring chains have their dipoles oppositely oriented. The bond distances are all normal with the average M-O increasing in the order Ni < Co < Mn while all the others are similar within experimental errors. The metal centres are only slightly distorted from octahedral geometry and the most noticeable is a 4+2 Jahn-Teller elongation where the longer bonds are to the uncoordinated O-PH<sub>2</sub>-O. Within one chain the Jahn-Teller distortion alternates from site to site by nearly 90°. The bridging and terminal O-PH<sub>2</sub>-O adopt almost identical geometry except for a slightly wider angle O-P-O of 119° for one of the bridging O-PH<sub>2</sub>-O compared to 116° for the other two. Two important hydrogen bonds, involving the water molecule and the terminal O-PH<sub>2</sub>-O, exist to connect the chains into a 3D-network. The first is between O7 (water) and O1 (the coordinated oxygen) and the second is between the O7 and O2 (the non-coordinated oxygen). The ammonium counter-balances the charge and sits in cavity.

### **Powder X-Ray Diffraction**

All the peaks in the powder diffraction patterns of the polycrystalline samples of the compounds (Figure S2) were indexed to those calculated by RIETAN. This suggests there are no other phases present in the bulk samples within the experimental errors of ca. 1%. The diffraction pattern for Fe( $\text{H}_2\text{PO}_2$ )<sub>3</sub> is also consistent with that determined from the single crystal structure (Figures S3 and S4).<sup>18</sup>

## Infrared Spectroscopy

Infrared spectra of the three compounds are shown in figure 3 as well as those of the ammonium salt,  $\text{Fe}^{\text{III}}(\text{H}_2\text{PO}_2)_3$  and  $[\text{Co}(\text{H}_2\text{O})_6](\text{H}_2\text{PO}_2)_2$  for comparison (Table 3). The spectra of the three compounds are almost identical to each other, confirming their isostructural nature. By comparison of the spectra to those of the ammonium salt,  $\text{Fe}^{\text{III}}(\text{H}_2\text{PO}_2)_3$  and  $\text{Co}(\text{H}_2\text{O})_6(\text{H}_2\text{PO}_2)_2$ , the  $\text{NH}_4$ ,  $\text{H}_2\text{O}$  and  $\text{H}_2\text{PO}_2$  group frequencies can be identified.<sup>25</sup> The OH and NH stretching modes are observed above  $3000\text{ cm}^{-1}$  and those of PH are in the range  $2190 - 2400\text{ cm}^{-1}$ . The presence of three such peaks may be due to the three crystallographically independent O-PH<sub>2</sub>-O groups. The bending modes of  $\text{H}_2\text{O}$  and  $\text{NH}_4$  are seen at  $1670$  and  $1400\text{-}1472\text{ cm}^{-1}$ , respectively, while those of PH<sub>2</sub> range between  $1100$  and  $1175\text{ cm}^{-1}$ . The P-O modes are centred at  $1075\text{ cm}^{-1}$ . A medium intensity peak at  $810\text{ cm}^{-1}$  is assigned to the rocking mode of PH<sub>2</sub>. The M-O bond stretch modes are weak and appear below  $500\text{ cm}^{-1}$ .

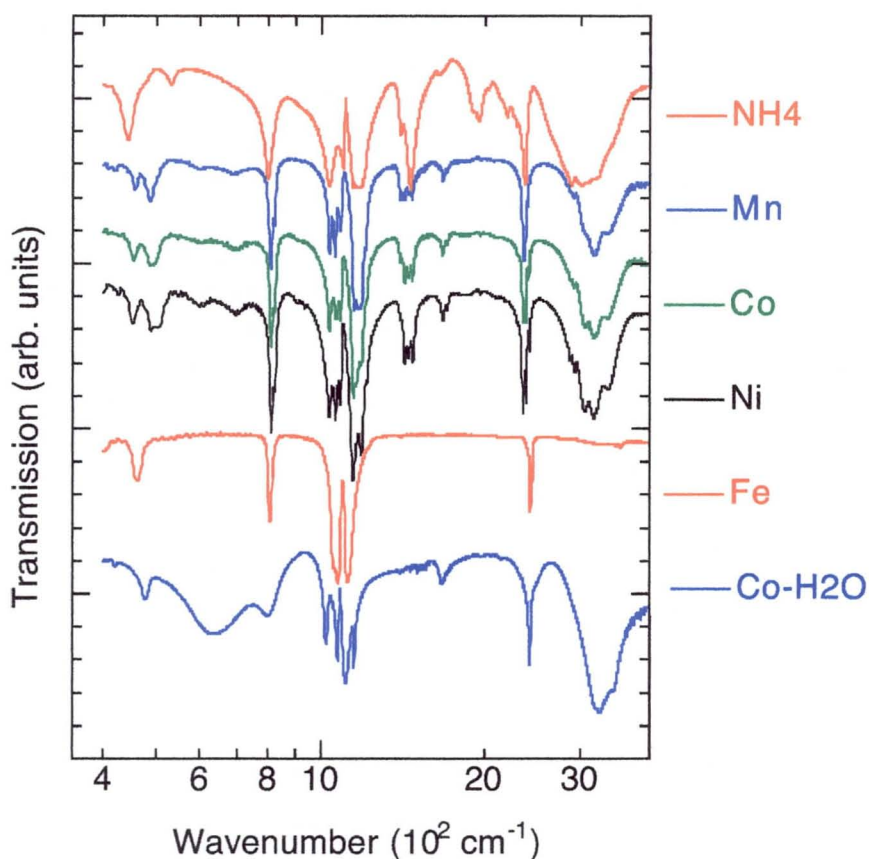


**Figure 3.** Infrared transmission spectra of  $[\text{NH}_4][(\text{H}_2\text{PO}_2)_3]$ ,  $[\text{NH}_4][\text{Mn}(\text{H}_2\text{O})(\text{H}_2\text{PO}_2)_3]$ ,  $[\text{NH}_4][\text{Co}(\text{H}_2\text{O})(\text{H}_2\text{PO}_2)_3]$ ,  $[\text{NH}_4][\text{Ni}(\text{H}_2\text{O})(\text{H}_2\text{PO}_2)_3]$ ,  $\text{Fe}^{\text{III}}(\text{H}_2\text{PO}_2)_3$  and  $\text{Co}(\text{H}_2\text{O})_6(\text{H}_2\text{PO}_2)_2$  (from top to bottom).

**Table 3:** Frequencies and assignments of the bands in the spectra of the complexes.<sup>25</sup>

Mn	Co	Ni	Fe	Co-H <sub>2</sub> O	NH <sub>4</sub>	Assignment
3348 s, br	3350 s, br	3358 s, br		3440 s sh	3494 vw sh	$\nu(\text{N-H})$
3168 s, br	3156 s, br	3156 s, br		3242 vs	3220 s br	$\nu(\text{O-H})$
3052, sh	3048 s, br	3048 s, br		3177 vs	3080 s br	$\nu(\text{O-H})$
2908 vw	2912 vw	2918 vw			3004 s br	
2864 vw	2864 vw	2860 vw			2878 s br	
			2434 s			
			2416 s	2412 s		
2384 w	2398 w	2404 w			2356 s	$\nu(\text{P-H})$
2358 s	2364 s	2368 s			2282 vw	$\nu(\text{P-H})$
2350 s		2350 sh			2250 vw	$\nu(\text{P-H})$
2336 sh	2338 s	2338 s			2192 w	$\nu(\text{P-H})$
					2042 vw	
					1942 m	
					1896 vw	
	1698 vw	1700 vw				
1670 vw	1668 w	1670 w		1670 m	1634 vw	$\delta(\text{H}_2\text{O})$
1472 m	1472 m	1474 m			1462 s	$\delta(\text{NH}_2)$
1450 m	1448 m	1446 m				$\delta(\text{NH}_2)$
1424 m	1426 m	1426 m			1402 w	$\delta(\text{NH}_2)$
1400 m	1402	1402 sh				$\delta(\text{NH}_2)$
1210 sh	1212 sh	1214 vw				
1174 m	1184 m	1184 s			1178 s	$\delta(\text{PH}_2)$
	1160 m			1152 s	1144 vw	$\delta(\text{PH}_2)$
1148 m	1146 s	1144 s	1118 vs	1110 s		$\nu(\text{PH}_2)$
1086 m	1086 m	1086 m				$\nu(\text{PO}_2)$
1076 w	1074 sh	1074 m	1076 vs	1074 s		$\nu(\text{PO}_2)$
1060 m	1064 m	1062 m	1055 s sh			$\nu(\text{PO}_2)$
1036 m	1036 m	1036 m		1023 s	1036 s	$\nu(\text{PO}_2)$
822 w	822 m	822 m				(PH <sub>2</sub> ) rock
810 m	812 m	812 m	807 s	800 s br	800 s	(PH <sub>2</sub> ) rock
				636 s br		
		502 w			530 vw	
486 w	488 w	488 w				
456 w	454 w	452 w	462 m	476 m	442 m	
				420 w		

### UV-Vis Spectroscopy

The UV-vis absorption spectra of the complexes were recorded by transmission through suspensions of finely ground powders in glycerol held between two microscope slides (Figure 4). The spectra therefore suffer from a high diffusion due to scattering which increases with energy. The absorption bands are superposed on this background. These spectra are limited to 350 nm due to absorption of the glycerol and the glass slides. In contrast the transmission spectra recorded through a masked single crystal are free of the high

diffusion and are extended to the highest energy (180 nm). The spectrum for the cobalt complex shows two bands in the visible region; a strong one at 534 nm and a shoulder at 483 nm which are assigned to the  ${}^4T_{1g}(F) \rightarrow {}^4T_{1g}(P)$  and  ${}^4T_{1g}(F) \rightarrow {}^4A_{2g}$  transitions, respectively.<sup>26</sup> The strong bands in the UV region below 200nm are possibly due to the ligands. The spectrum of the nickel complex consists of two weak bands at 767 and 681 nm and a strong one at 417 nm. The former two are assigned to the  ${}^3A_{2g} \rightarrow {}^3T_{1g}(F)$  which is split due to spin-orbit coupling that mixes the  ${}^3T_{1g}$  and  ${}^1E_g$  states. The band at 400 nm is the  ${}^3A_{2g} \rightarrow {}^3T_{1g}(P)$  transition. For the manganese complex, no band is observed in the visible. The observed spectra are characteristics of those of the corresponding divalent metals in an octahedral coordination of six oxygen atoms.<sup>26</sup>

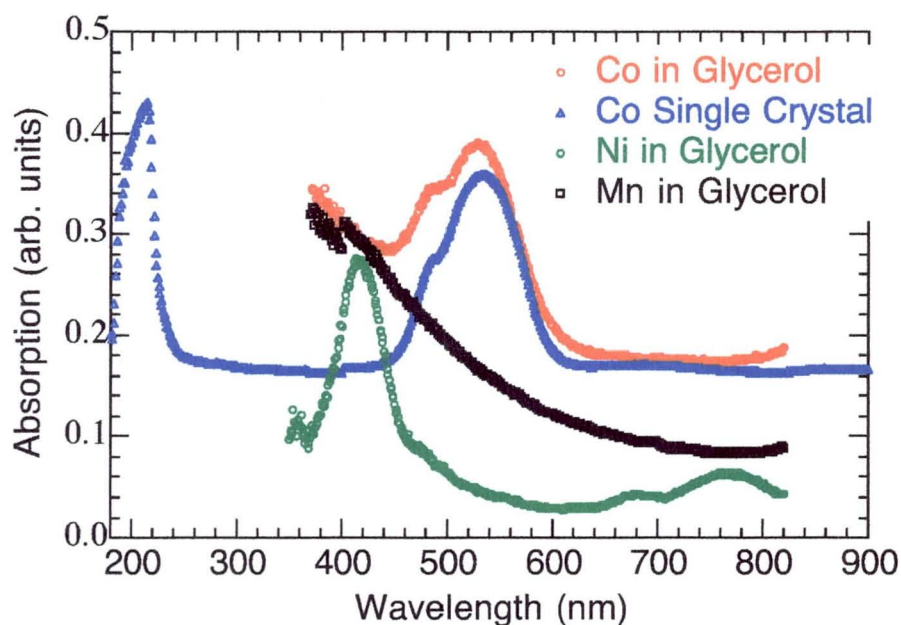


**Figure 4.** Transmission uv-visible spectra of  $[NH_4][Mn(H_2O)(H_2PO_2)_3]$ ,  $[NH_4][Co(H_2O)(H_2PO_2)_3]$  and  $[NH_4][Ni(H_2O)(H_2PO_2)_3]$ .

### Thermogravimetric Analyses

The results of the thermogravimetric analyses indicate that the three compounds behave slightly different (Figure 5). They are stable up to 150°C and the first weight loss corresponds to the departure of the coordinated water and it appears to be harder to remove for the nickel compound compared to those of cobalt and manganese. The second weight loss is the departure of  $NH_3$ . The remaining metal-phosphite has different stability for the three metals. Its stability increases from Mn to Ni and to Co. The products may be the results of

different progression of condensation of  $\text{H}_2\text{PO}_2$  to  $\text{H}_4\text{P}_2\text{O}_3$ ,  $\text{H}_6\text{P}_3\text{O}_4$  and higher weight oligomers.

The colourless crystals of  $\text{Fe}(\text{H}_2\text{PO}_2)_3$  show stability to  $200^\circ\text{C}$  followed by a weight loss amounting to the departure of two oxygen atoms and resulting in a light orange powder. The powder x-ray diffraction of the latter indicates that it is highly crystalline but TREOR and DICVOL are unable so far to find a unit cell. Two further steps to reach a mass corresponding to  $\text{FeH}_6\text{P}_3\text{O}_4$ .

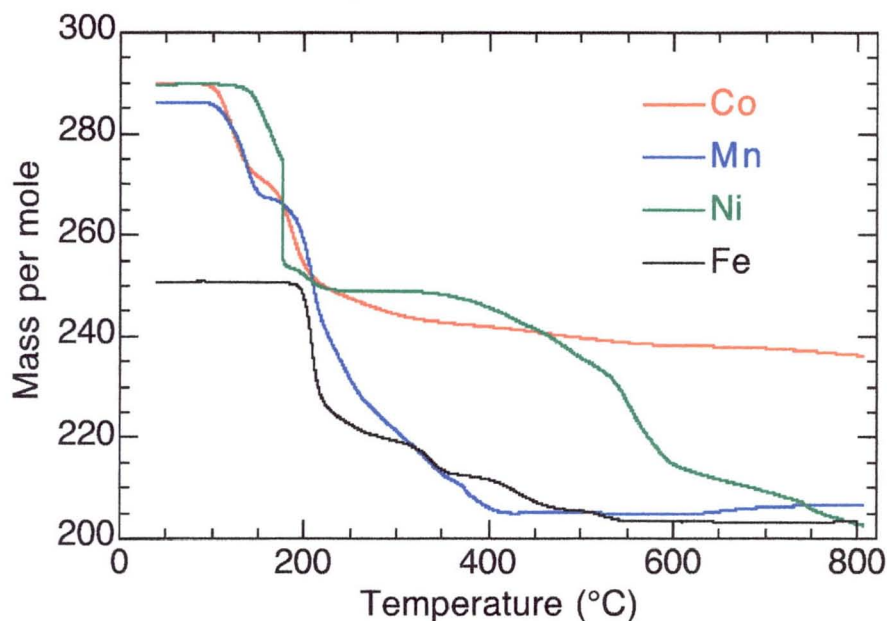


**Figure 5.** Thermogravimetry for  $[\text{NH}_4][\text{Mn}(\text{H}_2\text{O})(\text{H}_2\text{PO}_2)_3]$ ,  $[\text{NH}_4][\text{Co}(\text{H}_2\text{O})(\text{H}_2\text{PO}_2)_3]$ ,  $[\text{NH}_4][\text{Ni}(\text{H}_2\text{O})(\text{H}_2\text{PO}_2)_3]$  and  $\text{Fe}^{\text{III}}(\text{H}_2\text{PO}_2)_3$ .

### Magnetic Measurements

The magnetic susceptibilities and the inverse susceptibilities of the compounds are shown in figure 6. The results of the Curie-Weiss fit of the data and the temperature range are given in table 4. All three compounds exhibit weak antiferromagnetic coupling between nearest neighbours. The Curie constants are all normal for these cations in their divalent oxidation state. However, the Weiss temperatures are quite different due to the presence or absence of local anisotropy. The isothermal magnetizations at 2 K also indicate the presence of AF coupling and therefore deviate from the Brillouin functions for the isolated paramagnets of spin  $5/2$ ,  $3/2$  and 1 (Figure 7).<sup>27</sup>

The susceptibility of  $\text{Fe}(\text{H}_2\text{PO}_2)_3$  is different to those of the divalent metals and it shows a maximum at 5 K (Figure 8). The Curie-Weiss fit of the magnetic susceptibility of  $\text{Fe}(\text{H}_2\text{PO}_2)_3$  for data above 50 K indicates antiferromagnetically coupled nearest neighbour

interaction while a very good fit to a 1D-antiferromagnetic chain, using the equation below, is obtained for the whole temperature range with  $2J/k$  of 1.20(1) K and  $g$  of 2.019(2).<sup>28</sup> The slight deviation below 3 K may be due to the presence of interchain exchange interaction which appears to be also antiferromagnetic. The isothermal magnetization at 2 K also indicate the presence of AF coupling and exhibits a linear dependence on field without reaching saturation at the highest field of our SQUID magnetometer.

$$\chi = \left( \frac{Ng^2\mu_B^2 S(S+1)}{3kT} \right) \left( \frac{1+u}{1-u} \right)$$

$$u = \coth \left( \frac{2JS(S+1)}{kT} \right) - \left( \frac{kT}{2JS(S+1)} \right)$$

**Table 4:** Summary of the magnetic parameters of the complexes.

	Mn	Co	Ni	Fe
Temperature range (K)	2-294	100-294	2-300	50-294
$C / \text{cm}^3 \text{K mol}^{-1}$	4.464(2)	3.49(1)	1.428(2)	4.6(1)
$\theta / \text{K}$	-3.3(1)	-35.0(8)	-3.8(2)	-9.7(4)
1D AF - FIT				$2J/k = 1.20(1) \text{ K}$ $g = 2.019(2)$

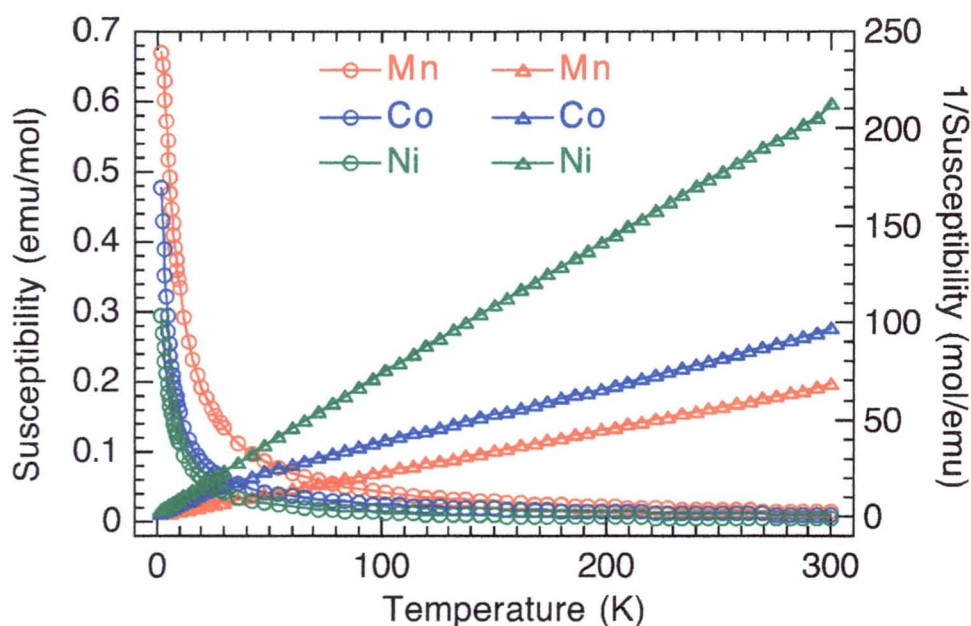


**Figure 6.** Temperature dependence of the magnetic susceptibility (circles) and its inverse (triangles) for  $[\text{NH}_4][\text{Mn}(\text{H}_2\text{O})(\text{H}_2\text{PO}_2)_3]$  (red),  $[\text{NH}_4][\text{Co}(\text{H}_2\text{O})(\text{H}_2\text{PO}_2)_3]$  (blue) and  $[\text{NH}_4][\text{Ni}(\text{H}_2\text{O})(\text{H}_2\text{PO}_2)_3]$  (green).



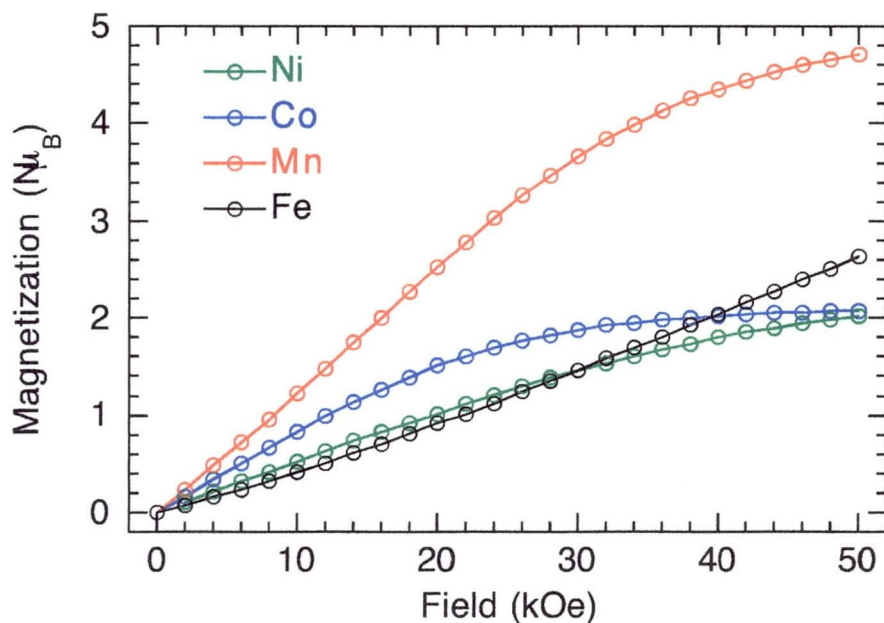


**Figure 7.** Isothermal magnetization for  $[\text{NH}_4][\text{Mn}(\text{H}_2\text{O})(\text{H}_2\text{PO}_2)_3]$  (red),  $[\text{NH}_4][\text{Co}(\text{H}_2\text{O})(\text{H}_2\text{PO}_2)_3]$  (blue),  $[\text{NH}_4][\text{Ni}(\text{H}_2\text{O})(\text{H}_2\text{PO}_2)_3]$  (green) and  $\text{Fe}^{\text{III}}(\text{H}_2\text{PO}_2)_3$  (black).

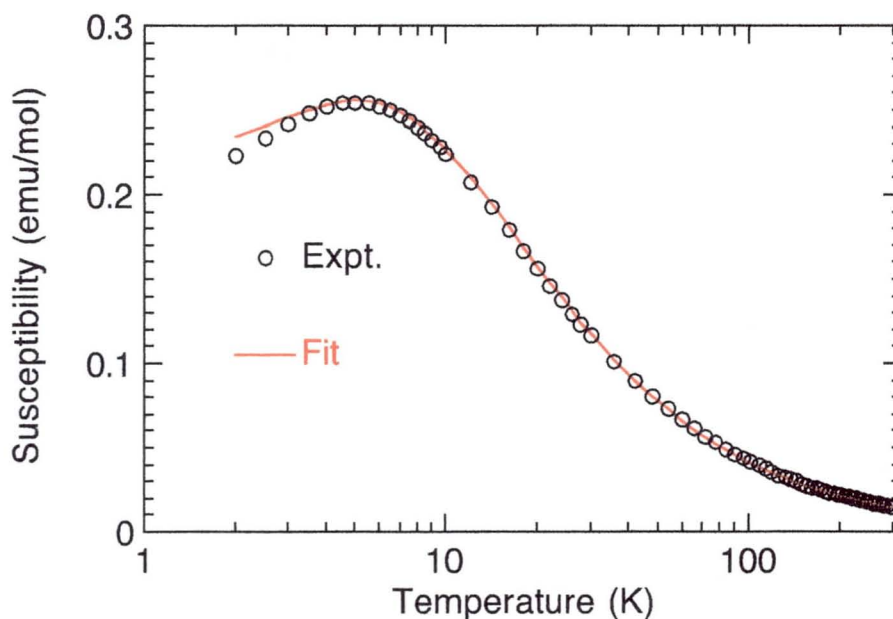


**Figure 8.** Temperature dependence of the magnetic susceptibility of  $\text{Fe}^{\text{III}}(\text{H}_2\text{PO}_2)_3$  (circles) and the fit to a 1D-AF model (solid line).

## Conclusion

In the present work, we have isolated and characterised structurally and magnetically a novel series of transition metal one-dimensional polymers,  $[\text{NH}_4][\text{Mn}(\text{H}_2\text{O})(\text{H}_2\text{PO}_2)_3]$  where

M = Mn, Co or Ni, having two bridging and one terminal O-PH<sub>2</sub>-O groups. They all behave Curie-Weiss paramagnets with weak antiferromagnetic near-neighbour interaction. In contrast, the polymer [Fe(H<sub>2</sub>PO<sub>2</sub>)<sub>3</sub>] with three bridging O-PH<sub>2</sub>-O groups exhibits a one-dimensional antiferromagnetic behaviour.

## Acknowledgements

We thank the CNRS and the University of Hiroshima for funding this work and Université Louis Pasteur for their hospitality to Y.Y. We are also grateful for the partial supports by a Grant-in-Aid for Science Research (A) (No. 18205023) and “Nanotechnology Support Project” of the Ministry of Education, Culture, Sports, Science, and Technology (MEXT), Japan. We thank Dr Serge Vilminot for recording some of the X-ray powder diffraction.

## Supplementary Information.

Numbering scheme adopted in the crystal structure determinations; the cif files for the structures; the calculated and observed powder X-ray diffraction patterns of the complexes; the calculated and observed powder X-ray diffraction patterns of Fe(H<sub>2</sub>PO<sub>2</sub>)<sub>3</sub> and after its decomposition at 220°C. This material is available on the WWW under <http://www.rsc.org> or from the corresponding author.

## References

1. See the (a) ‘Proceedings of the International Conference on Magnetism’, *J. Mag. Mag. Mater.*, **2007**, *310*, Issue 2; (b) ‘Proceedings of the International Symposium on Physics of Magnetic Materials’, *J. Mag. Mag. Mater.*, **2006**, *303*, Issue 2; (c) ‘Proceedings of the International Conference on Molecule-based Magnets (ICMM)’, *Polyhedron*, **2003**, *22*, Issues 14-17; **2005**, *24*, Issues 16-17; **2007**, *26*, Issues 9-11.
2. (a) P. Day and A. E. Underhill, Eds. "*Metal-Organic and Organic Molecular Magnets*". *Philos. Trans. R. Soc. London, Ser. A*, **1999**, *357*, 1-333. (b) O. Kahn, Ed. "*Magnetism: A Supramolecular Function*", *NATO ASI Ser., Ser. C*, **1996**, *484*. (c) K. Itoh and M. Kinoshita, Eds. *Molecular Magnetism, New Magnetic Materials*; Gordon Breach-Kodansha: Tokyo, **2000**. (d) R. L. Carlin, *Magneto-Chemistry*, Springer-Verlag, Berlin, **1986**.
3. P. J. Hay, J. C. Thibeault and R. Hoffmann, *J. Am. Chem. Soc.* **1975**, *97*, 4884-4898.

4. (a) S. J. Blundell, *Magnetism in Condensed Matter*, Oxford University Press, **2001**. (b) M. M. Schieber, *Selected Topics in Solid State Physics, Experimental Magnetochemistry*, vol. VIII, Wohlfarth, E. P. (ed.), North-Holland, Amsterdam, **1967**.
5. X-Y. Wang, Z-M. Wang and S. Gao, *Chem. Commun.*, **2007**, DOI: 10.1039/b708122g.
6. J. Ribas, A. Escuer, M. Monfort, R. Vicente, R. Cortés, L. Lezama and T. Rojo, *Coord. Chem. Rev.*, **1999**, 193-195, 1027-1068.
7. Y-Q. Tian, C.-X. Cai, X.-M. Ren, C.-Y. Duan, Y. Xu, S. Gao and X-Z. You, *Chem. Eur. J.*, **2003**, 9, 5673-5685
8. (a) M. Kurmoo and C. J. Kepert, *New J. Chem.*, **1998**, 1525-1524. (b) S. R. Batten and K. S. Murray, *Coord. Chem. Rev.*, **2003**, 246, 103-130.
9. (a) A. S. Borovik-Romanov, N. M. Kreines, and L. A. Prozorova, *Zh. Éksp. Teor. Fiz.*, **1963**, 45, 64 [*Sov. Phys. JETP*, **1964**, 18, 46]. (b) A. S. Borovik-Romanov, V. G. Zhotikov, and N. M. Kreines, *Zh. Éksp. Teor. Fiz.*, **1978**, 74, 2286 [*Sov. Phys. JETP* **1978**, 47, 1188] (c) T. Lancaster, S. J. Blundell, F. L. Pratt and M. Kurmoo, *Physica*, **2003**, B326, 522-526.
10. (a) M. Ohba and H. Okawa, *Coord. Chem. Rev.*, **2000**, 198, 313-328. (b) C. N. R. Rao, S. Natarajan and R. Vaidhyanathan, *Angew. Chem., Int. Ed.*, **2004**, 43, 1466-1496.
11. (a) Z-M. Wang, B. Zhao, H. Fujiwara, H. Kobayashi and M. Kurmoo, *Chem. Commun.* **2004**, 416. (b) Z-M. Wang, B. Zhang, T. Otsuka, K. Inoue, H. Kobayashi and M. Kurmoo, *Dalton Trans.*, **2004**, 2209-2216. (c) Z-M. Wang, B. Zhang, M. Kurmoo, M. A. Green, H. Fujiwara, T. Otsuka and H. Kobayashi, *Inorg. Chem.*, **2005**, 44, 1230-1237. (d) Z-M. Wang, Y. Zhang, M. Kurmoo, T. Liu, S. Vilminot, B. Zhao and S. Gao, *Aust. J. Chem.*, **2006**, 59, 617-628. (e) Z-M. Wang, B. Zhang, K. Inoue, H. Fujiwara, T. Otsuka, H. Kobayashi and M. Kurmoo, *Inorg. Chem.*, **2007**, 46, 437-445. (f) B. Zhang, Z-M. Wang, M. Kurmoo, S. Gao, K. Inoue and H. Kobayashi, *Adv. Funct. Mater.*, **2007**, 17, 577-584. (g) Z-M. Wang, B. Zhang, Y-J. Zhang, M. Kurmoo, T. Liu, S. Gao and H. Kobayashi, *Polyhedron*. **2007**, 26, 2207-2215. (h) Z-M. Wang, Y. Zhang, T. Liu, M. Kurmoo and S. Gao, *Adv. Funct. Mater.*, **2007**, 17, 1523-1536. (i) Z-M. Wang, X. Zhang, S. R. Batten, M. Kurmoo and S. Gao, *Inorg. Chem.*, **2007**, 46, 8439-8441.
12. (a) M. I. Naumova, N. V. Kuratieva, D. Y. Naumov and N. V. Podberezskaya, *J. Struct. Chem.*, **2004**, 45(3), 465-470. (b) K. J. Gaskell and P. M. A. Sherwood, *Surface Science Spectra*, **2004**, 9, 67-74.
13. (a) M. I. Naumova, N. V. Kuratieva, D. Y. Naumov and N. V. Podberezskaya, *Acta Crystallogr.*, **2005**, C61(2), i14-i16. (b) C. Sugiura, A. Kamata, T. Kashiwakura, H.

- Tezuka, K. Suzuki and S.-I. Nakai, *J. Phys. Soc. Jpn.*, **1997**, *66(1)*, 274-275. (c) N. V. Kuratieva, M. I. Naumova, D. Y. Naumov and N. V. Podberezskaya, *J. Struct. Chem.*, **2004**, *45(2)*, 281-286.
14. (a) M. D. Marcos, P. Amoros, D. Beltran and A. Beltran, *Powder Diffraction* **1994**, *9(1)*, 15-20. (b) A. Le Bail, M. D. Marcos and P. Amoros, *Inorg. Chem.*, **1994**, *33(12)*, 2607-2613. (c) M. D. Marcos, P. Amoros, D. Beltran and A. Beltran, *Inorg. Chem.*, **1994**, *33(6)*, 1220-1226. (d) M. D. Marcos, R. Ibanez, P. Amoros and A. Le Bail, *Acta Crystallogr.*, **1991**, *C47(6)*, 1152-1155. (e) F. Sapina, P. Gomez-Romero, M. D. Marcos, P. Amoros, R. Ibanez, D. Beltran, R. Navarro, C. Rillo and F. Lera, *Eur. J. Solid State and Inorg. Chem.*, **1989**, *26(6)*, 603-617.
15. (a) M. D. Marcos, P. Amoros, F. Sapina, A. Beltran-Porter, R. Martinez-Manez and J. P. Attfield, *Inorg. Chem.*, **1993**, *32(23)*, 5044-52. (b) M. D. Marcos, P. Amoros, A. Beltran and D. Beltran, *Solid State Ionics* **1993**, *63-65(1-4)*, 96-109. (c) S. A. Mikhalyuk and N. V. Romanova, *Ukrainskii Khimicheskii Zhurnal (Russian Edition)* **1978**, *44(8)*, 803-806. (d) N. C. Johnson and W. E. Bull, *Inorg. Chim. Acta* **1978**, *27(2)*, 191-195. (e) N. V. Kuratieva, M. I. Naumova, D. Y. Naumov and N. V. Podberezskaya, *Acta Crystallogr.*, **2003**, *C59(1)*, i1-i3. (f) G. Brun and M. Dumail, *Comptes Rendus des Seances de l'Academie des Sciences, Serie C: Sciences Chimiques*, **1971**, *272(23)*, 1866-1869.
16. M. D. Marcos, P. Amoros, F. Sapina, D. J. Beltran, *Alloys and Compounds* **1992**, *188*, 133-137.
17. D. Y. Naumov, M. I. Naumova, N. V. Kuratieva, E. V. Boldyreva and J. A. K. Howard, *Acta Crystallogr.*, **2002**, *C58(5)*, i55-i60.
18. (a) N. V. Kuratieva and D. Y. Naumov, *Acta Crystallogr.*, **2006**, *C62(1)*, i9-i10. (b) F. Mawrow and J. Zonew, *Z. Anorg. Allgem. Chem.* **1915**, *93*, 311-312.
19. (a) J. A. Seddon, A. R. W. Jackson, R. A. Kresinski and A. W. G. Platt, *Polyhedron* **1996**, *15(11)*, 1899-902. (b) P. A. Tanner, S. T. Hung, T. C. W. Mak and R. J. Wang, *Polyhedron* **1992**, *11(7)*, 817-822.
20. (a) D. Y. Naumov, M. I. Naumova, N. V. Podberezskaya and N. V. Kuratieva, *Acta Crystallogr.*, **2004**, *C60(8)*, i73-i75. (b) D. Y. Naumov, M. I. Naumova and N. V. Kuratieva, *Acta Crystallogr.*, **2005**, *E61(11)*, i251-i252.
21. (a) O. J. Parker, R. M. Harvey and G. L. Breneman, *Acta Crystallogr.*, **1996**, *C52(4)*, 871-873. (b) D. Y. Naumov, D. S. Yufit, E. V. Boldyreva and J. A. K. Howard, *Acta Crystallogr.*, **2001**, *C57(7)*, 790-792. (c) G. L. Breneman, M. Fields and O. J. Parker, *Acta Crystallogr.*, **2002**, *E58(6)*, m262-m264. (d) J. Sala-Pala, R. Kergoat and J. E.

- Guerchais, *Comptes Rendus des Seances de l'Academie des Sciences, Serie C: Sciences Chimiques* **1972**, 274(6), 595-597.
22. F. Izumi and T. Ikeda, *Mater. Sci. Forum*, **2000**, 321-324, 198-203.
  23. Sheldrick, G. M. SADABS 2.05; University of Göttingen: Göttingen, Germany.
  24. (a) Sheldrick, G. M., SHELX97 Programs for Crystal Structure Analysis., Tammanstrasse 4, D-3400 Gottingen, Germany, **1998**. (b) SHELXTL 6.10; Bruker Analytical Instrumentation: Madison, WI, **2000**.
  25. (a) R. I. Bickley, H. G. M. Edwards, A. Knowles, J. K. F. Tait, R. E. Gustar, D. Mihara and S. Rose, *J. Spectrochimica Acta, Part A: Molecular and Biomolecular Spectroscopy* **1994**, 50A(7), 1277-85. (b) R. I. Bickley, H. G. M. Edwards, R. E. Gustar and J. K. F. Tait, *J. Mol. Struct.*, **1992**, 273, 61-72. (c) P. Tanner, L. Yu-Long and T. C. W. Mak, *Polyhedron* **1997**, 16(3), 495-505.
  26. Lever, A. B. P. *Inorganic Electronic Spectroscopy*, 2nd ed.; Elsevier: Amsterdam, **1984**.
  27. Herpin, A. *Theorie du Magnétisme*; Presse Universitaire de France: Paris, **1968**
  28. M. E. Fisher, *Am. J. Phys.*, **1974**, 32, 241.

# Syntheses, Structures and Magnetic Properties of One-Dimensional Chains of Transition Metals with O-P-O Bridges

Yusuke Yoshida,<sup>a,b</sup> Katsuya Inoue,<sup>b</sup> Natalie Kyritsakas<sup>a</sup> and Mohamedally Kurmoo\*<sup>a</sup>

<sup>a</sup> Laboratoire de Chimie de Coordination Organique, CNRS-UMR7140, Université Louis Pasteur, Institut Le Bel, 4 rue Blaise Pascal, 67000 Strasbourg Cedex 01, France.

<sup>b</sup> Department of Chemistry and Institute for Advanced Materials Research, Hiroshima University, Kagamiyama, Higashi-Hiroshima, 739-8526, Japan.

## Supplementary Materials

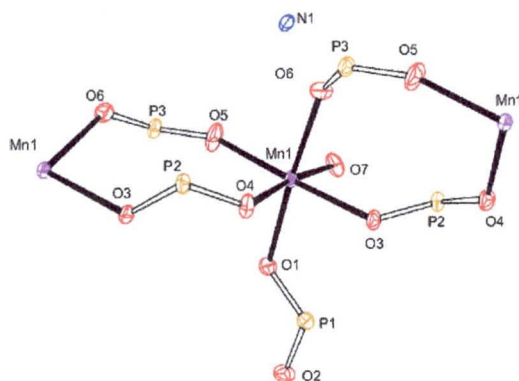


**Figure S1:** Crystal structure and ORTEP drawing for  $[\text{NH}_4][\text{Mn}(\text{H}_2\text{O})(\text{H}_2\text{PO}_2)_3]$ . Co and Ni compounds are isostructural.

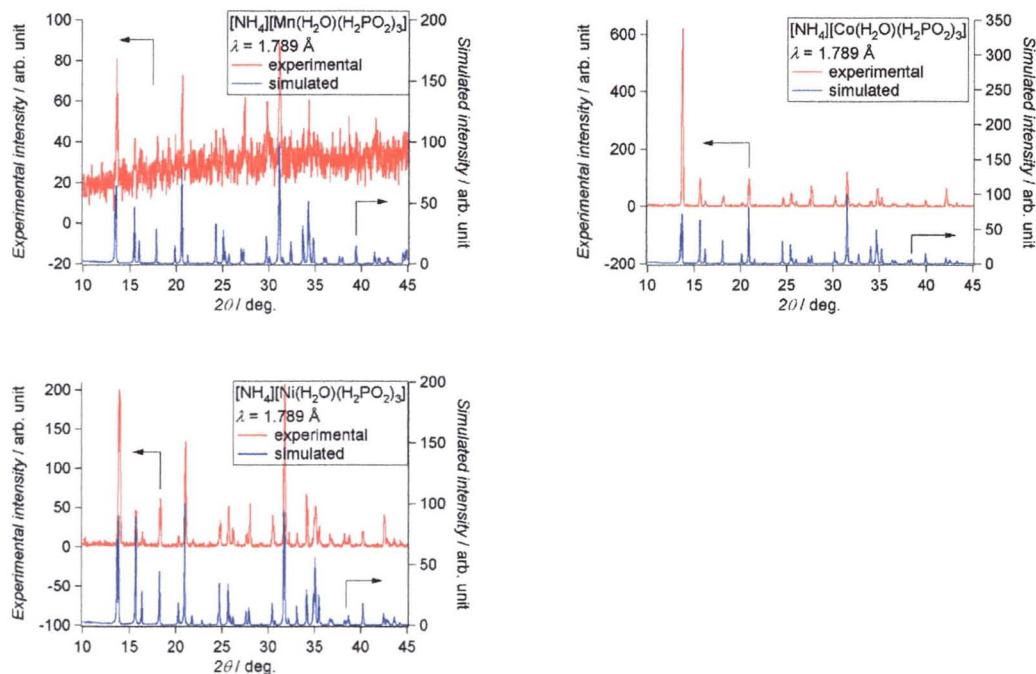


**Figure S2:** Experimental and simulated XRPD patterns ( $\lambda = 1.789 \text{ \AA}$ ).

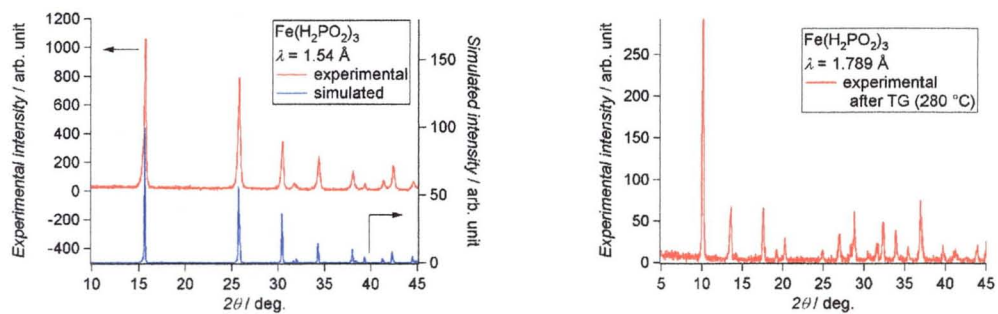


**Figure S3:** Experimental and simulated XRPD patterns for  $\text{Fe}^{\text{III}}(\text{H}_2\text{PO}_2)_3$  ( $\lambda = 1.54 \text{ \AA}$ ; left) and experimental XRPD pattern of its decomposition product at  $220 \text{ }^\circ\text{C}$  ( $\lambda = 1.789 \text{ \AA}$ , right).

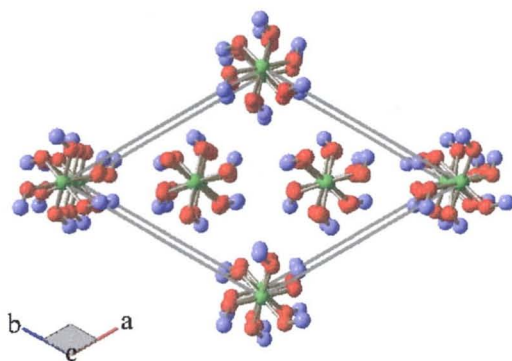


**Figure S4:** View of the crystal structure of  $\text{Fe}(\text{H}_2\text{PO}_2)_3$  showing the arrangement of the one-dimensional chains (reference 18).

## Acknowledgement

I would like to express my deep gratitude to my supervisor, Professor Katsuya Inoue, for guidance of science, experiments. He gave chances to meet many scientists who are from all over the world, and chances to go for abroad with financial support. I would like to thank his great efforts to win the “excellent student scholarship” from Hiroshima university, and for being accepted our 2nd paper for Chemistry Letters.

I am deeply grateful to my supervisor, Dr. Mohamedally Kurmoo, Laboratoire de Chimie de Coordination Organique, Université Louis Pasteur, France. His wide knowledge and his logical thinking way have been great value for me. I have grown up as a scientist through his teaching and discussion. Throughout my thesis-writing period, he provided great teaching on the way how to write the paper from basic step, encouragement, guidance for the important choice in my life. This work would not have been possible without his support and education. I would like to thank his caring during my stay in Europe, too. I enjoyed beautiful buildings and architectures, tasty foods and alcohols, difference of the culture with your great help and support in this period.

I owe my sincere gratitude to Professor Koichi Kikuchi, Tokyo Metropolitan University, who gave me important guidance for finding NEW things, being unique, enjoying the life. First step of the research in Chapter III has started with his pointing.

I wish to thank Prof. Ashot S. Markosian, L. V. Romonosov Moscow State Universtiy, Russia. His passion to the science has inspired me during the collaboration research in Chapter III. His teach on magnet has been great value to me.

I would like to thank Professor Jun-ichiro Kishine, Kyushu Institute of Technology. His explanation on advanced physical part of “chiral magnet” was easy to understand and improved my knowledge.

I warmly thank Professor Shinya Hayami and Dr. Motoko Akita for their constructive



comments, and for their supports throughout this work.

My sincere thanks are due to the official referees, Professor Masahiro Yamashita, Tohoku University, Professor Katsuhiko Miyoshi, and Professor Teruhumi Fujiwara for their review of this thesis.

I warmly thank to Dr. Natalie Kyritsakas, Laboratoire de Chimie de Coordination Organique, Université Louis Pasteur, France, for single crystal X-ray measurement and analysis for the compounds in appendix of this thesis.

I also warmly thanks to the Professor Tsutomu Mizuta for providing machine time of single crystal X-ray machine and Dr. Yukiteru Katsumoto letting me use IR.

I sincerely thank to the staffs those who in Workshop for Advanced Techniques. They gave me many large glass tubes as a gift to make all compounds in title of this thesis. The staffs those who in the Cryogenic Center. They have provided liquid nitrogen and liquid helium for running SQUID machine. The staffs those who in Natural Science Center for Basic Research and Development (N-BARD). They have measured elemental analysis and provided time of single crystal X-ray machine and MCD.

I warmly thank Professor Misako Aida and Mr. Akihiro Yamada for constructive advices for getting Ph. D. degree.

I wish to thank Ms. Kazuyo Nakamura, secretary in our laboratory, for support to make difficult documents for going and staying in France.

During this work I have collaborated with many colleagues for whom I have great regard, and I wish to extend my sincerely thanks to all those who have helped, supported, shared knowledge in Tokyo metropolitan university, Institute for Molecular Science, Hiroshima University, Kyushu Institute of Technology, Kyusyu University, SPring-8, Institut Laue-Langevin, France, and Université Louis Pasteur, France, Universidad de Zaragoza, Spain, and all those who came to our Laboratory.

I am grateful to all my colleagues and friends in Hiroshima University. Dr. Youhei Numata

who stimulated me including unexpected attack in drinking party, Dr. Youhei Yamane who invited me for many experience such as motor-bike trip run through Shimanami-Kaidou, and unique and good shotyu, Dr. Yuki Imamura who brought me to Sanuki area for eating 6 bowls of udon in a day. Mr. Yusuke Kosaka, Aoyama Gakuin University, who made useful programs to run MCD machine and told me many side stories. Mr. Hiroyuki Higashikawa and Mr. Daisuke Urakami who help my experiment. Dr. Koichi Yamada, Mr. Atsushi Turuta, Mr. Koji Nakao and Mr. Hirohumi Honda who have helped the laboratory to run smoothly. Prof. Prasanna S. Ghalsasi, Dr. Hiroyuki Imai, Dr. Kentaro Suzuki, Mr. Kazuki Okuda, Mr. Takaki Morita, Mr. Naoki Wakimoto, Ms. Ai Kusano, Mr. Masaki Atsuchi, Mr. Kenji Nagasawa, Mr. Masato Sonoo, Mr. Yoshihiro Kojima, Mr. Kazuhisa Murata, and Mr. Masahiro Tanigawa who have provided great support, communication, and entertainment.

I am also grateful to all members in Laboratoire de Chimie de Coordination Organique, Université Louis Pasteur, France. My best gratitude is due to Mr. Dmitry Pogozhev for crazy and interesting talk, and for inviting me drinking party and trips to foreign countries. I specially thanks to Dr. Stéphane Baudron, Dr. Domingo Salazar-Mendoza, Mr. Fabrice Eckes, Mr. Claude Wolter, Ms. Marina Kozlova, Ms. Cristina Carpanese, Ms. Elisabeth Kühn Mr. Thomas Lang, Mr. Jérôme Ehrardt, Mr. Pierre Dechambenoit, Mr. Catharine Bronner and Mr. Mei-Jin Lin who have provided emotional support, entertainment, and great conversation.

I cannot end without thanking my family, my parents, Kazuo Yoshida and Ayako Yoshida, my grand parents Kiyoji Yoshida and Sachi Yoshida, and my young sister Taeko Yoshida, on whose constant heartfelt encouragement, support, and understanding, I have concentrated to the study throughout my time at the Academy. It is to them that I dedicate this work.